FURTHER EXPERIMENTAL STUDIES ON GRID-GENERATED TURBULENCE

by
Dana Duong

Thesis submitted to
the University of Ottawa
in partial fulfillment of
the requirements for the degree of

DOCTOR OF PHILOSOPHY

in Mechanical Engineering

Ottawa-Carleton Institute for Mechanical Engineering
University of Ottawa
Ottawa, Canada

Abstract

This thesis describes three experimental investigations of velocity fluctuations and turbulent diffusion and mixing downstream of uniform grids. The first experiment examined the enhancement of turbulent diffusion of a passive scalar with the use of porous obstructions placed downstream of the grid. It was shown that the adopted strategy, which was based on theoretical and empirical arguments, was successful in increasing significantly the spread of a slightly heated plume produced by a line source. The second experiment examined the flow fields behind grids at very small turbulence Reynolds numbers, including values that were lower than any of those in the literature. When Reynolds number was sufficiently large, the grids generated conventional grid turbulence and, when Reynolds number dropped below a certain threshold, which depended on the grid, the flow was essentially steady. For intermediate Reynolds number values, the flow structure depended on the grid geometry and Reynolds number. The Reynolds stress and dissipation anisotropies increased drastically as Reynolds number was decreased within the intermediate range. The Kolmogorov-scaled power spectra differed strongly in this range, but nearly collapsed in their large wavenumber ranges, when normalised by an effective dissipation rate that was fitted to a universal normalised spectrum. The third study examined the effect of mean flow pulsation on grid turbulence and turbulent diffusion. It showed that flow pulsation augmented the turbulent kinetic energy and passive scalar diffusion. The results are discussed in the context of maximising turbulence and turbulent mixing in diverse engineering applications.

Acknowledgements

My sincerest gratitude to my supervisor, Dr. Stavros Tavoularis for his patience and understanding; his guidance has made critical impact on my life, not only for my education and career, but on my day-to-day as well. From the time of my master's degree, you have always been a wonderful supervisor and teacher, full of knowledge and insights that you have tried to bestow upon me. The student-mentor relationship is and has always been of great importance to the scientific endeavor, since the times of our predecessors, exemplified in our long scientific genealogy. I hope in the future that I too can make an impact on a student to the degree that Dr. Tavoularis has made in my life.

I would also like to thank my committee, Dr. Catherine Mavriplis, Dr. Matei Radulescu, Dr. Metin Yaras, and and Dr. Philippe Lavoie for their guidance during the defence process. Their knowledge and intuitions have been invaluable in shaping my research and enhancing my understanding of the field. Each of you brought unique perspectives and constructive feedback that challenged me to think critically and push the boundaries of my work.

Special thanks goes to the mechanical engineering technical staff. I have learned many technical skills from them, and their expertise and aid have helped shape my research significantly.

I am deeply grateful to my parent-in-laws, Octavian and Aurelia Barbu. Both of you have been unwavering in your support, not only to me but also as wonderful grandparents to Luna. Thank you for putting up with my highs and lows throughout this journey and for being by my side during every exam, milestone, and challenge. Your presence and encouragement have meant more to me than words can express, and I could not have done this without you.

Daveyon, while we don't always see eye to eye, we shared a passion for math, and that has always connected us. I wish you luck in your journey ahead. Thank you for being a part of this experience with me.

To my wonderful friends, Omid Beiraghi and Chris Isip. While we are physically far from each other, we will always be close at heart. Thank you for your continued support and wonderful friendship. You guys will always be Luna's uncles, whom she always wants

to see and visit.

I want to thank my friend Ehsan Amjadian for the late-night conversations and for always challenging my thinking. Your support and insights were invaluable throughout this process. I appreciate everything you've done to help me along the way.

To my loving wife Roxana Maria Barbu, I would be nowhere near the person I am today without your continued love and support. From moving for our graduate school programs, to supporting me through long days and nights, and gifting me our Luna, there are no words that can express my eternal gratitude to you.

This thesis is dedicated to my daughter Luna Sofia. I hope that one day your life will lead you to endeavors that keep your life fulfilled, your mind occupied and your heart full of love from family and friends.

Table of Contents

List of Figures

List of Tables

Nomenclature

A	actuator extension
a	pulsation or oscillation amplitude, constant
B	relative extension of linear actuator
b	constant
b_x	bias uncertainty of parameter X
C	concentration, Kolmogorov universal constant
C_ϵ	dissipation parameter
D	diameter of pipe, Taylorian diffusivity
d	grid bar height
E_{11}	streamwise velocity spectra
E_o	output voltage
$E_{c,o}$	corrected output voltage
E_{CW}	cold-wire output voltage
E_{therm}	thermistor output voltage
F	flatness factor
f	pulsation or oscillation frequency
f_{fan}	fan frequency
f_η	Kolmogorov universal function
G	enstrophy
g	gravitational constant
h	height of tunnel or channel
J	rate of molecular diffusivity
K	turbulent kinetic energy
k	turbulent kinetic energy

L	representative length scale
L_1	integral length scale
L_2	transverse length scale
$L_{11,1}$	integral length scale
$L_{22,2}$	transverse length scale
M	grid mesh size
m	fitting coefficient
N	total number of cycles, total number of measurement points
n	fitting coefficient, decay exponent
P	pressure, turbulence production
p	pressure
$\overline{p}$	time-averaged pressure
$\tilde{p}$	oscillating pressure
p_x	precision uncertainty of parameter X
R	autocorrelation coefficient, radius of pipe, sensor resistance
R_w	heated sensor resistance
Re	Reynolds number
Re_d	grid Reynolds number
Re_{ds}	steady grid Reynolds number
Re_{dt}	turbulent grid Reynolds number
Re_G	oscillating grid Reynolds number
Re_I	global Reynolds number
Re_L	local Reynolds number
Re_M	mesh Reynolds number
Re_{Ms}	steady mesh Reynolds number

Re_{Mt}	turbulent mesh Reynolds number
Re_{λ}	turbulence Reynolds number
S	streamwise velocity derivative skewness
S_g	oscillating grid stroke
St	Strouhal number
T	temperature, integral time scale, time
T_1	streamwise integral time scale
T_c	centerline temperature
$T_{c,o}$	reference temperature
T_{cal}	calibration temperature
T_e	eddy turnover time
T_f	instantaneous local flow temperature
T_r	calibration flow temperature
T_w	sensor temperature
$\mathscr{T}$	Lagrangian integral time scale
ΔT	temperature rise
ΔT_{ref}	reference temperature rise
t	time
U	velocity, streamwise velocity
U_1	streamwise velocity
U_2	transverse velocity
U_c	centerline velocity
U_e	external velocity
u	velocity fluctuation
u_1	streamwise velocity fluctuation

u_{1b} streamwise background velocity fluctuation

u_{1bm} streamwise background and noise velocity fluctuation

u_{1m} streamwise measured velocity fluctuation

u_{1n} streamwise velocity noise fluctuation

u_2 transverse velocity fluctuation

u_1' streamwise velocity fluctuation

u_2' transverse velocity fluctuation

u_1^* streamwise turbulence velocity fluctuation

$\tilde{u_1}$ streamwise periodic velocity fluctuation

u_τ friction velocity

X particle displacement, streamwise distance, measured variable

x distance

x_1 streamwise distance

x_2 transverse distance

x_3 spanwise distance

x_{10} effective origin

Greek symbols

α_o	thermal coefficient of resistance
α_p	relative forcing amplitude
γ	molecular diffusivity
δ	boundary layer thickness
δ_X	uncertainty of property X
ϵ	turbulent kinetic energy dissipation rate
η	Kolmogorov microscale
κ_1	streamwise wavenumber
λ	Taylor microscale, non-dimensional amplitude
ν	kinematic viscosity
ν_T	turbulent viscosity
ρ	density
σ	plume half-width
σ_X	standard deviation of property X
τ	time increment
ϕ	divergent or convergent diffuser angle
Ω	non-dimensional frequency, resistance
ω	pulsation or oscillation frequency
ω^+	normalized frequency

Other notations

$\overline{...}$	time average
$\langle ... \rangle$	phase average
$\widetilde{...}$	coherent component

Subscripts

$(...)_i$ $i = 1, 2, 3$, directional index

$(...)_j$ $j = 1, 2, 3$, directional index

Chapter 1

Introduction

1.1 Turbulent flows

Turbulence is a state of fluid motion that, in contrast to laminar motion, has the following characteristics:

- its velocity and vorticity fields, as well as any transported properties, are spatially and temporally random
- it is highly diffusive, causing rapid mixing
- it is rotational and three-dimensional, characterised by high levels of vorticity fluctuations
- it is dissipative, converting kinetic energy of the fluid into heat.

Turbulence is a feature of fluid flow that normally occurs when a dynamic parameter, the Reynolds number, exceeds a certain threshold White *et al.* (2011). The analysis of turbulent flows customarily employs statistical methods. A common approach is Reynolds decomposition (Adrian *et al.*, 2000; White *et al.*, 2011), which decomposes all properties into averages and fluctuations. Turbulent flows are abundant in nature and in technological systems, but these are usually complex and specific to particular geometrical shapes and physical conditions. As such, a universal description of all turbulent flows would be an arduous, if not unachievable, task. However, practical turbulent flows have common features with relatively simple ones, which are usually generated in the laboratory and are referred to as "canonical flows". A documentation and an understanding of canonical turbulence characteristics are essential for our predictive ability of turbulence. Among the common canonical flows that have been studied in laboratories are the following ones:

- grid-generated, nearly isotropic turbulence

- nearly homogeneous, uniformly sheared turbulence
- wakes
- jets
- mixing layers
- thermal plumes
- boundary layers
- pipe and channel flows.

The vast majority of previous studies of canonical turbulence have been performed under stationary conditions, namely, such that the statistical properties of the flow do not change with time. Nevertheless, non-stationary turbulent flows are abundant in the environment and in technological systems. Although time averaging permits a straightforward statistical description of stationary turbulence, non-stationary turbulence characteristics depend statistically on the temporal pattern of each individual flow. The most general non-stationary process is one that has no discernible temporal pattern and so one would not be able to identify trends or recurring events, which can be treated statistically. On the other hand, there are also many non-stationary flows, which may be classified, at least approximately, in one of the following two general categories.

- Flows with a monotonic overall trend, which may be upwards (accelerating flows) or downwards (decelerating flows). Example of such flows are the boundary layers on wings of airplanes during take-off and landing.
- Quasi-periodic flows, in which a distinct overall flow pattern recurs at fixed time intervals. Examples of quasi-periodic flows are the velocity fields in engines of internal combustion. Quasi-periodic flows include oscillatory flows, in which the long-time-averaged velocity vanishes, and pulsatile flows, in which the long-time-averaged velocity is non-zero. An example of the former type is air flow in the human respiratory system, whereas an example of the latter type is blood flow in the large arteries. The statistical description of quasi-periodic flows is usually achieved by phase averaging

of the flow velocity and other random processes, so that fluctuations can be distinguished between coherent ones, which recur periodically, and non-coherent ones, which change from one cycle to the next.

As already mentioned, an important property of turbulence is that it enhances drastically the mixing of transported scalars, which include the concentration of admixtures and heat, thus playing a pivotal role on the rate of chemical reactions and, in some cases, the products of reactions. In many applications, such as in combustion chambers, strong turbulence is introduced deliberately to enhance the mixing of fuel with the oxidant. Passive turbulence generation mechanisms (namely, those that do not require an external power source for their operation) are less complex and generally more robust than active ones. Considerable efforts have been made to design optimal turbulence generators for specific applications, but the general understanding of mixing enhancement mechanisms can benefit from additional investigations of fundamental nature. In particular, studies of combined passive and active turbulence generator designs may reveal advantages that have not been exploited in the past. Grids and other obstructions have been used extensively as turbulence generators and any improvement of their operation by modification of their design or by addition of accessories may find direct application in industrial and transportation systems. It seems intuitive that introduction of pulsatility would, under certain conditions, enhance mixing in grid turbulence, but for this mechanism to be effective, its properties need to be optimised, which requires a detailed documentation of its effects under different conditions. The present work is meant to address such needs.

Grid-generated turbulence has historically been studied at relatively large Reynolds numbers, but there are some applications in which grid Reynolds numbers can be very small, such as flows behind fine meshes used for flow management in wind tunnels. Similar to the laminar-to-turbulent transition of pipe flows (Reynolds, 1883), grid-generated turbulence flows in these small Reynolds number regimes could display unique characteristics that are different from conventional grid-generated turbulence.

1.2 Objectives of the present research

The objective of this research is to investigate experimentally fundamental physical phenomena in grid-generated turbulence. Towards this objective, the following three studies

were performed:

- An examination of the enhancement of passive scalar mixing by porous obstructions in stationary grid turbulence.
- The examination of velocity fields behind uniform grids at very small Reynolds numbers.
- The examination of pulsatile grid turbulence and its comparison to corresponding stationary grid turbulence.

1.3 Plan of the thesis

This thesis is composed of seven chapters. The present first chapter introduces the topic of turbulence as well as laying out the general objectives of the research and a plan for the thesis. The second chapter is a literature survey of the general field of grid turbulence and the three specific topics of investigation. The third chapter describes the experimental facilities and the experimental methods that were used for the present research. The fourth chapter describes the experimental investigation of the enhancement of scalar mixing by porous obstructions in stationary grid turbulence. The fifth chapter discusses the experimental study of very small Reynolds numbers flows behind a grid. The sixth chapter presents the experimental study of pulsatile grid turbulence. The last chapter presents the main conclusions of the thesis and recommendations for future work.

Chapter 2

Literature Survey

2.1 Grid-generated turbulence

Grid-generated turbulence has long served as a popular paradigm of turbulent flows and an essential benchmark for the validation of theories and models. The term "grid" has been used to describe a variety of devices with periodically arranged flow obstructions, including two-dimensional or square arrays of circular or square cylinders, perforated plates and woven screens (Figure 2.1). The main geometrical characteristics of grids are the spacing M between elements, which for square grids is called the mesh size, the wire diameter d, and the solidity σ, which is the ratio of the projected solid area of the grid and the total area (Figure 2.1). When the streamwise mean speed $\overline{U}_1$ is sufficiently large, a grid generates turbulence in the production region, which extends up to a relatively short dimensionless streamwise distance x_1/M from the grid, or, equivalently, a relatively short dimensionless convection time $t\overline{U}_1/M$ ($t = x_1/\overline{U}_1$). In this region, turbulence is produced by the strong shear that is present in the interacting wakes of the solid elements and the jets issuing from the open spaces between elements. The kinetic energy per unit mass k of turbulence reaches a maximum, typically at $x_1/M \approx 4$ (Vassilicos, 2015; Hurst & Vassilicos, 2007; Nedić & Tavoularis, 2016*b*), beyond which it decays monotonically, until it is dissipated entirely to heat.

The decay of grid-generated turbulence is commonly described by an empirically fitted power function of the type

$$k = a\left(\frac{x_1 - x_{10}}{M}\right)^{-n}, \tag{2.1}$$

where a is a constant that depends on the grid geometry, n is the decay exponent and x_{10} is an effective origin. The values of a, n and x_{10} depend on the grid design and are also specific to each of several successive ranges of x_1/M. Several studies (Jayesh & Warhaft, 1992; Hurst & Vassilicos, 2007; Krogstad & Davidson, 2012; Isaza *et al.*, 2014; Nedić & Tavoularis, 2016*b*; Seoud & Vassilicos, 2007; Krogstad & Davidson, 2011; Ertunç *et al.*,

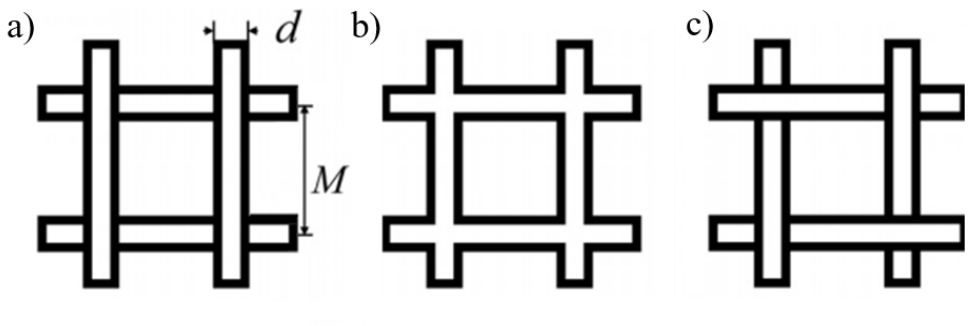

Figure 2.1: Grid types. a) Two-dimensional array. b) Perforated plate. c) Woven screen.

2010; Valente & Vassilicos, 2011, 2014; Zheng *et al.*, 2021) have distinguished the following ranges of decay:

- a "near-field range", typically for $4 \lesssim x_1/M \lesssim 20$, where $1.5 \lesssim n \lesssim 1.8$;
- the "initial period of decay", typically for $20 \lesssim x_1/M \lesssim 150$, where $1.2 \lesssim n \lesssim 1.3$;
- an intermediate range, typically for $150 \lesssim x_1/M \lesssim 500$, where n is somewhat larger than in the previous range;
- and the "final period of decay", for $500 \lesssim x_1/M$, where $n \approx 2.5$.

The strength of the turbulent flow is commonly measured by the value of the turbulence Reynolds number $\mathrm{Re}_\lambda = u_1'\lambda/\nu$, where u_1' is the standard deviation of the streamwise velocity fluctuations, λ is the Taylor microscale and ν is the kinematic viscosity of the fluid. Much interest in the field has focused on studies of grid turbulence having Re_λ values that were as large as possible. Turbulence produced by passive grids has, in most cases, $\mathrm{Re}_\lambda < 100$ (Batchelor, 1953; Comte-Bellot & Corrsin, 1966), whereas active grids have raised the upper limit of this parameter to nearly 1000 (Mydlarski, 2017). It has also been understood that, when Re_λ is smaller than a value of the order of 10, the distinct characteristics that qualify a flow as turbulent tend to become bland and, presumably, for even smaller Re_λ, turbulence would likely become undetectable (Djenidi *et al.*, 2014).

An essential feature of turbulence is the mechanism of energy cascade, which entails an isotropy and universality of the fine structure (first Kolmogorov hypothesis) Kolmogorov

(1941*b*), and that the power spectrum includes an inertial subrange, in which it is proportional to a power of the wavenumber with an exponent $-5/3$ (second Kolmogorov hypothesis) Kolmogorov (1941*c*). The approximate universality of power spectra in the high-wavenumber range (namely, in the inertial and dissipative subranges) has been demonstrated by many authors (Saddoughi & Veeravalli, 1994; Uberoi & Freymuth, 1969; Comte-Bellot & Corrsin, 1971; Kistler & Vrebalovich, 1966; Hearst & Lavoie, 2015; Azzam & Lavoie, 2023; Cekli *et al.*, 2010). This has been evidenced by the approximate collapse of corresponding spectral measurements when normalised by Kolmogorov scales in the form (Pope, 2000)

$$E_{11}(\kappa_1)/(\varepsilon\nu^5)^{1/4} = C(\kappa_1\eta)^{-5/3} f_\eta(\kappa_1\eta)\,, \tag{2.2}$$

where C is a universal constant and $f_\eta(\kappa_1\eta)$ is a universal function. It is common to estimate ε from measurements of λ, under the assumption of isotropy, but Djenidi & Antonia (2012); however, have proposed that the dissipation rate for a given turbulent flow should have a value ε^* that fits, in the large wavenumber range, the universal equation

$$E_{11}(\kappa_1)/(\varepsilon^*\nu^5)^{1/4} = C^*(\kappa_1\eta^*)^{-5/3} f^*_{\eta^*}(\kappa_1\eta^*)\,, \tag{2.3}$$

where $\eta^* = (\nu^3/\varepsilon^*)^{1/4}$ and $C^*, f^*_{\eta^*}(\kappa_1\eta^*)$ were specified empirically.

2.2 Turbulent diffusion

The study of turbulent diffusion is based on Taylor's seminal work, which was formulated for stationary, one-dimensional, isotropic turbulence (Taylor, 1938), and its extension to three-dimensional, homogeneous turbulence (Batchelor, 1949). Analytical and experimental studies of diffusion from a point source and a line source in various turbulent flows include those in channels (Webster *et al.*, 2003; Rahman & Webster, 2005; Lepore & Mydlarski, 2011; Germaine *et al.*, 2014), uniformly sheared flow (Tavoularis & Corrsin, 1981*b*,*a*; Sakai *et al.*, 1986; Karnik & Tavoularis, 1989), and grid-generated turbulence (Taylor, 1938; Warhaft, 1984; Anand & Pope, 1985; Stapountzis *et al.*, 1986). Nedić & Tavoularis (2016*a*) and Tavoularis & Nedić (2017) extended Taylor's diffusion theory to grid turbulence and uniformly sheared flow and confirmed the well known observation that the growth rate of a passive scalar plume is higher in the near-field than in the far-field, where it matches the growth rate of the integral length scale. Several studies Taylor (1938);

Nedić & Tavoularis (2016*b*); Tavoularis & Nedić (2017) have also shown that the mean scalar profile across the plume has an essentially Gaussian shape, which is robust to the flow conditions. Many of these studies also examined properties of the scalar field, such as the mean and fluctuating temperature profiles, and estimates of the Lagrangian velocity autocorrelation function from dispersion measurement (Uberoi & Corrsin, 1952; Nedić & Tavoularis, 2016*b*). Most notably for this study, Tavoularis & Nedić (2017) introduced the term *Taylorian diffusion* to describe passive scalar plume growth in nearly homogeneous turbulence, where the plume width is large compared to the local integral length scale. Additionally, Tavoularis & Nedić (2017) found that, under such conditions, the far-field plume width would be related to the dissipation parameter as

$$\sigma \propto C_\varepsilon^{-1/2} L. \tag{2.4}$$

In grid turbulence (Tavoularis & Nedić, 2017), there is a flow region near the grid, where C_ε grows monotonically and a further downstream region, where $C_\varepsilon \approx$ const. Eq. 2.4 implies that, if the far-field condition ($\sigma \gg L$) is satisfied at the start of the $C_\varepsilon \approx$ const. region, it will continue being satisfied further downstream, so that the plume will grow at the same rate as the turbulence scale does. The analysis also indicates that, if the far-field condition is not satisfied at the start of the $C_\varepsilon \approx$ const. region, it will never be satisfied and the plume will keep growing at a slower rate than L does.

2.3 Low Reynolds number turbulence

The strength of turbulence is commonly quantified by the value of the turbulence Reynolds number $\mathrm{Re}_\lambda = u_1' \lambda / \nu$. The two hypotheses of Kolmogorov, which were mentioned previously, are widely used theoretical postulates, which are meant to apply to flows with sufficiently large Re_λ. The first Kolmogorov hypothesis (Kolmogorov, 1941*b*) postulates that sufficiently strong turbulence has a universal fine structure, which is statistically isotropic (local isotropy), whereas the second Kolmogorov hypothesis (Kolmogorov, 1941*c*) implies that the power spectrum of the turbulence has an inertial subrange, within which it is proportional to the wavenumber raised to a $-5/3$ power. Many studies have examined the universality of the fine structure in different types of flows where the Reynolds number was large, but few investigations scrutinised the validity of this condition as Re_λ diminishes

towards zero. In an early numerical study, Mansour & Wray (1994) examined the power spectrum of nearly isotropic turbulence in the range $15.7 \leq \mathrm{Re}_\lambda \leq 71.4$ and observed that, for $\mathrm{Re}_\lambda \leq 20$, the Kolmorogov-normalised spectrum deviated significantly from those at higher Re_λ. This was further investigated by Djenidi *et al.* (2014), who performed direct numerical simulations (DNS) in low Reynolds number grid turbulence and also found that, as Re_λ dropped below 20, the Kolmogorov-normalised spectra deviated from those at higher Re_λ, but local isotropy was approximately satisfied for Re_λ as low as 3.5. Zheng *et al.* (2021) also observed experimentally that, for their studied range of $5 \leq \mathrm{Re}_\lambda \leq 14$, the Kolmogorov-normalised spectra deviated from the higher Re_λ and that no inertial subrange was present (Figure 2.2).

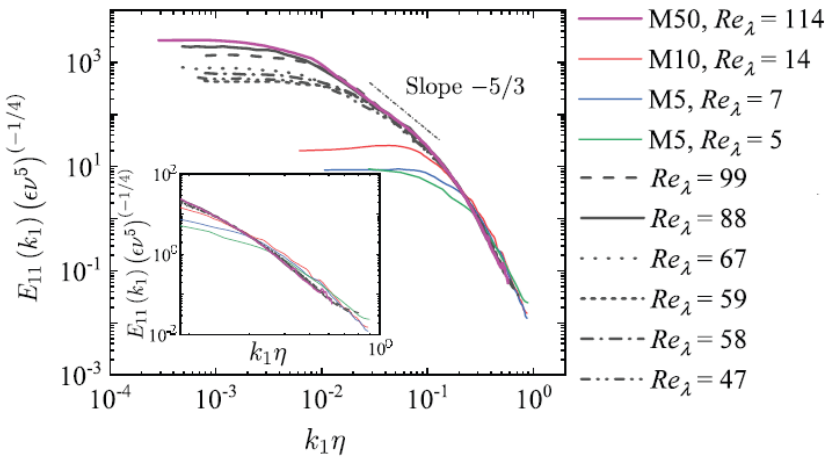

Figure 2.2: Normalized one-dimensional power spectra. Modified from Zheng *et al.* (2021).

A universal characteristic of turbulent flows is the negative value of the skewness S of the streamwise velocity derivative. This parameter is proportional to the average rate of production of enstrophy G (namely, vorticity fluctuations) by turbulent vortex stretching (Taylor, 1938). A non-zero skewness of a random variable is evidence of its non-normality, which, for the case of the streamwise velocity derivative, has been associated with the consistent presence of ramp-like patterns in the velocity signals. The dependence of S on Re_λ has been examined analytically and experimentally in many studies (Van Atta & Antonia, 1980; Kerr, 1985), including specific ones on grid turbulence (Tavoularis *et al.*, 1978; Bennett & Corrsin, 1978; Zheng *et al.*, 2021). Tavoularis *et al.* (1978) showed that

S exhibits a plateau near -0.5 at moderate Re_λ ($\mathrm{Re}_\lambda \gtrsim 10$), but as Re_λ decreases below about 10, S decreases in magnitude towards 0. Similar findings were reported by other authors for a variety of turbulent flows (Bennett & Corrsin, 1978; Kerr, 1985; Van Atta & Antonia, 1980; Antonia & Chambers, 1980). Recent experimental work by Zheng *et al.* (2021) showed agreement with previous observations, with one exception. A review of available literature found no studies of the streamwise velocity derivative in non-stationary flows. The dependence of G upon Re_λ in grid turbulence has been investigated in the range $5 \leq \mathrm{Re}_\lambda \leq 1000$ (Zheng *et al.*, 2021; Lee *et al.*, 2013; Kang *et al.*, 2003; Zhou *et al.*, 2000, 2002; Djenidi & Antonia, 2014; Batchelor & Townsend, 1947; Huang & Leonard, 1994; Larssen & Devenport, 2011). In decaying turbulence that follows a power law, G may be related to S as (George, 1992)

$$\frac{G}{\mathrm{Re}_\lambda} \equiv \frac{15}{7\mathrm{Re}_\lambda}\left(\frac{n-1}{n}\right) + \frac{S}{2}\,. \tag{2.5}$$

This expression shows that, as $\mathrm{Re}_\lambda \to 0$, $(G/\mathrm{Re}_\lambda)/(-S) \to \infty$, which implies that, as turbulent activity weakens, vorticity dissipation tends to dominate its production (Huang & Leonard, 1994; Zhou *et al.*, 2000, 2002; Batchelor & Townsend, 1947; Lee *et al.*, 2013). The same expression implies that, as Re_λ increases, production and dissipation tend to equalise (Zheng *et al.*, 2021; Zhou *et al.*, 2000; Lee *et al.*, 2013).

The flatness factor F of the streamwise velocity derivative is a primary measure of the non-normality of the fine structure of turbulence. It is an indicator of the "spotty" nature of the fine structure, referred to as the internal intermittency of turbulence. This flatness factor was examined by various authors (Zheng *et al.*, 2021; Van Atta & Antonia, 1980; Kerr, 1985; Antonia & Chambers, 1980). For Gaussian random variables, $F = 3$, but, as Re_λ increases, internal intermittency becomes intensified and F increases indefinitely. At low Re_λ, $F \to 3$.

2.4 Statistically periodic turbulent flows

Flows that are pulsatile or oscillatory on the mean are characterised by two main parameters: the amplitude a and the frequency ω or f of the oscillations; one is reminded that $\omega = 2\pi f$, where ω is measured in s^{-1}, whereas f is measured in Hz. Accelerating and decelerating (namely, ramp-like) flows are characterised by the mean acceleration. In all

cases, an important parameter is the instantaneous Reynolds number, which has a main effect on the state of the flow, namely, whether it is laminar, turbulent or transitional. Several different methods to normalise the frequency and/or amplitude of flow oscillations in periodic flows have been proposed in the literature.

In a numerical study of isotropic turbulent flow undergoing periodic forcing, Yang *et al.* (2019) defined the relative forcing amplitude as $\alpha_p = \widetilde{p}/\overline{p}$, where $\widetilde{p}$ is the zero-mean, periodic (dependent on ω) kinetic energy injection rate and $\overline{p}$ is the time-averaged kinetic energy injection rate. These authors also used a normalized frequency, ωT_e, where T_e is the eddy turnover time. Similarly, in an experimental study of active grid turbulence undergoing periodic modulation, Cekli *et al.* (2010) used the normalized frequency fT_e. In oscillatory and pulsating grid turbulence, the stroke S_g of the oscillating grid is an important variable, as a measure of the amplitude of the flow oscillation or pulsation. Although no normalised frequency or stroke parameter is presented in the literature, the main parameter that characterises the flow is the oscillating grid Reynolds number, defined as $\mathrm{Re_G} = MS_g f/\nu$, where M is the grid mesh size (McCorquodale & Munro, 2017).

In the pulsatile pipe flow experiment by Gerrard (1971), two normalized parameters were used. The first one is the non-dimensional frequency $\Omega = R\sqrt{(\omega/\nu)}$, where R is the radius of the pipe and ν is the kinematic viscosity of the fluid; Ω represents the ratio of the tube radius and the distance towards the core at which the vorticity produced at the wall will diffuse during one period. The second one is the non-dimensional amplitude of the oscillations, defined as $\lambda = \omega a/\overline{U}$, where $\overline{U}$ is the cross-sectional and time-averaged velocity. In another pulsatile pipe flow experiment by Mao & Hanratty (1986), the dimensionless frequency ω^+ was defined as $\omega^+ = \omega\nu/\overline{u}_\tau^2$, where $\overline{u}_\tau$ is the friction velocity based on the time-averaged wall shear stress. In a periodic pipe flow experiment, Ramaprian & Tu (1983) used the Strouhal number $\mathrm{St} = \omega D/\overline{u}_\tau$, where D is the diameter of the tube; St is a dimensionless number that is a measure of the ratio of the inertial forces due to the oscillations and the inertial forces due to the convective acceleration. In an experiment in which a turbulent boundary layer was subject to a pulsatile free stream, Cousteix *et al.* (1981) defined a Strouhal number as $\mathrm{St} = \omega X/\overline{U}_e$, where X is the streamwise distance and $\overline{U}_e$ is the time-averaged free stream velocity. In an oscillatory turbulent pipe flow experiment that focused on the boundary layer at the wall, Ronneberger & Ahrens (1977) defined

a Strouhal number as $\mathrm{St} = \omega\nu/\overline{u}_\tau^2$.

2.5 Non-stationary grid-generated turbulence

Previous authors have used different experimental methods to produce non-stationary grid turbulence. Some studies employed the use of active grids with periodically varying solidity; others used oscillated passive grids in a liquid that was initially at rest; and other studies modulated the mean flow upstream of a fixed passive grid. Moreover, there are also computational studies, in which isotropic turbulence was subject to periodic or pulsatile modulation.

Azzam & Lavoie (2019, 2023) used active grids to produce pulsatile flows. Their study focused on documenting the general characteristics of the turbulence, such as the mean and the fluctuation level, as well as documenting the spectra, under varying modes of flow modulation, to apply these unsteady flows to models such as UAVs and wind turbines. In another study, Cekli *et al.* (2010) modulated periodically a turbulent wind tunnel flow using an active grid. They found a resonant enhancement of the turbulent kinetic energy dissipation rate at a modulation frequency equal to the large-eddy turnover rate. Specifically, at $fT_e \approx 1.5$, the dissipation rate was approximately 1.5 times than the dissipation rate at $fT_e = 1$, regardless of the turbulence intensity. The frequency response was found to decrease rapidly as fT_e increased. Furthermore, it was also found that the modulation of the turbulence is affected at low frequencies and large scales, while the small scale structures respond through the turbulent kinetic energy dissipation rate.

Turbulence has been generated by oscillating grids for different purposes. Such studies include the interaction between turbulence and solid impermeable boundaries (McCorquodale & Munro, 2017, 2018*b*), gas-liquid mass transfer at a free surface (Brumley & Jirka, 1987; Chiapponi *et al.*, 2012; Herlina, 2005; Jirka *et al.*, 2010; McKenna & McGillis, 2004; Longo *et al.*, 2013), turbulence in stratified fluids (Thompson & Turner, 1975; Hopfinger & Toly, 1976; Verso *et al.*, 2017; Xuequan & Hopfinger, 1986; Long, 1978; Dickinson & Long, 1978, 1983; Fernando & Long, 1983, 1985; Fernando & De Silva, 1993), and the behaviour of bubbles, aggregates or particulate suspended in a turbulent liquid phase (Morikawa *et al.*, 2008; Nagami & Saito, 2013; Rastello *et al.*, 2020; San *et al.*, 2017; Yao

et al., 2021). Some early works studied the propagation of the turbulent front, separating the turbulent and non-turbulent fluid in an initially homogeneous fluid (Long, 1978; Dickinson & Long, 1978, 1983) and in two fluids (Fernando & Long, 1983, 1985). Later, some studies examined the turbulence structure itself, in various fluid media such as water (Cheng & Law, 2001; McCorquodale & Munro, 2017, 2018*a*), purely elastic fluids (Liberzon *et al.*, 2009; Wang *et al.*, 2015, 2016), and shear-thinning fluids (Lacassagne *et al.*, 2019, 2020). Cheng & Law (2001) examined the turbulence behind an oscillating grid in water. They measured the spatial evolution of the Reynolds stresses and longitudinal and transverse correlations.

Recently, Raushan *et al.* (2019, 2021) used a wave-maker to generate oscillatory surface waves in a water tunnel with an oscillating passive grid. Turbulence parameters such as the phase-averaged velocity, length scales, the turbulence Reynolds number, the dissipation parameter, and the anisotropy factors were documented, but the authors examined them spatially, rather than temporally.

In a recent numerical study by Yang *et al.* (2019), time-periodic forcing was applied to an isotropic turbulent flow in an attempt to examine the effects of modulation on the turbulent kinetic energy and the scalar mixing and verify their previous analytical predictions (Bos & Rubinstein, 2017). Two different forcing schemes were applied, the first was modulation of the turbulent kinetic energy injection rate and the second was modulation of the scalar variance injection rate. It was found that, when the amplitude of the modulation was large and the modulation frequency was small, the transfer rate of the kinetic energy through the energy cascade was improved, while the mixing rate was diminished. In another numerical work, Bos *et al.* (2007) examined the small-scale response to periodically forced isotropic turbulence, with particular interest on the dependence of the turbulent kinetic energy and the dissipation rate upon the Reynolds number, and found that the dissipation at low Reynolds numbers was proportional to ω^{-1}, while, at high and moderate Reynolds numbers, the dissipation was proportional to ω^{-3}. In a theoretical analysis of periodically "kicked", isotropic turbulence, Lohse (2000) found that, for a fixed amplitude, the Reynolds number varied with the frequency at smaller frequencies, but had an initial rise and then approached a saturation value at larger frequencies. Lohse (2000) also documented the saturation values of the Reynolds number for various frequencies and

amplitudes. Lohse (2000) also proposed an experiment to confirm the theoretical results by using two counter-rotating disks; this proposed experiment was later realised by Cadot *et al.* (2003). Several theoretical and numerical studies (von der Heydt *et al.*, 2003*a*,*b*; Kuczaj *et al.*, 2006, 2008) examined isotropic and homogeneous turbulence undergoing modulated energy input. In a theoretical work, von der Heydt *et al.* (2003*a*) proposed that, at higher modulation frequencies, the amplitude of the response of the turbulence decreased proportionally to the inverse of the frequency. It was also proposed that, for smaller modulation frequencies, the response of the turbulence followed the modulation with a nearly constant amplitude. Additionally, it was found that at some frequencies, the amplitude of the response was either significantly diminished or enhanced. Numerical simulations by von der Heydt *et al.* (2003*b*) confirmed that the amplitude of the response of the turbulence at high modulation frequencies decreased proportionally to the inverse of the frequency and that, for smaller frequencies, the response of the turbulence followed the modulation with a nearly constant amplitude. This study was followed up by a direct numerical simulation of the same problem by Kuczaj *et al.* (2006), which arrived at similar conclusions. In another direct numerical simulation, Kuczaj *et al.* (2008) examined the effects of the amplitude and the type of forcing and found that the maximal response was more pronounced for larger amplitudes of forcing. Two types of forcing were examined in this work, the first was the sinusoidal forcing used in previous studies and the second was a square-wave forcing, which is the same as in the periodically "kicked" turbulence by Lohse (2000). It was found that the maximal response of the turbulence occurred at a time of the order of the eddy turnover time. This work was followed up by experimental work by Cekli *et al.* (2010), using an active grid to periodically modulate a turbulent wind tunnel flow; this work was discussed previously in this section. Another recent follow-up study (Fang & Bos, 2023) examined the effects on the dissipation rate from large-scale forcing and from turbulence with reversed initial conditions. Their results showed that the predicted perturbation spectrum showed the $k^{-7/3}$ spectrum, confirming their their previous theoretical predictions and confirming other DNS results (Horiuti & Tamaki, 2013).

2.6 Other non-stationary flows

Pulsating turbulent pipe flows have been studied extensively due to their frequent occurrence in nature and industrial applications. Early experimental studies of such flows used electrolysis (Gerrard, 1971), single-component Laser Doppler Anemometry (Ramaprian & Tu, 1980, 1983; Tu & Ramaprian, 1983), and hot-wire anemometry (Shemer & Kit, 1984; Shemer *et al.*, 1985). Some of the early studies examined the effect of the pulsation frequency ω on the time-averaged flow properties (Gerrard, 1971; Ramaprian & Tu, 1980, 1983; Tu & Ramaprian, 1983). Tu & Ramaprian (1983) and Ramaprian & Tu (1983) found small changes in the time-averaged characteristics, except for the Reynolds stresses, when the oscillation frequency was sufficiently close to the bursting frequency or when the amplitude was sufficiently large. This was further supported by Shemer & Kit (1984), who concluded that, when the frequency of the pulsations was sufficiently large, the turbulence structure responded to the changes in the mean flow and, eventually, the turbulence became independent of the pulsations. Shemer *et al.* (1985) examined the effects of the amplitude of the oscillations on the turbulence and found that they were weaker than the effects of the oscillation frequency. Using the amplitude of the imposed pulsations, Lodahl *et al.* (1998) and Manna *et al.* (2012) distinguished two flow regimes, namely, a current-dominated regime (when $a/\overline{U} < 1$) and a wave-dominated regime (when $a/\overline{U} > 1$). Lodahl *et al.* (1998), found that in some small region of the wave-dominated regime, the phase-averaged wall shear stress was smaller than the quasi-steady values and the current-dominated values and that, in some of these cases, the differences were considerable. These authors attributed this result to the occurrence of a reverse transition, triggered by the suppression of turbulence by the oscillatory mean shear. Large eddy simulation studies by Manna & Vacca (2005); Manna *et al.* (2012) suggest that the averaged wall shear stress was reduced, while the turbulence survived during the entire oscillating cycle.

A first attempt to measure the wall shear stress was made by Mao & Hanratty (1986), who introduced the dimensionless frequency ω^+. An interesting observation in the study is the presence of a relaxation effect, during which the phase angle characterising the temporal change of the wall shear stress undergoes a sharp change over a small range of ω^+. Mao & Hanratty (1992) further reported a decrease in the wall shear stress when the amplitude was large and $\omega^+ = 0.05$.

Earlier works also examined the effect of pulsatility on the critical Reynolds number. Experimentally, it was found that the amplitude and frequency of the pulsations increased the critical Reynolds number, assuming no local flow reversal (Gilbrech & Combs, 1963; Sarpkaya, 1966; Ramaprian & Tu, 1980; Lodahl *et al.*, 1998). Laminar to turbulent transition studies were also carried out by Yellin (1966); Ramaprian & Tu (1980); Shemer & Kit (1984); Shemer *et al.* (1985); Stettler & Hussain (1986). The introduction of the concept of the relaxation time to interpret the effects of a periodic component superimposed onto the mean flow was made by Yellin (1966). It was also found that neither the mean nor the instantaneous Reynolds number provided a sufficient criterion for determining laminar to turbulent transition . Through the relaxation time concept, it was also found that slowly oscillating flows of large amplitude tended to suppress or destroy the turbulence downstream of the disturbance source. Relaminarisation was found to depend on factors such as intermittency of turbulent buffs in the mean quasi-steady flow and the frequency of oscillation (Ramaprian & Tu, 1980). Transition was primarily governed by the instantaneous Reynolds number (Shemer *et al.*, 1985). Transition in pipe flows is mainly associated with plugs of turbulence that can grow or shrink in size (Stettler & Hussain, 1986). The DNS results by Tuzi & Blondeaux (2008) were in qualitative agreement, but differed in value; this difference was attributed to the different levels of flow perturbations present in the experimental apparatus and those introduced in the DNS study.

In accelerating and decelerating pipe flows, previous authors investigated the turbulent production near the wall, the turbulent kinetic energy redistribution among its components and the radial propagation of the turbulence into the core of the flow (Maruyama *et al.*, 1976; Greenblatt & Moss, 1999, 2004; He & Jackson, 2000, 2009; He & Ariyaratne, 2011). Maruyama *et al.* (1976) studied the turbulence response following a step increase or decrease in the flow rate. Following a step increase, generation and propagation of new turbulence occurred, whereas, following a step decrease, there was a decay of the existing turbulence. He & Jackson (2000) measured the phase-averaged velocities, root-mean-square velocity fluctuations and turbulent shear stress in linearly accelerating and decelerating pipe flows. He & Ariyaratne (2011) extended the previous study to include wall shear stress measurements. These authors described that the response of the turbulence underwent a three-stage development, namely a “delay”, during which the turbulence remained largely

unchanged, a rapid change and finally a developed stage. Compared to the quasi-steady flow, the turbulence intensity tended to be smaller in the accelerating flow and larger in the decelerating flow due to the delayed response of the turbulence. For a rapidly accelerating flow, the production of turbulence was proposed by Greenblatt & Moss (2004) to first occur at a location well beyond the buffer layer, and then propagate towards the wall and the core of the flow. This was seen as a consequence of the strongly distorted velocity profile. In an earlier experimental study, (Shuy, 1996) found that the wall shear stress in accelerating flows was smaller than the quasi-steady value and, in decelerating flows, it was greater. Predictions made by Vardy & Brown (2003) using unsteady friction models contradicted the experimental results; the models predicted that the wall shear stress in accelerating flows are initially greater than the corresponding quasi-steady values, then undershoots the quasi-steady values. This is supported by some experimental evidence by He & Ariyaratne (2011). This characteristic was attributed to two mechanisms: the inertia of the flow and the delay in the response of turbulence to changes in the flow.

In a recent experiment, Goltsman *et al.* (2018) examined pulsatile flow in a divergent channel. In a manner that was similar to the approach of Lodahl *et al.* (1998) and Manna *et al.* (2012), Goltsman *et al.* (2018) proposed that the type of pulsating flow regime in plane diverging or converging channels is determined by the value of the parameter fa, compared to $\overline{U}\frac{\delta g\phi}{2\pi h}$, where δ is the boundary layer thickness, ϕ is the opening angle of the converging/diverging channel and h is the height of the channel. These authors classified the effects of the imposed oscillations and the pressure gradient into three regimes:

- when $fa < \overline{U}\frac{\delta g\phi}{2\pi h}$, the pressure gradient played a much larger role than the flow oscillations
- when $fa \approx \overline{U}\frac{\delta g\phi}{2\pi h}$, the effects of pressure gradient and flow oscillations were comparable
- when $fa > \overline{U}\frac{\delta g\phi}{2\pi h}$, the flow oscillations played a larger role than the pressure gradient.

Goltsman *et al.* (2018) found that, for the second and third regimes, there was little effect of the pressure gradient on the ensemble-averaged streamwise velocity and the Reynolds stresses. Some earlier works also examined the turbulence structure and its response in channel flows subject to flow oscillations (Tardu & da Costa, 2005; Tardu *et al.*,

1987). Unlike the response of the turbulence in oscillatory pipe flows, no changes in the time-averaged characteristics, even when the oscillation frequency was sufficiently close to the bursting frequency and when the amplitude was sufficiently large, was observed (Tardu & da Costa, 2005).

In addition to pulsatile and oscillatory pipe flows, the literature also contains a few studies of boundary layers subject to oscillations in the free-stream (Karlsson, 1959; Patel & Young, 1977; Jayaraman *et al.*, 1982; Menendez, 1983; Brereton & Reynolds, 1987; Brereton *et al.*, 1990). These studies concluded that there was no effect of the imposed oscillations on the time-averaged properties. The same conclusion was determined for an accelerating boundary layer due to an external favourable pressure gradient (Finnicum & Hanratty, 1988). Brereton & Reynolds (1987) found that the phase lag of the shear stress increased across the boundary layer with increasing frequency. Brereton *et al.* (1990) extended upon the previous studies by expanding the range of frequencies and found that, even for frequencies for which the instantaneous velocity field differed significantly from the quasi-steady state, the time-averaged quantities remained robust; these authors also showed that no new turbulence was generated by the imposed oscillations. In another study, Menendez (1983) found that the time-averaged wall shear stress decreased slightly with increasing frequency. Recently, Ranade *et al.* (2019) examined a compressible, subsonic (at a Mach number of 0.6) boundary layer, undergoing external periodically forced shearing. The objective of this experiment was to determine whether the external shearing would amplify the turbulence in the boundary layer. The authors found that the turbulence was amplified in a critical layer that was inside the wake region of the boundary layer. This critical layer existed for a range of frequencies and amplitudes.

2.7 Dissipation parameter

A cornerstone assumption in the study of turbulence is that the small-scale motions evolve quickly compared to the timescale of the overall turbulence evolution and are thus in statistical equilibrium (Kolmogorov, 1941*a*). This assumption, together with dimensional analysis, leads to the following relationship between the turbulent kinetic energy dissipation rate ε, the turbulent kinetic energy k and the integral length scale L

$$\varepsilon \propto k^{3/2}/L. \tag{2.6}$$

This is equivalent to the statement that the dissipation parameter

$$C_\varepsilon = \frac{\varepsilon L}{k^{3/2}} \tag{2.7}$$

is constant. The near-constancy of C_ε has been verified by experimental studies in grid-generated turbulence (Batchelor, 1953; Sreenivasan, 1984; Nedić & Tavoularis, 2016*b*), homogeneous shear flow (Sreenivasan *et al.*, 1995; Nedić & Tavoularis, 2016*a*), turbulent boundary layers (Nedić *et al.*, 2017), turbulent wakes (Sreenivasan *et al.*, 1995) and the "French washing-machine" experiment (Cadot *et al.*, 1997) for a wide range of Reynolds numbers. A thorough review of the dissipation parameter was presented by Vassilicos (2015), who examined experimental evidence in grid-decaying turbulence that contradicts the assumption of the constancy of the dissipation parameter. More specifically, it was found that there was a flow region in which

$$C_\varepsilon \propto \frac{\mathrm{Re}_I^m}{\mathrm{Re}_L^n}, \tag{2.8}$$

where Re_I^m is a global Reynolds number, Re_L^n is some local Reynolds number and $m = n \approx 1$. This newly proposed scaling law, coined the "non-equilibrium dissipation law", applies to the region where $C_\varepsilon \neq const.$ and is followed by a region where $C_\varepsilon \approx const.$. In addition to proposing the non-equilibrium dissipation law, Vassilicos (2015) also proposed the following issues that need to be addressed in the study of the dissipation parameter.

1. Does the non-equilibrium dissipation law apply to other turbulent flows? Could similar regions of non-equilibrium dissipation occur in jets, wakes and mixing layers?

2. What causes the transition from a non-constant C_ε region to a constant C_ε region?

3. At which downstream distance does the transition occur and does this distance relate to the geometry of the turbulence generator and the inlet conditions?

4. What is the mechanism that sets the level of dissipation in a turbulent flow?

5. What is the physical significance of Equation 2.8 and what are the properties of the interscale energy transfer and turbulence cascade in regions in which this scaling holds?

Recent studies have begun addressing the first question and to some degree the third question of the previous list. Such studies have been performed in decaying grid turbulence, generated by uniform and fractal grids (Seoud & Vassilicos, 2007; Hurst & Vassilicos, 2007; Mazellier & Vassilicos, 2010; Valente & Vassilicos, 2011, 2012; Nedić & Tavoularis, 2016*b*; Hearst & Lavoie, 2016), uniformly sheared flow (Nedić & Tavoularis, 2016*a*), turbulent boundary layers (Nedić *et al.*, 2017), turbulent wakes (Dairay *et al.*, 2015; Obligado *et al.*, 2016; Nedić *et al.*, 2013), periodic turbulence (Goto & Vassilicos, 2015, 2016), and turbulent planar jets (Cafiero & Vassilicos, 2019; Cafiero *et al.*, 2020). Some studies confirmed that, upstream from the far-field regions, where $C_\varepsilon \approx const.$, there is a region of flow where C_ε may be approximated by Equation 2.8. It has been shown that the non-equilibrium dissipation law can be detected as far downstream as 160 characteristic lengths of the turbulence generator (Cafiero & Vassilicos, 2019). Azzam & Lavoie (2019) studied the dissipation parameter in non-stationary turbulence using an active grid and found that, for high enough frequencies, the dissipation parameter followed Equation 2.8. They also found that C_ε varied throughout the cycle, with the peak values at the point of flow deceleration. The downstream distance at which the transition occurs from non-equilibrium to equilibrium dissipation depends on the inlet conditions, as well as the characteristic length of the turbulence generator. For grid turbulence, the characteristic length is proportional to the mesh size, as it has been shown that an increase in mesh size extends the region of non-equilibrium dissipation (Nedić & Tavoularis, 2016*b*). For turbulent wakes, the characteristic length is proportional to the size of the wake generator and, for turbulent jets, the characteristic length is proportional to the nozzle diameter.

Although several recent studies have examined from different perspectives the dissipation scaling characteristics in different turbulent flows, interscale energy transfer and the turbulence cascade in non-equilibrium dissipation scaling regions require further attention. It has been found that non-equilibrium dissipation scaling is not limited to stationary, spatially developing flows, but also to non-stationary flows (Azzam & Lavoie, 2019, 2023). It seems of interest to investigate the similarities and differences between the energy cascade mechanisms in stationary and non-stationary turbulence.

Chapter 3

Experimental facilities and procedures

3.1 Stationary-flow wind tunnel

The experiments for the study of the enhancement of turbulent mixing by porous obstructions were performed in a stationary-flow wind tunnel. This wind tunnel is an open circuit, moderate speed range, blowing wind tunnel with a 16:1 contraction and a test section with a height of $h = 0.305$ m, a nominal width of $1.5h$ and a working length of approximately $16.6h$ (Figure 3.1).

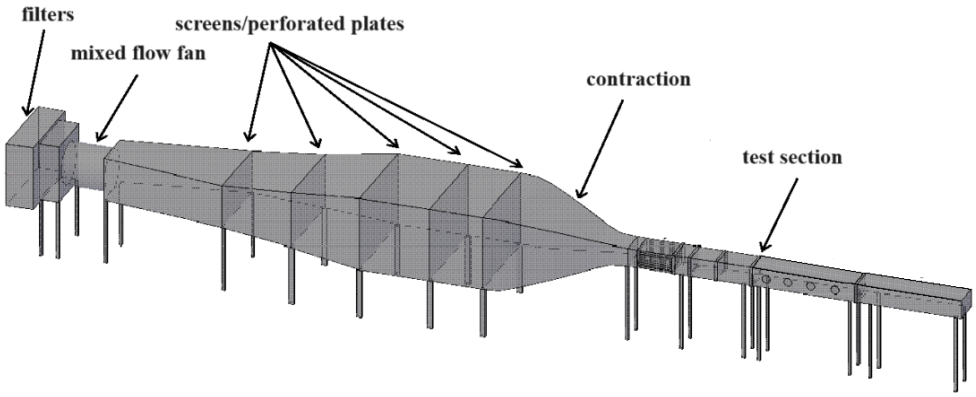

Figure 3.1: Sketch of the stationary-flow wind tunnel.

At the inlet of the fan, air filters were placed to remove 85% of particles with a diameter greater than 1 μm from the air. The air flow was produced by a mixed flow fan (Woods, 63Mx), operated by an electric motor with a variable-frequency-drive (Mitsubishi Electric Inverter, FR-D700). The wind tunnel could achieve a maximum velocity of 30 m/s with a background noise intensity of 0.5%. Downstream of the fan, the flow passes through three diffuser sections, two plenum sections and a contraction, from which it enters the test section. A number of screens are inserted between sections for flow conditioning. The test section (Figure 3.2) is equipped with a three-axis traversing system, allowing probe travel in the streamwise and transverse (vertical) directions and lateral (horizontal) travel

at specific locations. Streamwise traversing has a resolution of approximately 0.5 mm. Transverse and spanwise traversing has a resolution of approximately 0.032 mm. In this study, only the streamwise and transverse traverses were used. The test section is equipped with four ports for the insertion of turbulence generating grids and heat sources. The ports are located at 2.5h, 3.5h, 5h and 7h from the start of the test section. The side walls of the test section between 2.5h and 3.5h have an array of holes for the insertion of cylindrical obstructions. The two side walls of the test section downstream of 2h were diverged linearly to compensate for boundary layer growth. Further details of this wind tunnel have been reported by Karnik & Tavoularis (1987).

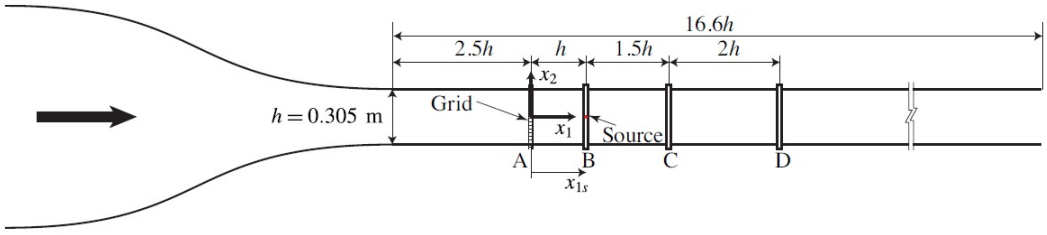

Figure 3.2: Sketch of the test section of the stationary-flow wind tunnel.

3.2 Non-stationary-flow wind tunnel

3.2.1 The wind tunnel

This facility, shown schematically in Figure 3.3, is a substantially modified version of an earlier facility that was designed for the study of non-stationary flows in a rod bundle (Rind & Tavoularis, 2012; Duong, 2017). Extensive literature review provided little guidance for the design of wind tunnels capable of generating non-stationary flows and very low Reynolds number flows. The present facility is uniquely appropriate for such flows and was designed, fabricated and assembled by the author. The main parts of this wind tunnel are described in the following paragraphs.

The centrifugal fan of the rod-bundle facility was replaced with an axial fan (Loren Cook, Model VAB18), which provided a flow with much lower disturbances and noise. The intake contraction to the fan was replaced with a small box, made of plywood and equipped with a fibreglass air filter, which was designed to remove 85% of particles with a diameter greater than 1 μm. Specifications of the axial fan are provided in Appendix A.

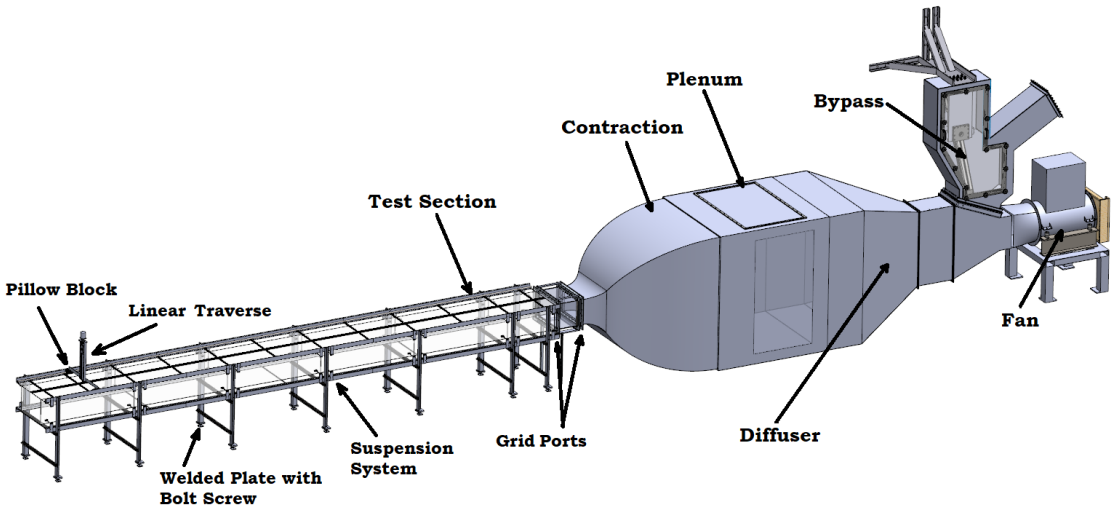

Figure 3.3: CAD model of the non-stationary-flow wind tunnel.

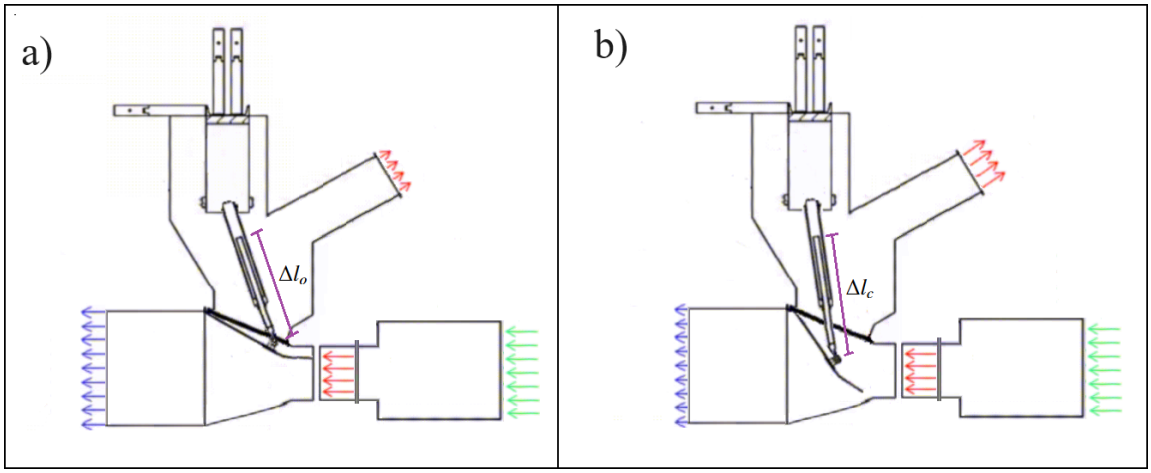

Figure 3.4: Sketches of the bypass section with the actuator extended so that the bypass duct is nearly fully closed (a) and nearly fully open (b).

A new bypass section is connected downstream of the fan. It contains a custom-made, hinged flap, which is operated by a linear actuator (Parker Hannifin Corporation, Model ETH080M32A1XPWDSN600A). The flap has two extreme positions, one which allows almost all of the flow pass through the test section, the other removes almost all of the flow from the test section (Figure 3.4). A transitional channel, connecting the circular outlet of the axial fan to the rectangular inlet of the bypass section was designed, fabricated and installed (see Appendix A).

The diffuser and the plenum of the rod-bundle facility were not modified, but new parts

were added to them. A new rectangular channel with perforated plates was inserted at the inlet of the diffuser to assist in breaking down large-scale air motions generated by the fan and the bypass section. The outlet of the plenum was fit with a new contraction, which led to the new test section. The plenum walls were lined with plywood, which added structural support to the thin plenum walls and helped reduce vibrations of these walls. A new 16:1 ratio contraction, made of aluminium, was also designed and installed between the plenum and the test section. The walls of the contraction were cut with a plasma cutter, rolled to obtain the design curvature and welded together.

A new, modular, rectangular test section was designed and constructed for the needs of this study. This test section has a height of 304.8 mm, an adjustable width with a starting value of 457.2 mm and a length of 6.70 m. It was designed such that its walls can be easily shifted sideways, modified or replaced. The bottom wall is composed of 711.2 mm wide, 10 mm thick, tempered glass panels. The side walls are made of 6.3 mm thick acrylic sheets. The top wall consists of two sets of 6.3 mm thick acrylic panels, separated by a longitudinal, 32 mm wide slot. Double-door weatherstripping (McMaster-Carr, Model 8111A24) was installed in the top wall slot to prevent leakage. The frame holding the test section is made up of steel angle brackets. Each leg of the steel frame rests on a steel plate, welded to a bolt, which allows the adjustment of the height and the levelling of the test section (Figure 3.3). The side walls of the test section were held in place using hinged threaded rods (Figure 3.5), which allow tilting of the walls for boundary layer compensation. The top wall was suspended from T-brackets, welded on beams.

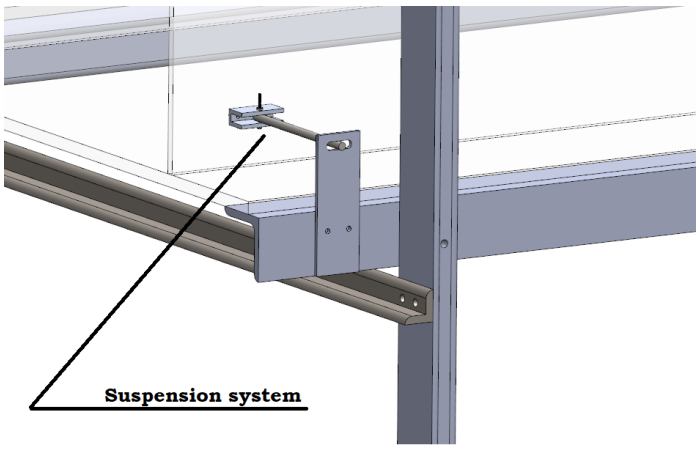

Figure 3.5: CAD model of the side wall suspension and tilting mechanism.

An external traversing system, composed of two hardened steel rails and two super double pillow blocks, was installed, allowing the traversing of probes along the test section. A linear traverse, mounted vertically on the rails, allowed measurements on the vertical centreplane of the test section (Figure 3.3).

3.2.2 Grids and grid insertion ports

A large number of grids, constructed previously for the stationary-flow wind tunnel were available for use in this study. A selection of these, all having square meshes, were actually used. The specifications of these grids are listed in Table 3.2.2. Some grids are made of woven wire, whereas others are perforated plates, machined from a steel sheet with a thickness of 1.6 mm.

Table 3.1: Specifications of various grids that are available for this study.

Name	Type	Mesh Size [mm]	Solidity
M3A	Woven screen	3.2	0.29
M3B	Woven screen	3.2	0.42
M13	Woven screen	12.7	0.29
M19	Perforated plate	19.1	0.25
M51	Perforated plate	50.8	0.25

The test section has two grid insertion ports, one at its inlet and another $1h$ downstream of it. These ports allow the insertion of the same grids as those that were constructed for use in the stationary-flow wind tunnel. A sketch of the test section, with the location of grid insertion ports is shown in Fig. 3.6. The used right-hand Cartesian coordinate system, also shown in this figure, has its origin on the centre of the cross-section at the test section inlet and is oriented such that x_1, x_2, x_3 are, respectively, the streamwise, transverse (namely, vertical) and spanwise axes.

3.2.3 Fan-flap settings calibration map

Flow velocity measurement in the range of present interest using Pitot tubes is not possible, because of the insensitive output of Pitot tubes at velocities lower than about 4 m/s.

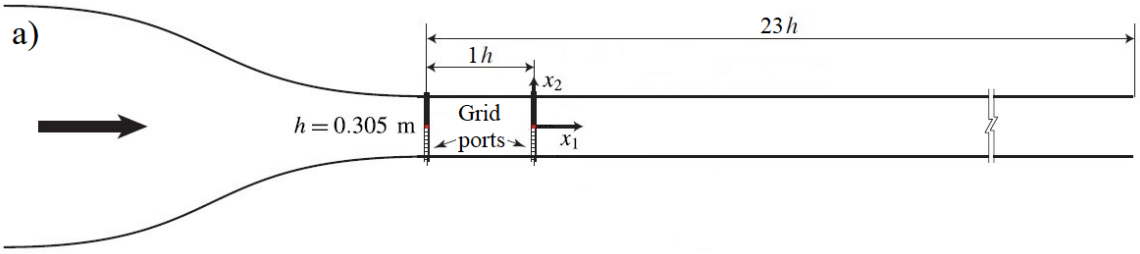

Figure 3.6: Sketch of the non-stationary wind tunnel test section.

Therefore, a different approach was required for the calibration of the hot wires, which are the velocity sensors used in this work. Hot wires can be calibrated at very low air speeds against measurements with a laser Doppler velocimeter (LDV). A two-component LDV system was available for this purpose. Supplied by Dantec Dynamics, consisted of a 5 Watt Argon-ion laser (Model #95L-5, Lexcel Laster, Fremont, USA) split by a transmitter (Fibre Flow, Model #60×41). Flow seeding was provided by droplets of Di-Ethyl-Hexyl-Sebacate (DEHS), generated by a six-jet atomizer (TSI, Model 9306). The LDV measuring volume is positioned on the test section centreline, at a distance of $0.5h$ from the end of the contraction. Preliminary work with the DEHS fluid has shown that the droplets completely evaporate after a period of time and do not affect the flow.

Although, in principle, it was possible to calibrate the hot wires in situ against the LDV measurement, in practice, this would be cumbersome and time consuming, as well as resulting in an excessive release of DEHS fluid in the laboratory. For this reason, hot wires were calibrated against a simpler standard that provided the flow speed in the test section. This speed depended on two settings: the fan rotational frequency f_{fan}, which was set by adjusting the electric motor rotational speed, and the position of the bypass flap, which was set by adjusting the extension of the linear actuator. Denoting the distance between the housing of the linear actuator and the axis of the hinge on which the actuator was pivoting on the flap as Δl, we define the relative extension of the linear actuator as

$$B = \frac{\Delta l_o - \Delta l}{\Delta l_o - \Delta l_c} \ , \tag{3.1}$$

where Δl_c is the actuator extension when the bypass duct is nearly fully open (Figure 3.4b) and Δl_o is the actuator extension when the bypass duct is nearly fully closed (Figure 3.4a).

Figure 3.7a presents a calibration map of the centreline velocity at the inlet of the test section, measured with the LDV system, for different fan frequencies and flap positions.

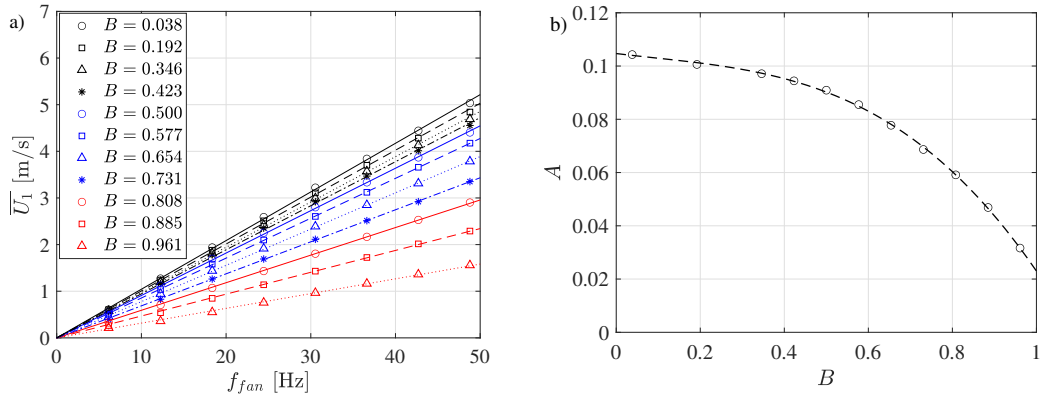

Figure 3.7: a) The fan-flap settings calibration map and b) the dependence of the ratio of the test section speed and the fan speed upon the relative extension of the flap actuator. $x_1/h = 0.5$

It is evident that, for a given flap position the flow velocity was proportional to the fan frequency, namely,

$$\overline{U_1} = A(B) f_{fan} \quad . \tag{3.2}$$

Moreover, the flow velocity in the test section decreased with increasing actuator extension, following the fitted expression (Figure 3.7b)

$$A(B) = -0.0857B^3 + 0.0231B^2 - 0.0191B + 0.105 \quad . \tag{3.3}$$

3.2.4 Quality of flow

The quality of the flow in the test section was determined with the LDV system installed in the flow without any grid.

Mean flow repeatability

LDV measurements to determine the repeatability of the flow velocity at a particular fan speed were taken at different hours of the day on three different days. The fan frequency was set at $f_{fan} = 24.44$ Hz, which provides a flow rate that is approximately 40% of the

fan's maximum capacity, and the linear actuator setting that controls the position of the by-pass flap was set at $B = 0.731$, which diverted most of the air generated by the fan through the by-pass section, thus, away from the test section. It was found that the time-averaged streamwise centreline velocity near the inlet of the test section was $\overline{U_1} = 2.24 \pm 0.2\%$ m/s.

LDV measurements to determine the repeatability of the flow velocity at a particular flap position were taken at different hours of the day during a single day. The linear actuator setting was set at $B = 0.731$ and the fan frequency was set at $f_{fan} = 24.44$ Hz. It was found that the time-averaged streamwise velocity on the test section centreline, at $x_1/h = 1$ was $\overline{U_1} = 2.44 \pm 0.3\%$ m/s.

Background velocity fluctuations

Figure 3.8a shows the standard deviation of the streamwise velocity fluctuations u_1' on the centreline at the inlet of the test section, normalised by the mean velocity $\overline{U_c}$, as measured with the LDV system. This figure shows that the relative background fluctuations $u_1'/\overline{U_c}$ were stronger at very low fan speeds ($f_{fan} < 10$ Hz), but outside this range the wind tunnel background "noise" was quite insensitive to the fan speed. Moreover, this noise, in general, increased significantly as the flap was turned from the nearly-closed-bypass to the nearly-open-bypass position, presumably due to flow separation at the flap tip. Figure 3.8b shows the dependence of the average level of noise (ignoring the very low fan speed measurement at $f_{fan} = 6.13$ Hz) upon the flap setting B. These results indicate that the average background fluctuations are generally within the usual range of academic wind tunnels.

Transverse and spanwise flow uniformity

The mean flow uniformity was assessed by LDV measurements in part of the cross-section at $x_1/h = 0.5$ for a centreline velocity $\bar{U}_c = 2.24$ m/s. As shown in Figure 3.9, in the core of the flow, the mean velocity non-uniformity was lower than 0.8%, whereas boundary layer effects are visible only very close to the walls, particularly in the vicinity of the side-bottom corner.

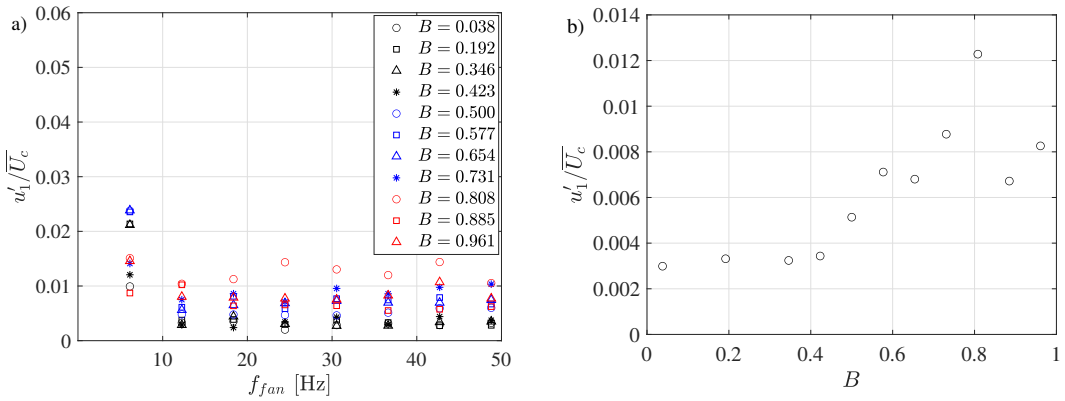

Figure 3.8: a) Normalised streamwise velocity fluctuations at various fan frequencies and actuator positions at the inlet of the test section without any grid inserted; b) the dependence of the average streamwise velocity fluctuations upon the flap setting. $x_1/h = 0.5$

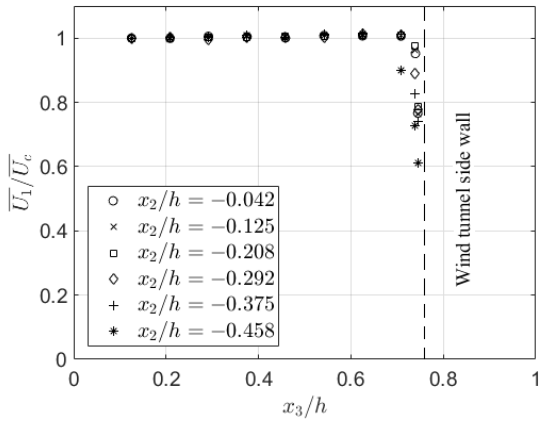

Figure 3.9: Spanwise mean speed profiles at various transverse positions ($x_1/h = 0.5$ and $\bar{U}_c = 2.24$ m/s).

3.3 Velocity measurement

3.3.1 Hot-wire probe

Velocity measurements in this study were conducted with constant temperature hot-wire anemometry (HWA). HWA measures the flow velocity from the convective heat transfer from thin electrically heated sensors, placed in a fluid flow. HWA has excellent frequency response, high spatial resolution and high signal-to-noise ratio, and is ideal for the study of turbulent flows (Bruun, 1995). In the present experiments, two components of the local velocity vector were measured simultaneously with a custom-made cross-wire probe that is shown schematically in Figure 3.10. The sensors are made of platinum-plated tungsten, have a diameter of 2.5 μm and a length of 0.85 mm, and are 0.5 mm apart from each other. The sensors are operated with AALabs1004 Constant Temperature Anemometers.

The frequency response of the anemometers was set by the standard square-wave test. While the anamometer was operating in the flow, a square-wave perturbation was superimposed to the bridge voltage and the bridge damping was adjusted to obtain a slightly under-damped anemometer response. According to Freymuth (1977) the low-pass cut-off frequency f_c of the system is determined as

$$f_c = \frac{1}{1.3\tau_c} , \tag{3.4}$$

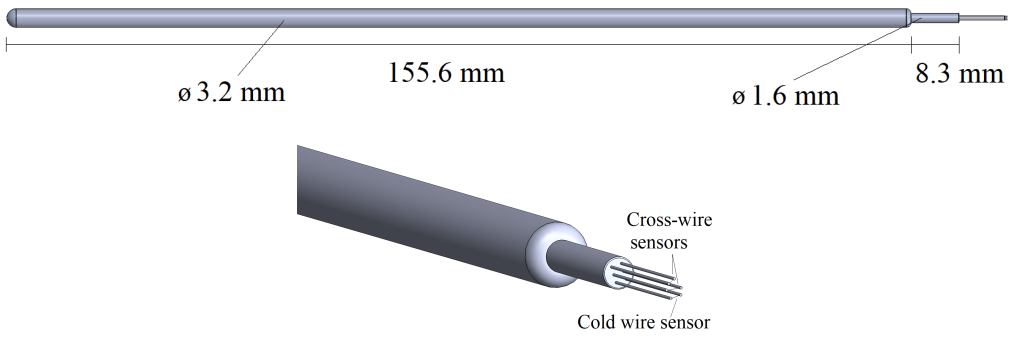

Figure 3.10: Sketches of the hot-wire and cold wire probe (top) and its tip (bottom).

where τ_c is the time between the start of the square-wave input and the time at which the output has decayed to 3% of its maximum value. For the hot-wires used in this study, τ_c = 15 μs, resulting in a cut-off frequency of 51 kHz.

3.3.2 Hot-wire calibration for the stationary-flow wind tunnel study

In the stationary-flow wind tunnel, the hot-wire anemometer was calibrated in situ against a Pitot tube, following standard procedure. In the non-stationary wind tunnel, the hot-wire anemometer was calibrated in the unobstructed inlet to the test section against the flow velocity corresponding to a combination of fan speed and flap setting, which was calibrated previously against LDV measurements. The hot-wire was positioned on the same spot, where the LDV measuring volume was located in previous tests. The wind tunnel was turned on and was allowed to warm up for 30 min before any experiments were performed. The bypass flap setting was set to zero, which corresponded to the mid-position of the flap trailing edge, so that roughly half of the flow bypassed the test section. The hot-wire calibration was performed within a speed range that was wider than the range of speeds in each particular experiment. The upper bound of the calibration range is the highest practical speed of the tunnel, which is about 6 m/s, and the lower bound is about 0.3 m/s, which is well into the mixed convection regime of heat transfer from hot-wires. Both sensors of the cross-wire probe were calibrated simultaneously using a velocity-pitch-map calibration method (Lueptow *et al.*, 1988; Tavoularis & Nedić, 2024). In this method, the probe is calibrated in a steady stream in the wind tunnel without any grid or other obstruction. Calibration is performed for different combinations of the flow velocity magnitude V and

the pitch angle ϕ of the velocity vector with respect to the probe body axis. Thus, V and ϕ are the two input parameters (the yaw angle is set to zero). The two sensor voltages E_1, E_2 are the calibration outputs. Each input is related to the two outputs by a surface polynomial $V(E_1, E_2)$, $\phi(E_1, E_2)$ of third order, as, for example,

$$\begin{aligned} V(E_1, E_2) = \; & b_1 E_1^3 + b_2 E_1^2 + b_3 E_1 + b_4 E_2^3 \\ & + b_5 E_2^2 + b_6 E_2 + b_7 E_1 E_2 \\ & + b_8 E_1^2 E_2 + b_9 E_1 E_2^2 + b_{10} \; . \end{aligned} \tag{3.5}$$

The coefficients $b_1, b_2, \ldots$ are fitted to the calibration data by a two-dimensional curve-fitting algorithm. An example of a calibration is presented in Figure 3.11. In this example, the velocity calibration surface polynomial was $V(E_1, E_2) = -0.172E_1^3 - 0.268E_1^2 - 0.722E_1 + 0.041E_2^3 - 0.067E_2^2 - 0.931E_2 + 0.129E_1E_2 + 0.381E_1^2E_2 - 0.381E_1E_2^2 - 0.665$.

During an experiment, the two sensor voltages are recorded and the polynomials are used to determine the instantaneous values of the corresponding velocity magnitude V and pitch angle ϕ. The corresponding streamwise and transverse velocity components are then determined as $U_1 = V\cos\phi$ and $U_2 = V\sin\phi$.

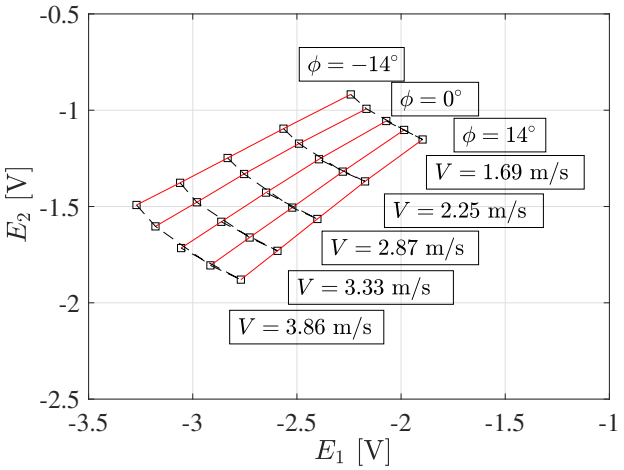

Figure 3.11: Example of cross-wire velocity calibration for the look-up method. □ are the measured voltages, red-solid lines represent constant-angle lines, and black-dashed lines represent constant-velocity lines.

The instantaneous outputs of the hot-wire sensors were corrected for the difference between the calibration temperature T_{cal} and the instantaneous local flow temperature T_f,

which was taken to be equal to the sum of the time-average temperature, measured by the thermistor, and the mean-free temperature fluctuations, measured by the cold wire, both to be discussed in the next section. A correction based on thermistor measurements alone was applied in isothermal flows.

The output voltage from the anemometer was corrected as

$$E_{c,o} = E_o \sqrt{\frac{T_w - T_r}{T_w - T}}, \tag{3.6}$$

where T_r is the flow temperature at which the calibration took place, T is the new flow temperature and T_w is the sensor temperature. $T_w - T$ was calculated as

$$T_w - T = (1/\alpha_o)\,[R_w - R(T)]. \tag{3.7}$$

where α_o is the thermal coefficient of resistance of the sensor material at a reference temperature T_o, R_w is the resistance of the heated sensor (as set at the anemometer) and $R(T)$ is the resistance of the sensor at the flow temperature T.

3.3.3 Hot-wire calibration for the non-stationary wind tunnel studies

For the non-stationary wind tunnel studies, the hot-wire anemometer was calibrated in the unobstructed inlet to the test section against the flow velocity corresponding to a combination of fan speed and flap setting, which was calibrated previously against LDV measurements for a larger speed range (between 0.5 and 3.9 m/s) using the lookup method.

3.3.4 Corrections of the velocity measurement in the non-stationary-flow wind tunnel

Velocity measurements in the non-stationary-flow wind tunnel were corrected for the effects of the wind tunnel background fluctuations and electronic noise. For example, the instantaneous measured streamwise velocity fluctuation downstream of the grid was expressed as

$$u_{1m} = u_1 + u_{1b} + u_{1n}\ , \tag{3.8}$$

where u_1 is the velocity fluctuation generated by the grid, u_{1b} is the background velocity fluctuation (which exists in the wind tunnel irrespectively of the presence of the grid)

and u_{1n} is electronic noise (converted to an equivalent velocity fluctuation). Similarly, the instantaneous measured streamwise velocity fluctuation in the absence of any grid was expressed as

$$u_{1bm} = u_{1b} + u_{1n} \, . \tag{3.9}$$

Assuming that u_1, u_{1b} and u_{1n} were statistically uncorrelated to each other, expressions for the relationships between the various statistical properties of u_{1m} and u_1 were derived, and corrections were applied to variables derived from the corrected values. The statistical properties of u_{1n} were measured with the hot-wires operating in the wind tunnel without any flow and those of u_{1bm} were measured at each given mean speed without any grid inserted. For example, the corrected variance of the streamwise velocity fluctuations in stationary grid turbulence was found as

$$\overline{u_1^2} = \overline{u_{1m}^2} - \overline{u_{1bm}^2} \, , \tag{3.10}$$

while for non-stationary grid turbulence the expression for the corrected variance of the non-coherent fluctuations would be

$$\langle u_1^{*2}(t) \rangle = \langle u_{1m}^{*2}(t) \rangle - \langle u_{1bm}^{*2}(t) \rangle \, . \tag{3.11}$$

Expressions for the corrected statistical properties of grid-generated fluctuations and typical correction levels are presented in Appendix A.

In the previous analysis, it was assumed that u_1, u_{1b} and u_{1n} were statistically uncorrelated to each other. Nevertheless, it is possible that the operation of the fan resulted in some increase of the electronic noise and that background fluctuations reaching the grid influenced in some way the grid-generated turbulence. Any existing correlation among these properties would have some quantitative effect on the results, but the assumption of zero correlation among different types of fluctuations cannot be tested and decoupling of these fluctuations would be impossible. Considering the relatively low level of corrections and the order of magnitude differences between turbulent intensities in the steady flow and the conventional grid turbulence, it is assessed that any residual inaccuracy in the corrections would not change the qualitative observations.

3.4 Temperature measurement

Mean temperature measurements

A 100 Ω RTD probe (RDF Corp., Model 29348-T01-B-48) with a response specified by the manufacturer was used to monitor the flow temperature upstream of the heated source (Figure 3.12) in all stationary and non-stationary wind-tunnel studies. The local mean flow temperature in all stationary and non-stationary wind-tunnel studies was measured with a glass-coated thermistor probe (EPCOS(TDK), B57540 series, 10 kΩ, 1% RAD), connected to an in-house circuit that provided a low excitation current of 50 μA. The thermistor was calibrated against the RTD probe in a heated calibration jet (Don, 2016; Duong, 2017) and its reading was frequently compared to the RTD reading in the unheated flow in the wind tunnel and corrected, if necessary. The thermistor signal was fitted with a third-order polynomial (Figure 3.13).

Cold-wire measurements in the stationary-flow wind tunnel

The fluctuating temperature in the stationary-flow wind tunnel was measured with a cold-wire probe, having a platinum sensor with a diameter of 0.6 μm and a length-to-diameter ratio of 800, etched from Wollaston wire and spot-welded onto two prongs, which are part of the cross-wire probe (Figure 3.10) in all studies. The cold-wire was operated with a low noise and high gain home-made circuit, at a current of 0.1 mA.

The cold-wire was calibrated in the plume of a heated source against the thermistor reading and the calibration data were fitted by a linear function. It is noted that cold-wire signals are subject to significant drift and so they were only used for measuring temperature fluctuations and not mean temperature.

Figure 3.12: Photograph of the RTD used in this study.

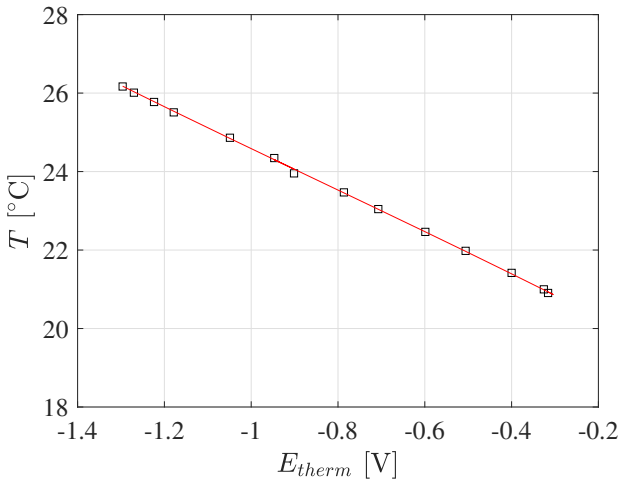

Figure 3.13: Example of thermistor temperature calibration. The black squares represent the measured RTD temperature and the red line represents the linear fit to the calibration data.

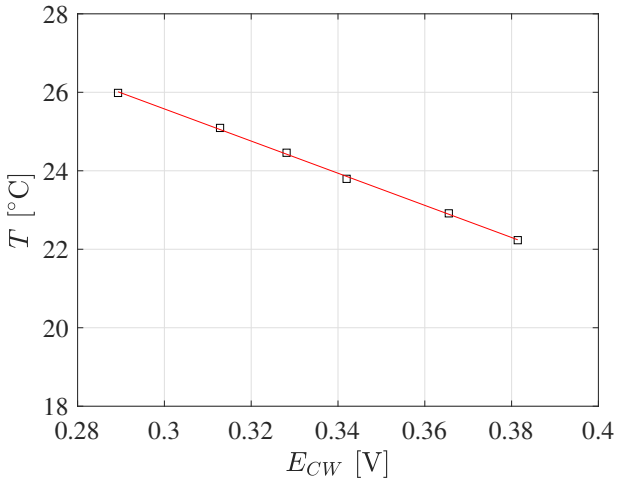

Figure 3.14: Example of cold-wire temperature calibration. The black squares represent the measured thermistor temperature and the red line represents the linear fit to the calibration data.

Attempts to use cold wires in the non-stationary wind tunnel

In general, heat transfer from an electrically heated sensor, such as a cold-wire, depends on both the local temperature and the local velocity (Tavoularis & Nedić, 2024). Provided that the sensor is sufficiently thin (the present sensor, which has a diameter of 0.6 μm, satisfies this condition), the current through the sensor is sufficiently small (the present current,

which is 0.1 mA satisfies this condition), and the flow speed is sufficiently large (typically larger than 4 m/s), the velocity sensitivity can be neglected and so the cold wire becomes a resistance thermometer. The present range of flow speeds; however, includes relatively small values, which made it necessary to investigate whether the cold-wire response was sensitive to velocity. For this test, the cold-wire was placed in the unheated, undisturbed flow in the wind tunnel and its output voltage E_{CW} was measured. The flow temperature was kept constant and equal to 20.8 °C. As Figure 3.15 shows, the voltage output was measurably sensitive to velocity for values lower than about 3.3 m/s, but this sensitivity became very strong only for speeds lower than about 1 m/s. For this reason, the use of a simple cold-wire calibration against temperature was deemed to be inappropriate and we spent substantial effort in trying to devise a method for correcting the cold-wire output.

First, we explored reducing the velocity sensitivity by decreasing the current further, but the value 0.1 mA was deemed to be the lower bound for which signal amplification noise would be tolerable.

Then, we explored the possibility of correcting the temperature reading by using the velocity measured by the hot wires that were adjacent to the cold wire. For simplicity, and considering that the ranges of temperature and velocity were relatively narrow, we

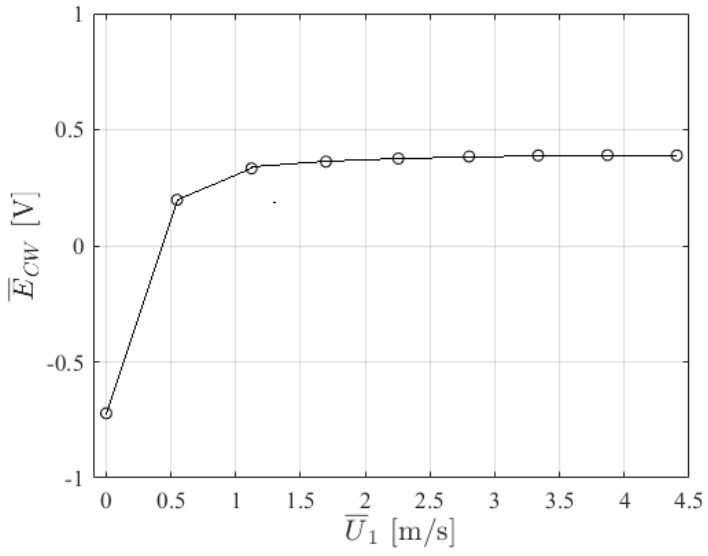

Figure 3.15: Cold-wire voltage output in a flow with a fixed temperature and different velocities.

linearised the cold-wire voltage output in the form

$$E_{CW}(U,T) = E_o + \alpha_U(U - U_{ref}) + \alpha_T(T - T_{ref}) \,, \tag{3.12}$$

where the values of E_o, α_U and α_T could ideally be determined by calibrating the sensor separately for temperature under a constant reference velocity and for velocity under a constant reference temperature. A likely source of error; however, is the considerable drift of the voltage output, which is a consequence of the large gain and offset used for signal amplification. Another, possibly prohibitive, source of error is heat conduction to the probe prongs. By comparison to the sensor, the prongs are quite thick and their temperature would vary measurably only in response to low-frequency fluctuations of the surrounding velocity and/or temperature. In the present pulsatile flow experiments, the flow pulsations had a frequency that was possibly sufficiently small to affect the prong temperature, especially in a heated flow. Under such conditions, the use of the previously presented static response would produce inaccurate results.

To test this hypothesis, we applied the previous expression to time dependent flows in the wind tunnel. We found that its prediction depended on the flow history, as the cold-wire voltage was different for accelerating and decelerating flows with the same instantaneous velocity. Moreover, we found that the level of correction depended on both the amplitude and the frequency of the pulsation. Other approaches to use the instantaneous velocity, measured with hot wires, for correcting the temperature measurement also led to inconsistent and unusable results.

We also considered a different approach, suitable for estimating statistical properties of the temperature in the heated flow by correcting them using corresponding statistical properties measured during the same phase in the cycle in the unheated flow. This approach appeared to produce more consistent results than the instantaneous correction approach, but its uncertainty was unknown and the corrected values became increasingly unreliable, as the streamwise distance from the grid increased and the temperature rise diminished.

In conclusion, the measurement of the fluctuating temperature with cold wires in the present pulsatile flows was deemed to be inaccurate and was aborted.

3.5 Stationary grid turbulence measurement procedures

In stationary and ergodic turbulent flows, one may define time averages, customarily denoted by an overline as, for example,

$$\overline{U}_i = \frac{1}{\Delta T}\int_0^{\Delta T} U_i(t)dt, \tag{3.13}$$

where the time interval ΔT is sufficiently large, typically equal to or larger than 100 integral time scales of the flow (to be defined in the following). The statistical analysis of the measurements was based on the commonly adopted approach of Reynolds decomposition, by which a fluctuating random property (*e.g.,* U_i) is decomposed into an average (*e.g.,* $\overline{U}_i$) and a fluctuation (*e.g.,* u_i), for example

$$U_i = \overline{U}_i + u_i. \tag{3.14}$$

Turbulent flows contain a wide range of motions ("eddies"), having different sizes. Through a mechanism called the energy cascade, kinetic energy is transferred mainly from larger eddies to smaller ones. The effects of friction become dominant for sufficiently small eddies, the kinetic energy of which is dissipated into heat. The size of turbulent motions is characterised by three distinct length scales, the integral length scale, the Taylor microscale and the Kolmogorov microscale. In the present experiments, the integral length scale L_1 is calculated as $L_1 = \overline{U_1}\mathcal{T}$, where the integral time scale $\mathcal{T}$ was determined by integrating the autocorrelation function R of the streamwise velocity to its first zero, namely, as

$$L_1 = \overline{U}_1\int_t^{t+\tau_0} R(\tau)d\tau, \tag{3.15}$$

where the autocorrelation coefficient is defined as

$$R(\tau) = \frac{\overline{u_1(t)u_1(t+\tau)}}{\overline{u_1^2(t)}}. \tag{3.16}$$

Using Taylor's frozen flow approximation, the Taylor microscale λ was calculated as

$$\lambda = \overline{U}_1\left(\frac{\overline{u_1^2}}{\overline{\partial u_1/\partial t^2}}\right)^{1/2}, \tag{3.17}$$

where the velocity derivative variances $\overline{(\partial u_1/\partial t)^2}$ and $\overline{(\partial^2 u_1/\partial t^2)^2}$ were calculated by extrapolating corresponding finite differences to a zero time lag. The turbulence Reynolds

number Re_λ was calculated as

$$\mathrm{Re}_\lambda = \frac{u_1' \lambda}{\nu} \tag{3.18}$$

where ν is the kinematic viscosity of air. The turbulent kinetic energy dissipation rate ε was estimated using the isotropic expression

$$\varepsilon = 15\nu \frac{\overline{u_1^2}}{\lambda^2}. \tag{3.19}$$

The Kolmogorov microscale η was then calculated as

$$\eta = \left(\frac{\nu^3}{\varepsilon}\right)^{1/4}, \tag{3.20}$$

and the dissipation parameter as

$$C_\varepsilon = \frac{L_1 \varepsilon}{(\overline{u_1^2})^{3/2}}. \tag{3.21}$$

Using the Reynolds decomposition method, the measured temperature can also be decomposed into its average ($\overline{T}$) and fluctuating (θ) components as

$$T = \overline{T} + \theta. \tag{3.22}$$

3.6 Pulsatile grid turbulence measurement procedures

3.6.1 Phase averaging

The statistical analysis of non-stationary flows is based on ensemble averaging, customarily denoted by angle brackets, as, for example, $\langle U_i \rangle$. If the members of the ensemble are quasi-periodic realisations of a flow under controlled external conditions, ensemble averages may also be called phase averages and can be computed by averaging corresponding repeat values at the same time with respect to the start of each realisation. For example, the phase-averaged streamwise velocity would be defined as

$$\langle U_i(t) \rangle = \frac{1}{N} \sum_{n=0}^{N-1} U_i(t + nT_{cyc}) \, , \; 0 \le t \le T_{cyc} \, , \tag{3.23}$$

where N is the total number of measured cycles and T_{cyc} is the period of the cycle. During each cycle period, the relative time in the cycle is defined as $\tau_p = t/T_{cyc}$, $0 \le \tau_p \le 1$. In quasi-periodic flows and in flows in which distinct coherent events recur regularly, one

may use the triple decomposition (Hussain & Reynolds, 1970, 1972; Reynolds & Hussain, 1972), as, for example for the instantaneous velocity $U_i(t)$,

$$U_i(t) = \langle U_i(t) \rangle + u_i^*(t) = \overline{U_i} + \widetilde{u}_i(t) + u_i^*(t) \ , \tag{3.24}$$

where $\langle U_i(t) \rangle$ is the ensemble-averaged velocity, $\widetilde{u}_i(t)$ is the zero-mean coherent fluctuations, and $u_i^*(t)$ is the zero-mean non-coherent fluctuations. The instantaneous fluctuation in a non-stationary pulsatile flow is

$$u_i(t) = \widetilde{u}_i(t) + u_i^*(t). \tag{3.25}$$

Figure 3.16 presents an example of a non-stationary pulsatile flow with the instantaneous, phase-averaged, and time-averaged velocities and instantaneous, coherent and non-coherent fluctuations.

The time-averaged variance of the instantaneous fluctuations is found as

$$\overline{u_i^2} = \overline{\widetilde{u}_i^2} + \overline{u_i^{*2}} + 2\overline{\widetilde{u}_i u_i^*}, \tag{3.26}$$

whereas the phase-averaged variance of the instantaneous fluctuations is found as

$$\langle u_i^2(t) \rangle = \langle \widetilde{u}_i^2(t) \rangle + \langle u_i^{*2}(t) \rangle + 2\langle \widetilde{u}_i u_i^*(t) \rangle. \tag{3.27}$$

Measurements of the covariance $2\langle \widetilde{u}_i u_i^*(t) \rangle$ were found to be of the order of 10^{-16} – 10^{-18} $\mathrm{m}^2/\mathrm{s}^2$ under different flow conditions with different grids; such values will be considered to be negligible in this work. The integral length scale $L_1(t)$ was calculated as $L_1(t) = \langle U_1(t) \rangle \mathcal{T}$, where the integral time scale $\mathcal{T}$ was determined by integrating the autocorrelation function $R(t)$ of the streamwise velocity to its first zero, namely, as

$$L_1(t) = \langle U_1(t) \rangle \int_t^{t+\tau_0} R(t, \tau) d\tau \ , \tag{3.28}$$

where the autocorrelation function is defined as

$$R(t, \tau) = \frac{\langle u_1(t) u_1(t + \tau) \rangle}{(\langle u_1^2(t) \rangle \langle u_1^2(t + \tau) \rangle)^{1/2}} \ . \tag{3.29}$$

Using Taylor's frozen flow approximation, the Taylor microscale $\lambda(t)$ was calculated as

$$\lambda(t) = \langle U_1(t) \rangle \left(\frac{\langle u_1^{*2}(t) \rangle}{\langle \partial u_1^* / \partial t \rangle^2} \right)^{1/2} , \tag{3.30}$$

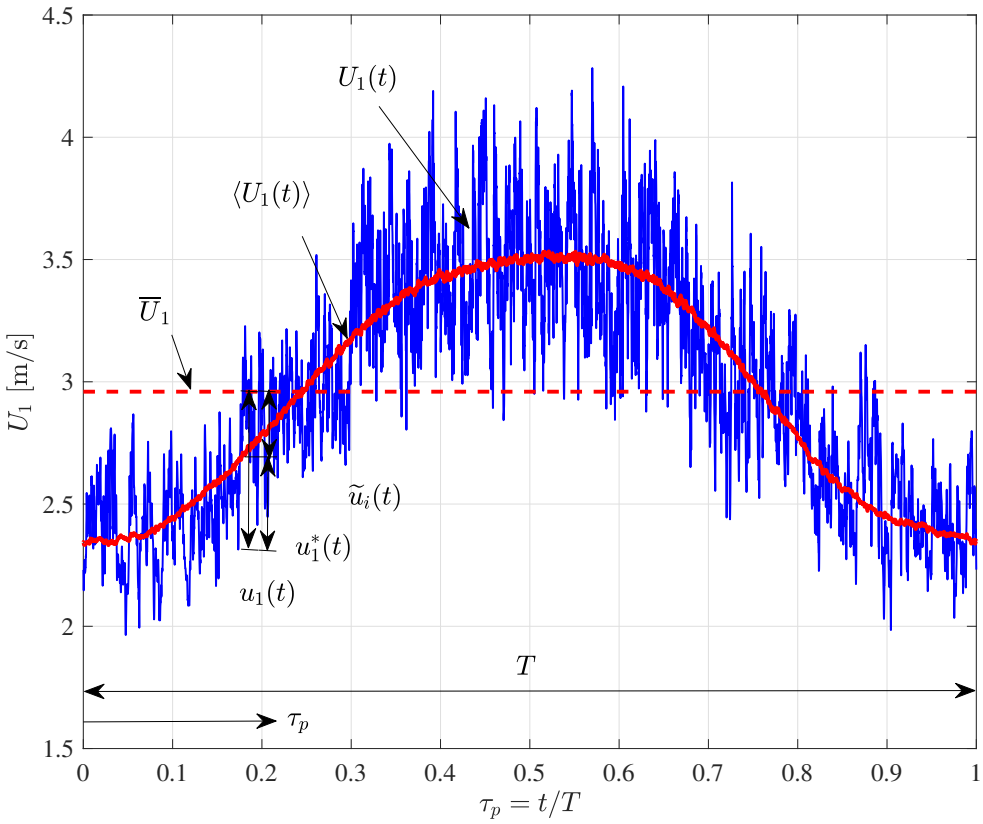

Figure 3.16: Example of a quasi-periodic flow cycle with the instantaneous (blue solid line), phase-averaged (red solid line), and time-averaged (red dashed line) velocities and instantaneous, coherent and non-coherent fluctuations.

where the velocity derivative variances $\langle \partial u_1^*/\partial t\rangle^2$ and $\langle \partial^2 u_1^*/\partial t^2\rangle^2$ were calculated by extrapolating corresponding finite differences to a zero time lag. The turbulence Reynolds number $\mathrm{Re}_\lambda(t)$ was calculated as

$$\mathrm{Re}_\lambda(t) = \langle U_1(t)\rangle \left(\frac{\langle u_1^{*2}(t)\rangle}{\langle \partial u_1^*/\partial t\rangle^2} \right)^{1/2} . \tag{3.31}$$

The turbulent kinetic energy dissipation rate $\varepsilon(t)$ was estimated using the isotropic expression

$$\varepsilon(t) = 15\nu \frac{\langle u_1^{*2}\rangle}{\lambda^2(t)} . \tag{3.32}$$

The Kolmogorov microscale $\eta(t)$ was calculated as

$$\eta(t) = \left(\frac{\nu^3}{\varepsilon(t)} \right)^{1/4} , \tag{3.33}$$

and the dissipation parameter as

$$C_\varepsilon(t) = \frac{L_1(t)\varepsilon(t)}{\langle u_1^{*2}\rangle^{3/2}} \,. \tag{3.34}$$

3.6.2 Convergence analysis

Convergence analyses were performed for the phase averages at different times in the pulsation cycle of the streamwise centreline velocity, standard deviation of the streamwise velocity fluctuations, Taylor microscale and Kolmogorov microscale. Results in Figure 3.17 show that the phase averages over 400 cycles converged sufficiently. Therefore, each reported measurement was averaged over at least 400 cycles.

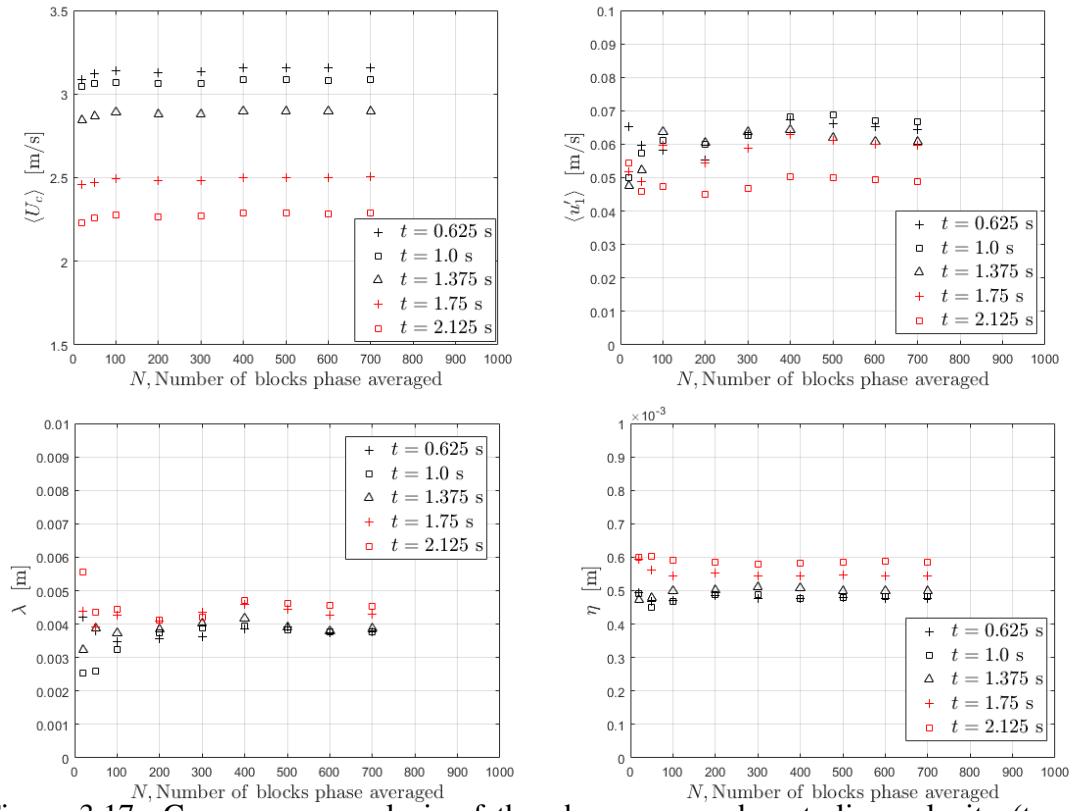

Figure 3.17: Convergence analysis of the phase-averaged centreline velocity (top-left), standard deviation of the streamwise velocity fluctuations (top-right), Taylor microscale (bottom-left) and Kolmogorov microscale (bottom-right) at different times in the pulsatile cycle.

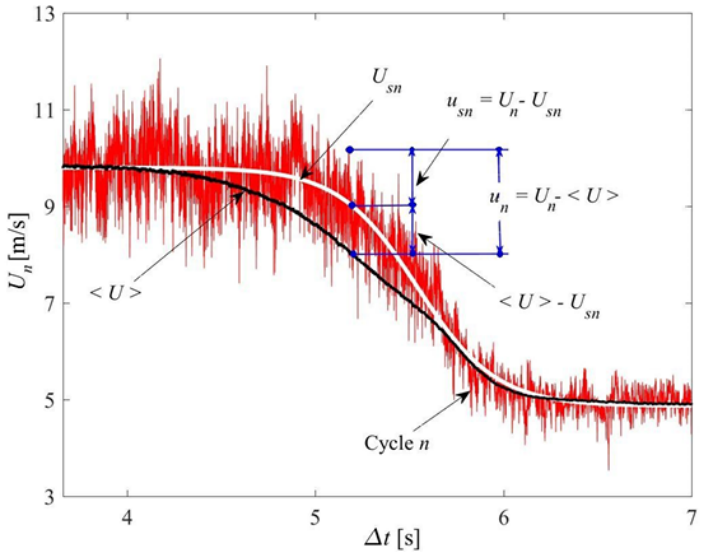

Figure 3.18: An example of a cycle-to-cycle variation, comparing the phase-averaged velocity (black line) and the velocity during an individual cycle (red line) during flow deceleration in previous work. Adapted from Duong (2017).

3.6.3 Cycle-to-cycle variations

In our previous work in a pulsatile turbulent flow through a rod bundle, we found that strong cycle-to-cycle variations led to unrealistic phase-averaged results (Duong, 2017), particularly during flow deceleration. For example, the uncorrected phase-averaged variance of the streamwise velocity was found have an error in excess of 900%. In that study, however, a large contributor to the cycle-to-cycle variations was an error in the program controlling the timing of the flap operation. An example of the effect of a cycle-to-cycle variation from Duong (2017) is presented in Figure 3.18.

This programming error was corrected for the present work and it was found that cycle-to-cycle variations were very small. Examples of a typical velocity cycle and the phase-averaged velocity during a full cycle at two different streamwise positions are presented in Figure 3.19. It is evident that the phase-averaged velocity coincides with a visually fitted line through the instantaneous measurements.

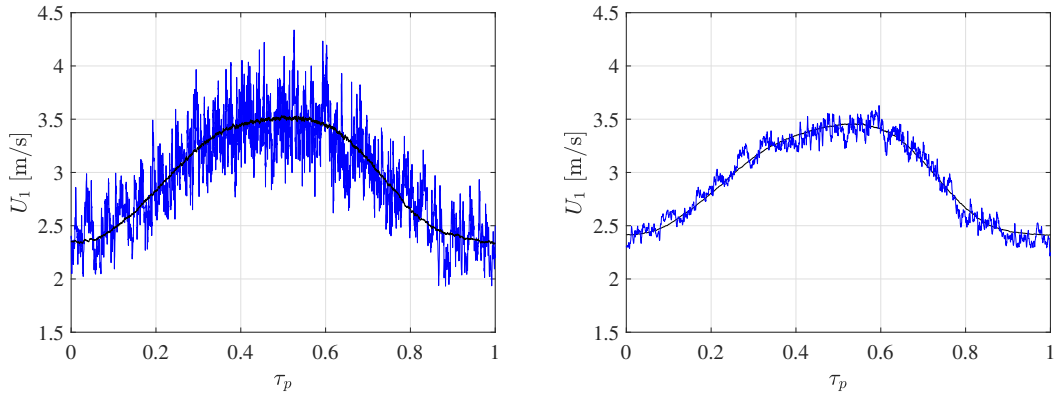

Figure 3.19: Comparison of the phase-averaged velocity (black line) and the velocity during a typical cycle (blue line) for the M51 grid at a) $x_1/M = 10$ and b) $x_1/M = 40$

3.7 Uncertainty analysis

The measurement uncertainty δ_x of a measured property x (*e.g.*, $\langle U_i \rangle$, $\langle u_i^2 \rangle$) is defined as

$$\delta_x = \sqrt{b_x^2 + p_x^2}\,, \tag{3.35}$$

where b_x is the bias limit and p_x is the precision limit of x (Tavoularis & Nedić, 2024).

All instrumentation and measurement procedures were designed to keep the uncertainty as low as possible. Probe supports were mounted firmly onto the traversing system to reduce mechanical vibration effects on the measured turbulence. It is well known that cross-wire probes are subject to error by cross-talk when the ratio of the separation distance to the length of the sensors is less than 0.15 (Jerome *et al.*, 1971); in this study this ratio was 0.59.

The effect of the hot-wire probe misalignment with respect to the incoming flow on the mean flow velocity was studied on the calibration jet for pitch angles ranging from -3° to 3°. Within this range, the measured mean flow velocity error ranged between 0.1 and 0.4%. When the probe was inserted in the test section, its axis formed an angle of less than 0.5° with the incoming flow and so the effect probe misalignment on the mean flow velocity was considered to be less than 0.2%.

Calibration error using the velocity-pitch-map was kept below 2% as much as possible, and common levels of calibration error were $0.3-0.4\%$ for $\overline{U_1}$ and $0.4-0.6\%$ for $\overline{U_2}$ in the higher-speed calibrations ($\overline{U_1} \geq 1.5$ m/s). In the lower speed calibrations ($\overline{U_1} \leq 1.0$ m/s),

the common error levels approached $1.3 - 1.6\%$ for $\overline{U_1}$ and $1.3 - 2.0\%$ for $\overline{U_2}$.

The effect of the linear actuator positioning was also examined; the actuator has a resolution of 0.02 mm, corresponding to a maximum uncertainty of 0.1% on the mean velocity.

The mini-thermistor probe used for temperature corrections was placed at approximately 25.4 mm away in the spanwise direction from the hot-wire, so that thermal and aerodynamic effects of the mini-thermistor on the hot-wire measurements would be considered negligible.

The precision limit was calculated as $p_x = 2\sigma_x/\sqrt{N}$, where σ_x is the standard deviation of an ensemble of repeat measurements of x and N is the number of measured points.

Wyngaard (1969) presented estimates of turbulent velocity derivatives in isotropic turbulence for four different hot-wire arrays. This analysis concluded that measurements of $\partial u_2/\partial x_1$ and $\partial u_1/\partial x_1$ with the present cross-wire would have errors of less than 3-4%. Furthermore, Ashok *et al.* (2012) showed that spatial filtering in the near-wall region of a wall-bounded flow has similar response to that of grid turbulence. Their work showed that the ratio of the sensor wire length to the Kolmogorov microscale scales well with the error estimates. In particular, they showed that, for a ratio less than 2, the effects of the spatial filtering would be negligible. In this study, the ratio of the sensor wire length to the Kolmogorov microscale varied between 2 and 2.5, which corresponds to an error of less than 2–3% for the streamwise velocity variance, 2–3% for the turbulent kinetic energy dissipation rate, 2% for the integral length scale and 1% for the Kolmogorov microscale.

The uncertainties of derived parameters (*e.g.*, the Taylor microscale and the Kolmogorov microscale) were estimated by standard statistical procedures (Tavoularis & Nedić, 2024). Tables 3.7 and 3.7 summarises the uncertainties of the measured and derived parameters. In the case of time-averaged properties, the lower values generally correspond to larger mean speeds ($\overline{U_1} = 3 - 4$ m/s) and the larger values correspond to smaller mean speeds ($\overline{U_1} = 0.4 - 0.6$ m/s). In the case of phase-averaged properties as well, the lower values generally correspond to larger mean speeds ($\langle U_1 \rangle = 3.5 - 3.6$ m/s), and the larger values generally correspond to smaller mean speeds ($\langle U_1 \rangle = 2.3 - 2.4$ m/s). In most cases, the uncertainty is relatively small, but it increases significantly as the velocity decreases to very low values. For the pulsatile measurements reported in this work, the largest contributor to the uncertainty of the phase-averaged properties was the precision uncertainty. Because

only 600 cycles of measurements were taken for each set of data, the precision uncertainty was at least 8.2% of the property's standard deviation. To reduce the precision uncertainty of the first- and second-order fluctuation derivatives in the pulsatile flow, the four nearest (±0.0005s) neighbours of the measurement point were used as part of the average, thus increasing the number of points to 6000 and decreasing the precision uncertainty to a minimum of 2.6% of the property's standard deviation. The flow in the pulsatile measurements for this work was always turbulent, and thus the bias uncertainty estimates remained small. When large biases were identified, they were removed by applying appropriate corrections to the directly measured properties, which propagated to the calculated properties, as outlined in Section 3.7.

Table 3.2: Typical levels of uncertainties of time-averaged measured properties.

property	Lower Bound (%)	Upper Bound (%)
$\overline{U_1}$	0.4	1.7
$\overline{u_1^2}$	0.7	1.8
$\overline{u_2^2}$	0.7	1.8
$\overline{\left(\frac{\partial u_1}{\partial t}\right)^2}$	< 3	< 3
$\overline{\left(\frac{\partial^2 u_1}{\partial t^2}\right)}$	< 5	< 5
λ	< 3	< 3
η	< 1	< 1
Re_λ	< 3	< 3
S	< 5	< 5
F	< 5	< 5

Table 3.3: Typical levels of uncertainties of phase-averaged measured properties.

property	Lower Bound (%)	Upper Bound (%)
$\langle U_1 \rangle$	8.2	8.2
$\langle u_1^2 \rangle$	10.3	12.3
$\langle u_2^2 \rangle$	10.3	12.3
$\langle \left(\frac{\partial u_1}{\partial t} \right)^2 \rangle$	4.0	5.2
$\langle \left(\frac{\partial^2 u_1}{\partial t^2} \right) \rangle$	5	5.6
λ	5	5.6
η	2.8	3.3
Re_λ	7.1	8.3

Chapter 4

Enhancement of turbulent mixing by a porous obstruction

This chapter contains the following article, which was published in the journal Physical Review Fluids on December 16, 2022.

Duong, D., & Tavoularis, S. (2022), "Enhancement of turbulent mixing by a porous obstruction", Phys. Rev. Fluids, 7(12), 124502.

The experiments described in this article implement a strategy for enhancing scalar mixing in decaying grid turbulence by introducing an array of cylinders (porous obstruction) close to the scalar source, as explained by Tavoularis & Nedić (2017). As a result of the introduction of the porous obstruction, the turbulent diffusion was drastically enhanced.

It is assessed that two distinct mechanisms contribute to the plume spreading enhancement: first the transverse deflection of part or all of the plume as it impacts on successive obstructions and second the additional transverse dispersion of scalar by the turbulence produced by the array elements, which is superimposed on and coupled with the grid-generated turbulence. Although it is not possible to separate the two effects with the present setup, one may do so by conducting additional experiments with different types of obstructions. One issue worth investigating is the effect of changing obstacle porosity, which can be achieved by changing the spacing and arrangement geometry of the elements, including a case with a zero porosity, which corresponds to a solid obstruction (e.g., a solid wedge).

Enhancement of turbulent mixing by a porous obstruction

Dana Duong and Stavros Tavoularis*
Department of Mechanical Engineering, University of Ottawa, Ottawa, Ontario, Canada K1N 6N5

(Received 10 August 2022; accepted 28 November 2022; published 16 December 2022)

Turbulent diffusion and mixing of heat, introduced passively by a thin ribbon in grid-generated turbulence, were enhanced drastically by a small array of thin cylinders, positioned closely downstream of the ribbon. A multistructure flow region was formed behind the array and relaxed towards grid turbulence, albeit maintaining a turbulence intensity and an integral length scale that were twice as large as those in the absence of the array.

DOI: 10.1103/PhysRevFluids.7.124502

I. INTRODUCTION

Turbulent mixing and diffusion of scalar properties, such as heat and the concentration of an admixture, have been studied extensively, due to their importance in combustion, chemical reactions, spreading of pollutants, and transmission of airborne pathogens [1,2]. Much of our understanding of these phenomena has been based on studies under idealized conditions [3–26], but such findings are also relevant to many practical conditions. Early studies of scalar dispersion from concentrated sources in homogeneous turbulence [27,28] have been adapted to estimate the far-field half-width of a scalar plume, generated by a line source in a uniform stream, as

$$\sigma \approx (2u_2' L_2 x_1/\overline{U_1})^{1/2} \quad \text{for } \sigma \gg L_2, \tag{1}$$

where x_1 is the distance from the source, $\overline{U_1}$ is the mean velocity, u_2' is the standard deviation of the transverse turbulent velocity, and L_2 is the transverse integral length scale. More recently, scalar diffusion theory was extended to account for turbulence decay, as would be the case for grid-generated turbulence [29]. In this case, the far-field plume half-width was estimated as

$$\sigma \propto C_\varepsilon^{-1/2} L_1, \tag{2}$$

where L_1 is the streamwise integral length scale and the dissipation parameter is defined in terms of L_1, the turbulent kinetic energy per unit mass k, and its dissipation rate ε as

$$C_\varepsilon = \varepsilon L_1/(2k/3)^{3/2}. \tag{3}$$

In isotropic turbulence, $L_2 = L_1$, but, in shear flows, one may generally expect that $L_1 > L_2$. Nevertheless, the scale L_1 was used in Eq. (2) instead of L_2, because the former is easier to measure, as well as being less sensitive to local inhomogeneity.

In grid turbulence, there is a developing flow region near the grid, where C_ε grows monotonically, followed by a partially developed region and finally a fully developed region, where C_ε is approximately constant [21,29]. Equation (2) implies that, if the far-field condition ($\sigma \gg L_1$) is satisfied at the start of the $C_\varepsilon \approx$ const region, it will continue being satisfied further downstream, so that the plume will grow at the same rate as the turbulence scale does. The analysis also indicates

*stavros.tavoularis@uottawa.ca

that, if the far-field condition is not satisfied at the start of the $C_\varepsilon \approx$ const region, it will never be satisfied and the plume will keep growing at a slower rate than L_1 does. Based on these observations, one may develop the following strategy for enhancing the spreading of the plume, thus improving scalar mixing in decaying grid turbulence: Introduce a disturbance close to the source, so that the plume will be wide enough to satisfy the far-field condition early in its evolution and then keep growing at its highest possible rate, which is the rate of growth of L_1. The choices of geometry and location of the grid, the scalar source, and the obstructions are crucial in implementing this strategy as efficiently as possible. In the following, we will outline the rationale for making the present choices.

First, we chose a grid. We need a grid that has a developing region that is sufficiently long to contain the obstructions, as well as a fully developed region that is sufficiently long for the plume growth to be observable within the wind-tunnel test section. When the grid mesh size M is relatively small, the developing region is essentially nonexistent [21], whereas, when M is relatively large, the highest dimensionless distance x_1/M attainable within the wind-tunnel test section would be small (thus restricting the length of the fully developed region), with the problem compounded by excessive boundary layer interference with the grid turbulence. Among the many grids that were available from previous studies in our laboratory, the one that generated a sizable developing region, a sizable fully developed region, and a core flow that was relatively free of wall effects was found to be a square-mesh perforated plate with a mesh size $M = 50.8$ mm.

In accordance with the previously explained strategy, we placed the scalar source as closely as possible downstream of the perforated plate. In fact, we mounted both the perforated plate and the source on the same frame that was inserted in the wind tunnel. An ideal line source of a scalar would introduce no disturbance to the flow, but such a source would also generate a very narrow plume, which is against the present strategy. Instead of a thin wire, which would approximate a line source, we used a thin ribbon as a source of heat and imposed a twist on it, such that it would introduce a sizable early plume. Of course, we anticipated that the wake generated by the ribbon may also introduce a relatively strong disturbance to the grid turbulence and, consequently, deviation from the conditions that are necessary for the previous plume spread theory to be accurate. Nevertheless, this choice of source appears to be justified, when we consider that our objective is to generate a plume that is as wide as possible near its origin and that grid turbulence would anyway be distorted by the obstruction to be placed downstream of the source.

Following our strategy to widen the plume as far upstream as possible, we placed the obstruction closely downstream of the source. The final, but very crucial, choice was the geometry of the obstruction. If we had introduced a relatively large solid obstruction in the scalar plume, we would have diverted the plume away from the source plane but would have also created a large, scalar-free, wake region. Moreover, the turbulence structure in the wake would be very different from grid turbulence, and the analysis would not hold, even approximately. After considering different possibilities, we decided to use an array of small cylinders, which would act as a porous obstruction, thus allowing the scalar to penetrate the array as well as reducing the disturbance to the grid turbulence. Of course, the turbulence structure behind the array would have contributions from the upstream grid turbulence, as well as contributions of the wakes of the cylinders and the high-speed flows between them. Consequently, this region will have a structure that is the result of more than one distinct turbulence generation mechanism and may be described as multistructure turbulence [30]. To minimize the overall flow disturbance and the pressure drop through the obstruction array, we designed the array such that, instead of being rectangular, it was contained in a triangular envelope, with its apex occupied by a single cylinder facing the source and followed by rows of staggered cylinders, increasing in number. Also to keep the obstruction disturbance relatively small, we set the height of the array to be smaller than the mesh size.

The general goal of this research is to devise a practical method for enhancing scalar mixing in a turbulent flow. In particular, we wished to widen the plume generated by a scalar line source in grid turbulence by inserting a porous obstruction closely behind it. We also wished to explore the

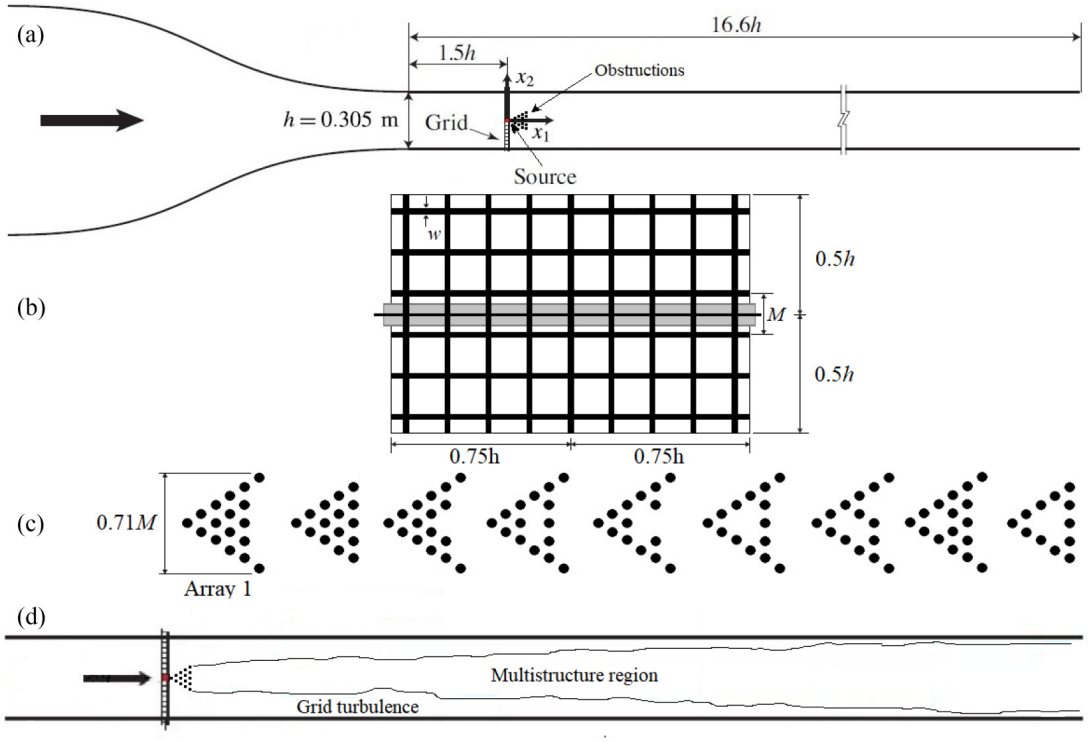

FIG. 1. Sketches of (a) a side view of the general experimental arrangement, (b) a view from upstream of the perforated plate bars (thick black lines), the obstruction projected frontal area (gray rectangle), and the heating ribbon (thin black horizontal line), (c) side views of the different cylinder arrays, and (d) a side view of the different flow regions. The different parts of this figure have different scales.

relationship between the plume spread and the turbulence properties in the multistructure region behind the obstruction.

II. APPARATUS AND MEASUREMENT PROCEDURES

The experiments were performed in an open-circuit wind tunnel, shown schematically in Fig. 1(a). The test section has a height $h = 305$ mm, a width of $1.5h$, and a length of $16.6h$. Beyond a certain initial length, the test section sidewalls were adjusted to be slightly diverging, to compensate the mean pressure field for boundary layer growth. A square-mesh perforated plate ["grid," shown in Fig. 1(b)], machined from a 16-gauge steel sheet with a thickness of 1.59 mm and having a mesh size $M = 50.8$ mm ($=0.167h$) and a solid bar width $w = 6.8$ mm (thus a solidity of 0.25), was inserted across the flow. An electrically heated ribbon, made of Nichrome alloy and having a thickness of 0.13 mm and a width of 1.59 mm, was inserted at a location that was 25.4 mm ($=0.50M$) downstream of the grid, to serve as the source of a passive scalar (i.e., temperature rise). The ribbon was twisted by approximately 30°, end to end, with respect to the horizontal plane. The heating power was the same for all reported tests. Arrays of ceramic rods, 3.2 mm in diameter and spaced by 5.5 mm, axis to axis, in equilateral arrangements, were positioned 38 mm ($=0.75M$) downstream of the source, namely, about $1.25M$ downstream of the grid. Each rod spanned the entire width of the test section, and the maximum projected height of the arrays was 36.2 mm, which is equal to $0.71M$. Measurements with the ribbon heated were taken following a warm-up time of 15 min to ensure that the rods had reached constant temperatures. Tests were performed for the nine array configurations that are shown in Fig. 1(c).

Measurements of the streamwise and transverse (i.e., vertical) velocity components and the fluctuating temperature were made with a homemade, three-wire probe. The velocity sensors, arranged in a cross-wire configuration, were made of tungsten and had a diameter of 2.5 μm, a sensing length of 0.85 mm, and a separation distance of 0.5 mm. The length-to-diameter ratio was 340, which is sufficiently large for end conduction effects to be negligible [31]. The temperature sensor ("cold wire") was made of platinum and had a diameter of 0.6 μm and a length-to-diameter ratio of 800; this sensor was etched from Wollaston wire and spot welded onto the prongs. The cold wire was supplied with a current of 0.3 mA by a low-noise, high-gain homemade circuit. The mean temperature close to the three-wire probe was measured with a miniature thermistor. The hot-wire signals were corrected for temperature effects, using an instantaneous temperature value that was the sum of the time-averaged temperature, measured with the thermistor, and the mean-free temperature fluctuation, measured with the cold wire. The reported temperature rise in the heated flow was the difference between the locally measured temperature and the temperature upstream of the heated source, measured with a precalibrated resistance temperature detector (RTD). The hot-wire and cold-wire signals were low-pass filtered with analog filters, having cutoff frequencies of 14 and 4 kHz, respectively, digitized at a rate of 30 kHz and recorded over 30 s for each test. The cross-wire probe was calibrated *in situ* using a velocity-pitch-map calibration method [32].

The streamwise integral time scale T_1 was determined by integrating the temporal autocorrelation coefficient of the streamwise velocity fluctuations to its first zero crossing. The streamwise integral length scale was then estimated as $L_1 = T_1\overline{U_1}$. The derivative $\overline{(\partial u_1/\partial t)^2}$ was calculated by extrapolating corresponding finite differences to a zero time lag. The Taylor microscale was calculated with the use of Taylor's frozen flow approximation as $\lambda = \overline{U}_1[u_1'^2/\overline{(\partial u_1/\partial t)^2}]^{1/2}$, and the turbulence Reynolds number was calculated as $\mathrm{Re}_\lambda = u_1'\lambda/\nu$, where ν is the kinematic viscosity of air. Lastly, the Taylorian diffusivity was calculated as $D = u_2'^2 L_1/2$.

III. RESULTS AND DISCUSSION

All measurements were taken at a fixed inlet velocity of $U_\infty = 10.0$ m/s, calculated from the mean pressure difference across the wind-tunnel contraction. In the absence of a grid, heating source, and flow obstructions, velocity fluctuations in the streamwise and transverse directions were found to be about 0.1%. The Reynolds number, based on the grid mesh size, was $\mathrm{Re}_M = U_\infty M/\nu \approx 34\,000$.

Preliminary measurements downstream of each of the nine cylinder arrays showed that, consistently with previous work [21,33], the mean temperature profiles had a nearly Gaussian shape. The peak of the obstructed temperature profile was substantially lower than that in unobstructed grid turbulence, while the plume was substantially wider. The additional spread of heat in the presence of the obstruction is attributed to two interacting, but distinct, effects. First, the warm wake of the source is either split by the first cylinder or diverted towards one side of it, in both cases tending to displace heated fluid away from the source plane. This process is repeated, as the displaced warm fluid reaches the second and subsequent cylinders. One is also reminded that the near field of a square-mesh grid consists of square jets, surrounded by short horizontal and vertical wakes, so that the flow reaching the obstruction is strongly three dimensional. Second, the cylinders produce additional turbulent fluctuations, which are superimposed on the grid turbulence, as well increasing the size of the energy-containing motions; both effects enhance turbulent diffusion. The effect of the obstructions on the plume spread is quite strong, despite the fact that the frontal projection of a full cylinder array is merely $0.076h$ in height.

Most effective in reducing the peak temperature rise was array 1, and so all measurements reported here were taken for this configuration. Profiles of the mean temperature rise $\Delta\overline{T}$ at three streamwise stations are shown in Fig. 2. These values have been normalized by a constant reference temperature rise $\Delta T_{\mathrm{ref}} = 0.44$ K, which is equal to the peak mean temperature rise in the unobstructed flow at $x_1/M = 6$. Although the unobstructed plume extended entirely within the flow core region (namely, it did not reach the boundary layers along the top and bottom walls), the

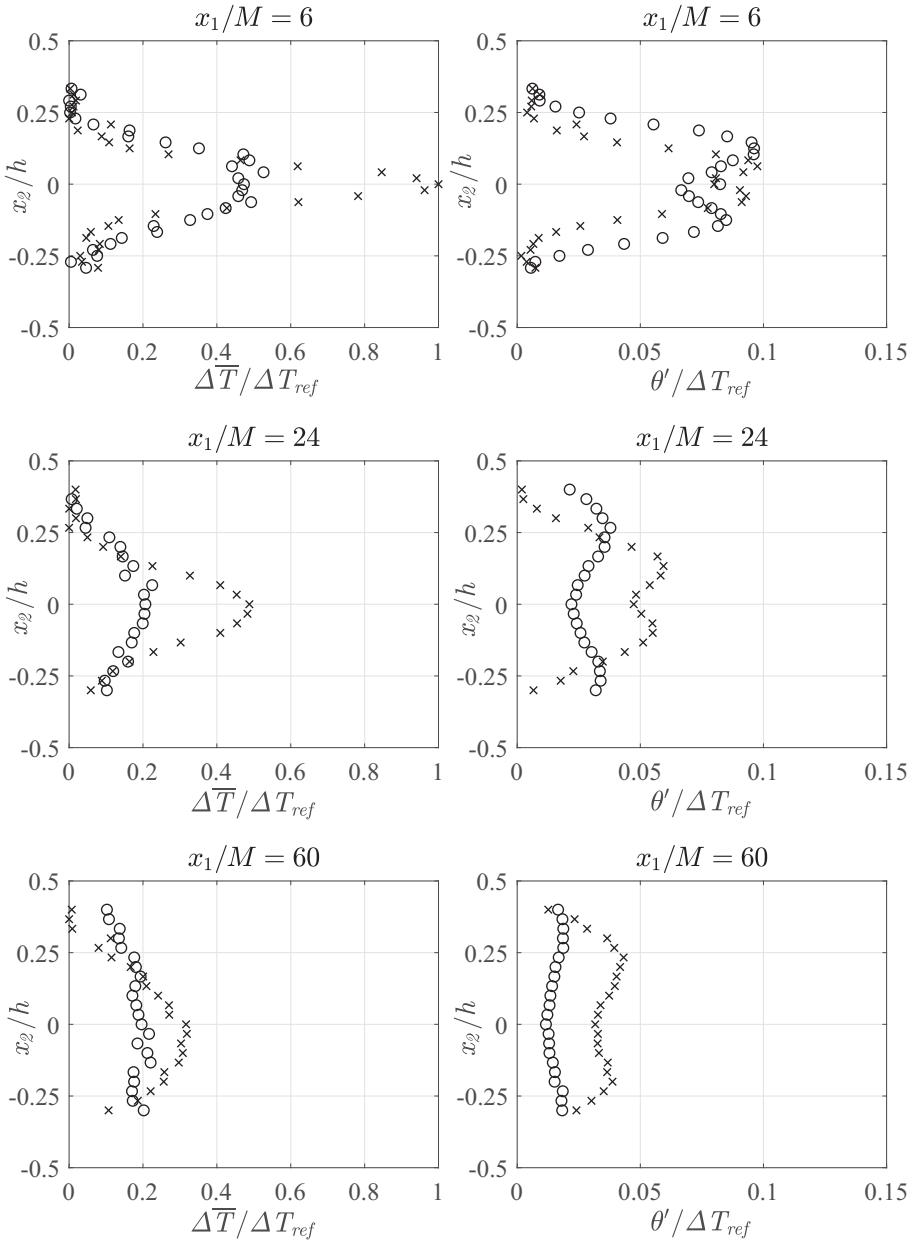

FIG. 2. Normalized mean temperature and temperature fluctuation profiles without (×) and with (○) the obstructions at three streamwise locations; the reference temperature rise was $\Delta T_{\text{ref}} = 0.44$ K.

obstructed plume grew wider than the core, encroaching into the boundary layers at the furthest station, where $x_1/M = 60$. Figure 2 also presents the transverse profiles of the normalized standard deviation θ' of the temperature fluctuations, at the same three streamwise locations. Dual peaks can be seen in both the unobstructed and obstructed flows, but, in the obstructed flow, the fluctuations spread further in the transverse direction and had a smaller nonuniformity. As shown in Fig. 3, the obstructed plume was roughly twice as wide as the unobstructed one. Figure 2 indicates that the obstruction intensified scalar mixing to the point that, roughly speaking, the mean temperature rise in the entire test section far away from the source exceeded half of its peak values in the

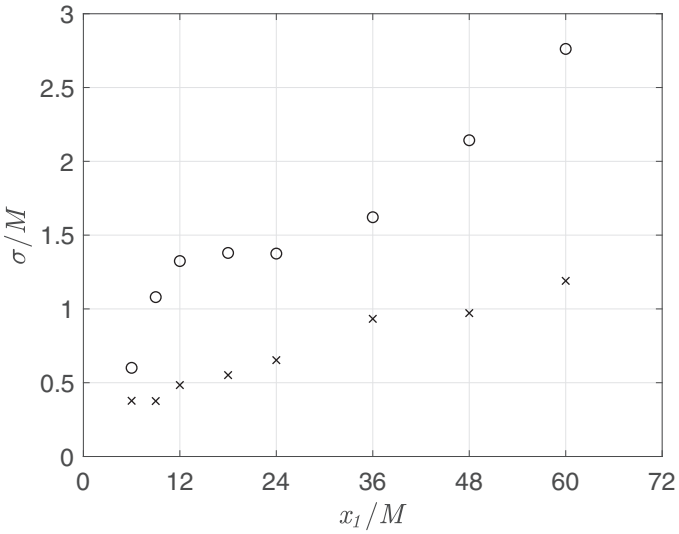

FIG. 3. Plume spread without (×) and with (○) the obstructions.

unobstructed case. In contrast, throughout the unobstructed flow, there were significant parts of the test section where there was no temperature rise at all. All things considered, we may confidently assert that the obstruction was quite effective in spreading and mixing the scalar.

To understand the effect of the obstructions, we compared the turbulence properties in their presence with those in their absence. Measured values of turbulence properties along the centerline, without and with the cylinder array, are listed in Table I, and representative vertical profiles of such properties are shown in Fig. 4. It should be noted that the various profiles near the grid are not expected to be two dimensional, but to have significant spanwise nonuniformity, generated by the vertical bars of the grid and the ribbon twist. It is also noted that the heating ribbon had a

TABLE I. Values of various properties at selected locations along the centerline; the values of P are at $x_2/h = 0.125$, where this property was at or near its peak.

	Grid only			Grid + array 1		
x_1/M	6	24	60	6	24	60
$\Delta T/\Delta T_{\text{ref}}$	1	0.488	0.317	0.473	0.206	0.196
$\theta'/\Delta T_{\text{ref}}$	0.160	0.095	0.063	0.164	0.044	0.023
σ/M	0.378	0.653	1.19	0.601	1.375	2.762
$\overline{U_1}/U_\infty$	0.857	0.949	0.967	0.701	0.903	0.941
u_1'/U_∞	0.094	0.035	0.020	0.165	0.068	0.036
u_2'/U_∞	0.080	0.032	0.018	0.198	0.065	0.030
$-\overline{u_1u_2}/u_1'u_2'$	0.017	−0.119	−0.114	0.000	0.005	−0.001
L_1/M	0.227	0.363	0.508	0.291	0.732	0.936
D (m^2/s)	0.004	0.001	0.0004	0.029	0.007	0.002
λ/M	0.029	0.178	0.339	0.029	0.179	0.337
Re_λ	89	68	67	158	132	117
P (m^2/s^3)	11.0	0.40		42	1.8	
$-S$	0.36	0.42	0.40	0.53	0.43	0.50
F	5.4	5.0	4.4	7.3	6.5	5.6

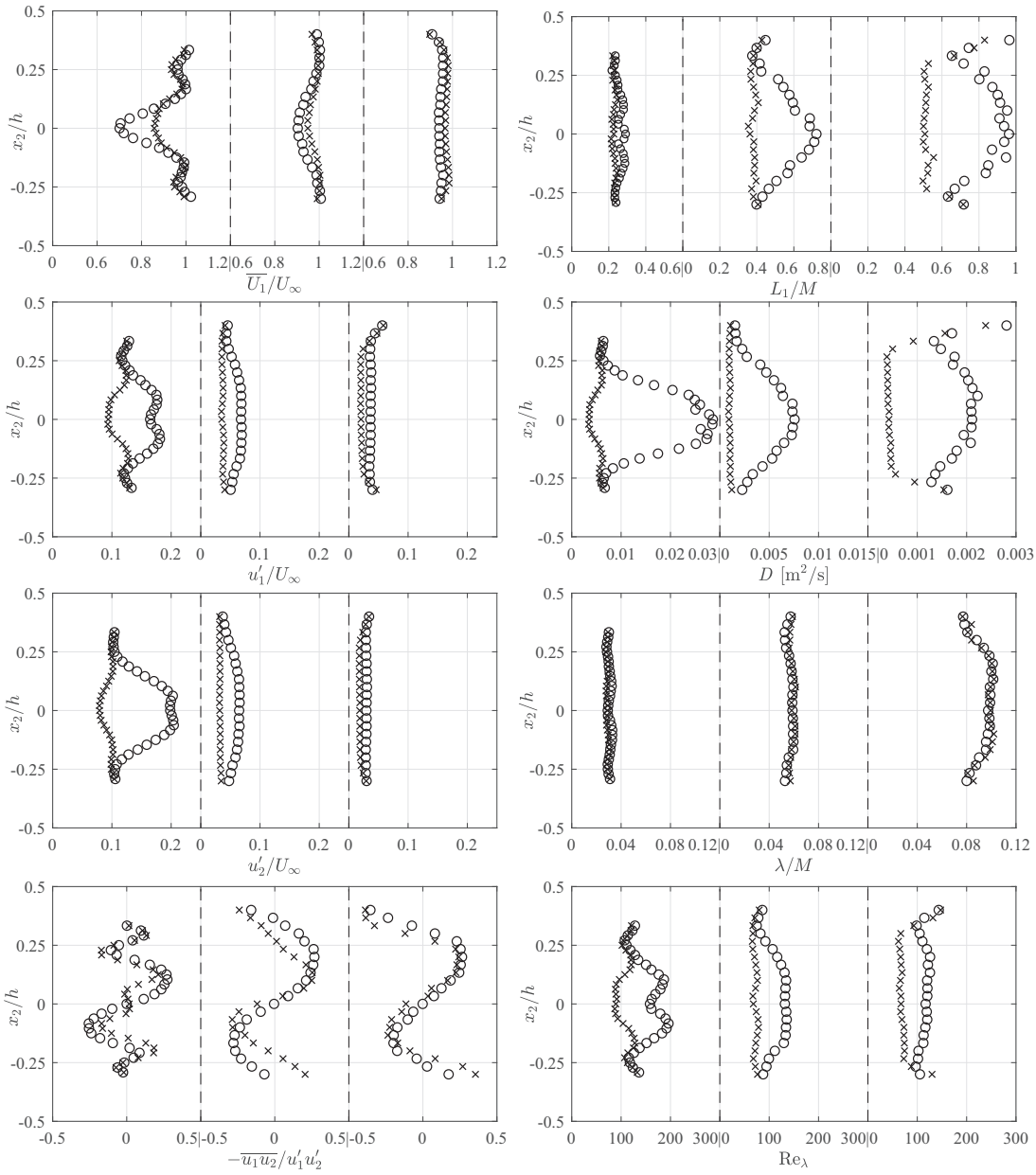

FIG. 4. Transverse profiles of the main turbulence properties without (×) and with (○) the obstructions at three streamwise locations; the axis scales for L_1 and D at each location have been adjusted to make the values readable.

measurable momentum wake, although we found no signs of buoyancy effects due to the heating. The main observations that can be based on these results are summarized as follows.

(a) Closely downstream of it, the obstruction increased the mean velocity deficit along the centerline to a level that was well above the already significant level in the absence of the obstruction, which is attributed to the grid bars and the ribbon wake. This deficit diminished with downstream distance, so that the mean flow in the core became nearly uniform at $x_1/M = 60$. At that location, the boundary layers on the top and bottom walls may be seen to occupy roughly a quarter of the

cross section each, with very weak velocity peaks persisting at the boundary layer edges; these peaks are interpreted to be remnants of upstream flow maxima between bar-generated wakes.

(b) The streamwise turbulent velocity fluctuation level behind the obstruction was nearly twice the unobstructed value in the entire test section, which means that the obstruction generated a permanent increase in turbulence level.

(c) The transverse turbulent velocity fluctuations behind the obstruction followed the same overall patterns as the streamwise fluctuations. It is interesting to note that, at $x_1/M = 6$, u_2' was somewhat larger than u_1', as the obstruction diverted flow away from the centerline. Further downstream, the ratio u_1'/u_2', both without and with obstructions, settled at a level in the range 1.1–1.2, which is somewhat larger than typical values in turbulence generated by grids with solidities that are higher than the present one [34]. In the near-wake of the obstruction, the turbulence intensity $u_1'/\overline{U_1}$ exceeded 20%. This brings into question the validity of Taylor's frozen flow approximation, but we note that a recent study on this issue [35] concluded that Taylor's approximation stands for $u_1'/\overline{U_1} \lesssim 25\%$.

(d) Unlike isotropic turbulence, the present flow had a measurable Reynolds shear stress, which is attributed to the combined wakes of the ribbon and the obstruction. The shear stress correlation coefficient was only mildly affected by the obstruction. It is interesting to note that, without and with the obstruction, this coefficient was negligible along the streamline and reached peak values of about ± 0.25 at about $x_2/h \approx \pm 0.125$, which points to persisting mild inhomogeneity and anisotropy throughout the measuring section. The peak shear stress correlation coefficient was smaller in magnitude than its value in outer turbulent boundary layers and in uniformly sheared turbulence, where it is about 0.4.

(e) In view of the appreciable mean shear and shear stress in parts of the flow, we examined the turbulence production $P = -\overline{u_1 u_2} d\overline{U_1}/dx_2$. In both the unobstructed and obstructed flows, P was negligible along the centerline, but it reached distinct peaks at about $x_2/h \approx \pm 0.125$. The peak production was up to a third of a corresponding rough estimate of the local turbulent kinetic energy dissipation rate and up to nearly half the dissipation value in the obstructed flow. By comparison, the production-to-dissipation ratio in uniformly sheared turbulence is about two-thirds [18].

(f) The obstruction nearly doubled the integral length scale, and such increase was maintained downstream.

(g) The obstruction increased drastically the turbulent diffusivity $D \approx u_2'^2 L_1/2$ in its wake. Close to the obstruction, the increase was by an order of magnitude and peaked on the centerline, but, further downstream, the turbulent diffusivity maintained a fairly uniform value in the flow core, which was roughly four times the corresponding unobstructed value. This increase in D is consistent with the drastic enhancement of scalar mixing.

(h) The Taylor microscale was essentially unaffected by the obstruction; this indicates that the obstruction increased both the velocity fluctuations and their temporal derivative by the same amount. Nevertheless, there was a very small correlation ($\lesssim 0.1$ for $x_1/M \geqslant 24$) between the velocity and its derivative. A physical justification for the lack of influence of the obstruction on the Taylor microscale remains to be found.

(i) The turbulence Reynolds number was roughly doubled by the obstruction, as a result of the increase of the turbulence level.

(j) As a final note, Fig. 5 shows representative profiles of the skewness S and flatness F factors of the streamwise velocity derivative, which are indicators of the fine structure. Away from the grid ($x_1/M \geqslant 24$), S takes values in the vicinity of -0.5 in both the unobstructed and the obstructed flows; such values are typical for fully developed turbulence at moderate Reynolds numbers [36–40]. However, closer to the grid ($x_1/M = 6$), S takes values that are measurably lower than the value -0.5 without the obstruction and closer to -0.5 with the obstruction; thus it appears that the effect of the obstruction is to accelerate the development of the turbulence structure. Moreover, the obstruction increases systematically the flatness factor throughout the test section, which is consistent with the increase in Re_λ and indicates an enhancement of the internal intermittency of the turbulence. It should be noted that, at the furthest downstream station ($x_1/M = 60$), the

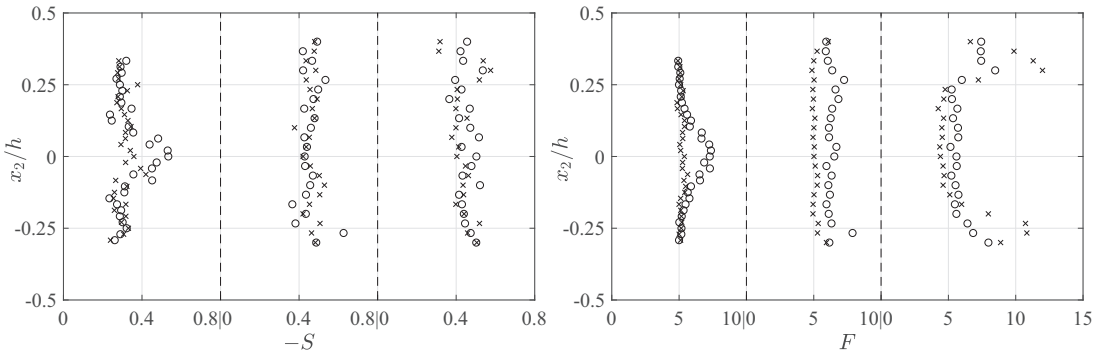

FIG. 5. Transverse profiles of the skewness and flatness factors of the streamwise velocity derivative without (×) and with (○) the obstructions. The axis scale of F at each location has been adjusted to make the values readable.

flatness factor is drastically larger outside the flow core ($|x_2/h| > 0.25$) than within the core $-0.25 \leqslant x_2/h \leqslant 0.25$; this is attributed to the intermittency between grid turbulence and turbulence in the boundary layers developing along the test section walls.

IV. CONCLUSIONS

In this paper, we found that a small array of thin cylinders, acting as a localized, porous, flow obstruction, enhanced drastically turbulent diffusion and mixing of a passive scalar injected from a line source in grid turbulence. The unobstructed scalar plume was confined within the test section core region, whereas the obstructed plume penetrated the boundary layers on the test section walls. This is further confirmed by the fact that the plume spread in the obstructed flow was twice as large as that in unobstructed grid turbulence. Transverse profiles of turbulence properties indicated that a multistructure flow region was formed behind the array and relaxed towards grid turbulence, albeit maintaining permanent increases in turbulence level, integral length scale, and turbulent diffusivity.

ACKNOWLEDGMENT

Funding for this research was provided by the Natural Sciences and Engineering Research Council of Canada, Grant No. RGPIN-2017-03835.

[1] P. E. Dimotakis, Turbulent mixing, Annu. Rev. Fluid Mech. **37**, 329 (2005).
[2] Z. Warhaft, Passive scalars in turbulent flows, Annu. Rev. Fluid Mech. **32**, 203 (2000).
[3] E. Germaine, L. Mydlarski, and L. Cortelezzi, Evolution of the scalar dissipation rate downstream of a concentrated line source in turbulent channel flow, J. Fluid Mech. **749**, 227 (2014).
[4] U. Karnik and S. Tavoularis, Measurements of heat diffusion from a continuous line source in a uniformly sheared turbulent flow, J. Fluid Mech. **202**, 233 (1989).
[5] G. I. Taylor, Statistical theory of turbulence. Parts I–IV, Proc. R. Soc. London A **20**, 151 (1935).
[6] S. P. Arya, *Air Pollution Meteorology and Dispersion* (Oxford University Press, Oxford, 1999), Vol. 6.
[7] D. R. Webster, P. J. W. Roberts, and L. Ra'ad, Simultaneous DPTV/PLIF measurements of a turbulent jet, Exp. Fluids **30**, 65 (2001).
[8] D. R. Webster, S. Rahman, and L. P. Dasi, Laser-induced fluorescence measurements of a turbulent plume, J. Eng. Mech. **129**, 1130 (2003).

[9] S. Rahman and D. R. Webster, The effect of bed roughness on scalar fluctuations in turbulent boundary layers, Exp. Fluids **38**, 372 (2005).
[10] I. Nakamura, Y. Sakai, and H. Tsunoda, On conditional statistics of the diffusion field of matter by a point source plume in uniform mean shear flow, JSME Int. J. Ser. II **32**, 180 (1989).
[11] A. Borg, J. Bolinder, and L. Fuchs, Simultaneous velocity and concentration measurements in the near field of a turbulent low-pressure jet by digital particle image velocimetry–planar laser-induced fluorescence, Exp. Fluids **31**, 140 (2001).
[12] K. Sakakibara, J. Hishida, and M. Maeda, Vortex structure and heat transfer in the stagnation region of an impinging plane jet (simultaneous measurements of velocity and temperature fields by digital particle image velocimetry and laser-induced fluorescence), Int. J. Heat Mass Transfer **40**, 3163 (1997).
[13] R. A. Lavertu and L. Mydlarski, Scalar mixing from a concentrated source in turbulent channel flow, J. Fluid Mech. **528**, 135 (2005).
[14] H. Stapountzis, B. L. Sawford, J. C. R. Hunt, and R. E. Britter, Structure of the temperature field downwind of a line source in grid turbulence, J. Fluid Mech. **165**, 401 (1986).
[15] C. Vanderwel and S. Tavoularis, Measurements of turbulent diffusion in uniformly sheared flow, J. Fluid Mech. **754**, 488 (2014).
[16] M. S. Anand and S. B. Pope, Diffusion behind a line source in grid turbulence, in *Turbulent Shear Flows 4*, edited by L. Bradbury, F. Durst, B. Launder, F. Schmidt, and J. Whitelaw (Springer, New York, 1985), pp. 46–61.
[17] J. Lepore and L. Mydlarski, Lateral dispersion from a concentrated line source in turbulent channel flow, J. Fluid Mech. **678**, 417 (2011).
[18] S. Tavoularis and S. Corrsin, Experiments in nearly homogenous turbulent shear flow with a uniform mean temperature gradient. Part 1, J. Fluid Mech. **104**, 311 (1981).
[19] S. Tavoularis and S. Corrsin, Experiments in nearly homogeneous turbulent shear flow with a uniform mean temperature gradient. Part 2. The fine structure, J. Fluid Mech. **104**, 349 (1981).
[20] Z. Warhaft, The interference of thermal fields from line sources in grid turbulence, J. Fluid Mech. **144**, 363 (1984).
[21] J. Nedić and S. Tavoularis, Measurements of passive scalar diffusion downstream of regular and fractal grids, J. Fluid Mech. **800**, 358 (2016).
[22] M. K. Chung and N. H. Kyong, Measurement of turbulent dispersion behind a fine cylindrical heat source in a weakly sheared flow, J. Fluid Mech. **205**, 171 (1989).
[23] M. S. Uberoi and S. Corrsin, Diffusion of heat from a line source in isotropic turbulence, NACA Technical Note No. 2710 (National Advisory Committee for Aeronautics, Washington, DC, 1952).
[24] J. E. Fackrell and A. G. Robins, Concentration fluctuations and fluxes in plumes from point sources in a turbulent boundary layer, J. Fluid Mech. **117**, 1 (1982).
[25] A. Townsend, The diffusion behind a line source in homogeneous turbulence, Proc. R. Soc. London A **224**, 487 (1954).
[26] L. Mydlarski, L. Danaila, and R. A. Lavertu, Isotropy of the temperature field downstream of a line source in turbulent channel flow, in *Advances in Turbulence XI: Proceedings of the 11th EUROMECH European Turbulence Conference*, Springer Proceedings in Physics Vol. 117 (Springer, New York, 2007), pp. 500–502.
[27] G. I. Taylor, Diffusion by continuous movements, Proc. London Math. Soc. **20**, 196 (1921).
[28] G. K. Batchelor, Diffusion in a field of homogeneous turbulence. I. Eulerian analysis, Aust. J. Chem. **2**, 437 (1949).
[29] S. Tavoularis and J. Nedić, Taylorian diffusion in mildly inhomogeneous turbulence, Int. J. Heat Fluid Flow **67**, 116 (2017).
[30] J. Nedić and S. Tavoularis, A case study of multi-structure turbulence: Uniformly sheared flow distorted by a grid, Int. J. Heat Fluid Flow **72**, 233 (2018).
[31] J. D. Li, B. J. McKeon, W. Jiang, J. F. Morrison, and A. J. Smits, The response of hot wires in high Reynolds-number turbulent pipe flow, Meas. Sci. Technol. **15**, 789 (2004).
[32] R. M. Lueptow, K. S. Breuer, and J. H. Haritonidis, Computer-aided calibration of X-probes using a look-up table, Exp. Fluids **6**, 115 (2004).

[33] G. I. Taylor, The spectrum of turbulence, Proc. R. Soc. London A **164**, 476 (1938).
[34] G. Comte-Bellot and S. Corrsin, The use of a contraction to improve the isotropy of grid-generated turbulence, J. Fluid Mech. **25**, 657 (1966).
[35] M. Wilczek, H. Xu, and Y. Narita, A note on Taylor's hypothesis under large-scale flow variation, Nonlinear Processes Geophys. **21**, 645 (2014).
[36] Y. Zheng, K. Nagata, and T. Watanabe, Energy dissipation and enstrophy production/destruction at very low Reynolds numbers in the final stage of the transition period of decay in grid turbulence, Phys. Fluids **33**, 035147 (2021).
[37] R. A. Antonia and A. J. Chambers, On the correlation between turbulent velocity and temperature derivatives in the atmospheric surface layer, Boundary-Layer Meteorol. **18**, 399 (1980).
[38] J. C. Bennett and S. Corrsin, Small Reynolds number nearly isotropic turbulence in a straight duct and a contraction, Phys. Fluids **21**, 2129 (1978).
[39] R. M. Kerr, Higher-order derivative correlations and the alignment of small-scale structures in isotropic numerical turbulence, J. Fluid Mech. **153**, 31 (1985).
[40] C. W. Van Atta and R. A. Antonia, Reynolds number dependence of skewness and flatness factors of turbulent velocity derivatives, Phys. Fluids **23**, 252 (1980).

Chapter 5

Grid-generated velocity fields at very small Reynolds numbers

This chapter contains the following article, which was published in Physical Review Fluids on 27 February 2024:

Duong, D., & Tavoularis, S. (2024), "Grid-generated velocity fields at very small Reynolds numbers", Phys. Rev. Fluids 9(2), 024607.

Experiments were conducted in a specially designed wind tunnel, which was capable of generating flows at very low speeds and used velocity calibration and measurement methods that are suitable for low speeds. Measurements identified and characterised an intermediate state between conventional grid turbulence and steady flow. The flow structure in the intermediate range exhibited some peculiarities which depended on the grid geometry and the Reynolds number. The Reynolds stress anisotropy increased drastically in the intermediate state. The power spectra in the intermediate state differed strongly, when normalised by Kolmogorov scales based on the measured dissipation rate, but nearly collapsed in their large wavenumber ranges, when normalised by a dissipation rate that was fitted to a universal normalised spectrum. The flow state could not be characterised accurately by the Reynolds number based on mesh size, but the change of state from the conventional to the intermediate one occurred at $\mathrm{Re}_\lambda \approx 10$ for all grids. The experiments further described the dependence of the skewness and flatness factors of the streamwise velocity derivative, the ratio of production and dissipation of vorticity fluctuations and the dissipation parameter upon Re_λ.

An issue not addressed in the published article is whether the non-fully-turbulent flow regime has common characteristics with a flow that undergoes transition from laminar to turbulent. Unlike a transitional flow that is in the process of becoming fully turbulent (e.g., flow closely behind grids at relatively large Reynolds numbers), the present non-conventional grid-generated fluctuations are not evolving towards conventional turbulence.

In this work, the terms ‘laminar”, “transitional” and “turbulent” flow were avoided when describing the three regimes observed. Nevertheless, with the exception of the “steady flows” in which the grid elements generate no velocity fluctuations, all other regimes originate at the unsteady vortices shed by the these elements. At low Reynolds numbers, the interactions between these vortices and the corresponding instability mechanisms are not strong enough to lead to transition to conventional turbulence, as happens at higher Reynolds numbers.

Grid-generated velocity fields at very small Reynolds numbers

Dana Duong and Stavros Tavoularis*
Department of Mechanical Engineering, University of Ottawa, Ottawa, Ontario, Canada K1N 6N5

(Received 6 November 2023; accepted 2 February 2024; published 27 February 2024)

Statistical moments and power spectra of velocity fluctuations and their temporal derivative were measured behind four square-mesh grids at very small bulk Reynolds numbers. Three distinct states of such flows were identified: (1) in cases with insufficiently small Reynolds number, the flow was characterized as conventional grid turbulence, in which the turbulent kinetic energy was scaled with the mean velocity; (2) when the Reynolds number dropped below a threshold, which was specific for each grid, the flow was characterized as approximately steady; and (3) for Reynolds numbers that were between the two previous bounds ("intermediate state"), the flow structure exhibited peculiarities, the details of which depended on the grid geometry and the Reynolds number. The Reynolds stress anisotropy increased drastically in the intermediate state. Moreover, power spectra in the intermediate state differed strongly, when normalized by Kolmogorov scales based on the measured dissipation rate, but nearly collapsed in their large wave number ranges, when normalized by a dissipation rate that was fitted to a universal normalized spectrum. The flow state could not be characterized accurately by the Reynolds number based on mesh size, but the change of state from the conventional to the intermediate one occurred at $\mathrm{Re}_\lambda \approx 10$ for all grids. Finally, measurements quantified the dependence of the skewness and flatness factors of the streamwise velocity derivative, the ratio of production, and dissipation of vorticity fluctuations and the dissipation parameter upon Re_λ.

DOI: 10.1103/PhysRevFluids.9.024607

I. INTRODUCTION

Grid-generated turbulence has long served as a popular paradigm of turbulent flows and an essential benchmark for the validation of theories and models. Moreover, grids, screens, and other uniform flow obstructions are used routinely for improving the quality of streams in wind tunnels and other fluid mechanical apparatus. Although it is generally desirable for turbulence-generating grids to operate at relatively large Reynolds numbers (based on the mean speed and the grid spacing), there are occasions (for example, fine-mesh screens stretched across the plenum of a wind tunnel) on which the Reynolds number is very small.

The term "grid" has been used to describe a variety of devices with periodically arranged flow obstructions, but in the present work we will consider, as representative designs, perforated plates and woven screens with square openings, characterized by a mesh size M and a solidity σ. When the flow mean speed $\overline{U}_1$ is sufficiently large, a grid will generate turbulence in the production region, which extends up to a relatively short dimensionless streamwise distance x_1/M from the grid, or, equivalently, a relatively short dimensionless convection time $t\overline{U}_1/M$ ($t = x_1/\overline{U}_1$). In this region, turbulence is produced by the strong shear that is present in the interacting wakes of the solid elements and the jets issuing from the open spaces between elements. The kinetic energy per

*stavros.tavoularis@uottawa.ca

unit mass k of turbulence reaches a maximum, typically at $x_1/M \approx 4$ [1], beyond which it decays monotonically, until it is dissipated entirely to heat.

All turbulent flows have velocity fluctuations, which are random processes, but not all flows with velocity fluctuations, even random ones, are considered to be turbulent, unless they satisfy additional physical and statistical conditions. A broadly accepted condition is that the flow contains a vortex-stretching mechanism that is capable of generating random vorticity fluctuations ω [2]. Another important feature of turbulent flows is that they consist of motions with relatively wide ranges of length, time, and amplitude scales. Two most prominent postulates of turbulence theory are that sufficiently strong turbulence has (1) a universal fine structure (first Kolmogorov hypothesis) and (2) a power spectrum that includes an inertial subrange, in which it is proportional to a power of the wave number with an exponent $-5/3$ (second Kolmogorov hypothesis).

The strength of a turbulent flow is commonly measured by the value of the turbulence Reynolds number $\mathrm{Re}_\lambda = u_1'\lambda/\nu$, where u_1' is the standard deviation of the streamwise velocity fluctuations, λ is the Taylor microscale, and ν is the kinematic viscosity of the fluid. Much interest in the field has focused on studies of grid turbulence having Re_λ values that were as large as possible. Turbulence produced by passive grids has, in most cases, $\mathrm{Re}_\lambda < 100$, whereas active grids have raised the upper limit of this parameter to nearly 1000. It has also been understood that, when Re_λ is smaller than a value of the order of 10, the distinct characteristics that qualify a flow as turbulent tend to become bland and, presumably, for even smaller Re_λ, turbulence would likely become undetectable. The local value of Re_λ and the state of the flow depend on the grid geometry, the distance from the grid, and a macroscopic, or bulk, Reynolds number. Two length scales may be used to define the latter: the frontal height d of the grid bars and the grid mesh size M. The former is more relevant in the close proximity of the grid, whereas the latter is relevant sufficiently downstream, where the wakes of adjacent bars interact with each other. Accordingly, one may define two macroscopic Reynolds numbers, $\mathrm{Re}_d = \overline{U}_1 d/\nu$ and $\mathrm{Re}_M = \overline{U}_1 M/\nu$. Following an analogy to the well-examined flows past circular cylinders, one may anticipate that the stream through a grid of a certain design would remain steady, when Re_M is lower than a critical value Re_{Ms} or, equivalently, when Re_d is lower than a critical value Re_{ds}. One may also expect that, as Re_M and Re_d are increased, the flow would become unsteady, possibly undergoing through one or multiple unsteady laminar states and eventually transitioning to turbulence. Whereas steady and fully turbulent flows can be identified unambiguously, intermediate cases should not necessarily be classified as transitional.

There has been no previous examination of the effect of Re_d and the only previous study that appears to be concerned about the value of Re_{Ms} is the one by Tavoularis *et al.* [3], who stated that the flow ceased to be turbulent as Re_M approached 400. One may also anticipate the possible existence of thresholds Re_{Mt} and Re_{dt}, above which the flow may be characterized as "conventional grid turbulence," in the sense that it has a strong self-similar energy transfer mechanism. Certain characteristics of flows in the intermediate range $\mathrm{Re}_{Ms} < \mathrm{Re}_M < \mathrm{Re}_{Mt}$ have been addressed in the literature, although the results have not been presented as functions of Re_M, but rather Re_λ. It must be pointed out, however, that, although Re_M is fixed for a given grid and mean speed, Re_λ decreases along the flow, and so it may attain a small value in both strongly decayed turbulence, as well as in a flow which was never fully turbulent; we will revisit this issue in the next section. There is plenty of experimental evidence that, even at moderate Re_λ, grid-generated turbulence displays a strong vortex-stretching mechanism and some inertial subrange. Moreover, a numerical study [4] concluded that an inertial subrange is not visible for $\mathrm{Re}_\lambda \lesssim 20$, although the power spectrum may still satisfy an approximate universality in the dissipative subrange. The main focus of the present study is precisely the characteristics of flows behind grids in this intermediate range. Collecting measurements with very small Re_M is quite challenging, because general-purpose wind tunnels cannot operate well at very low speeds and grids with a very small M tend to suffer from local nonuniformity of the mesh. Another challenge is the measurement of velocity fluctuations at low mean speeds. Hot wires are suitable for this purpose, but commonly used hot-wire calibration standards, including Pitot tubes and pressure drop across a contraction, are insensitive at air speeds

that are lower than about 4 m/s. Therefore, in order to examine low-Re grid turbulence, one must give particular consideration to the choice of apparatus and experimental methodology.

The objective of this study is to investigate experimentally the characteristics of flows past grids in the ranges $120 \lesssim \mathrm{Re}_M \lesssim 5000$ and $20 \lesssim \mathrm{Re}_d \lesssim 670$. A unique feature of our experiments is that the wind tunnel and the hot-wire calibration procedure are particularly suitable for such measurements. Statistical moments and power spectra of velocity fluctuations and their temporal derivatives are measured and analyzed to determine whether each flow under examination may be qualified as conventional grid turbulence or not. In the following, we will first present some theoretical background on low Reynolds number grid turbulence. Then we will describe briefly the wind tunnel, the grids, and the measurement procedures. Next we will present the experimental results and their analysis, and finally we will summarize the main conclusions.

II. BACKGROUND ON LOW-RE GRID TURBULENCE

The decay of grid-generated turbulence is commonly described by empirically fitted power functions of the type

$$k = a\left(\frac{x_1 - x_{10}}{M}\right)^{-n}, \tag{1}$$

where a is a constant that depends on the grid geometry, n is the decay exponent, and x_{10} is an effective origin. The values of a, n, and x_{10} depend on the grid design and are specific to each of several successive ranges of x_1/M. Previous authors [5–15] have distinguished the following ranges of decay:

(1) A "near-field range," typically for $4 \lesssim x_1/M \lesssim 20$, where $1.5 \lesssim n \lesssim 1.8$

(2) The "initial period of decay," typically for $20 \lesssim x_1/M \lesssim 150$, where $1.2 \lesssim n \lesssim 1.3$

(3) An intermediate range, typically for $150 \lesssim x_1/M \lesssim 500$, where n is somewhat larger than in the previous range and

(4) The "final period of decay," for $500 \lesssim x_1/M$, where $n \approx 2.5$.

The simplified balance equation for the standard deviation ω' of vorticity fluctuations in isotropic turbulence is [16]

$$\frac{d\omega'^2}{dt} = -\frac{7}{3\sqrt{5}}\omega'^3 S - \frac{14}{3\sqrt{5}}\omega'^3 \frac{G}{\mathrm{Re}_\lambda}, \tag{2}$$

where the skewness of the velocity derivative is

$$S \equiv \frac{\overline{(\partial u_1/\partial x_1)^3}}{\left[\overline{(\partial u_1/\partial x_1)^2}\right]^{3/2}} \tag{3}$$

and

$$G \equiv u_1'^2 \frac{\overline{(\partial^2 u_1/\partial x_1^2)^2}}{\left[\overline{(\partial u_1/\partial x_1)^2}\right]^2}. \tag{4}$$

Equation (2) shows that the rate of change of vorticity fluctuations is equal to the balance between production by vortex stretching, which has a coefficient equal to $-S$, and dissipation by viscous actions, which has a coefficient equal to G/Re_λ. A negative S, which is evidence of deviation from normality, is an essential feature of turbulent flows and has been associated with the presence of ramplike patterns in the velocity signals. Non-normality of the velocity derivative has been also associated with the "spotty" nature of the fine structure of the flow, referred to as the internal intermittency of turbulence. An indicator of the internal intermittency strength is the flatness factor

of the velocity derivative

$$F \equiv \frac{\overline{(\partial u_1/\partial x_1)^4}}{\left[\overline{(\partial u_1/\partial x_1)^2}\right]^2}. \tag{5}$$

Although Eq. (2) is strictly applicable to isotropic turbulence, one may extend the concepts of vorticity fluctuation production and dissipation to wider classes of turbulent flows, the fine structure of which may be approximated as locally isotropic, under the understanding that this approximation tends to be more accurate as Re_λ increases. The dependence of S and F on Re_λ has been examined analytically and experimentally by several authors both for grid turbulence and for other turbulent flows [3,15,17–20]. Tavoularis *et al.* [3] were the first to show that S plateaus near -0.5 at moderate Re_λ ($\mathrm{Re}_\lambda \gtrsim 10$), but, as Re_λ decreases below about 10, S decreases in magnitude towards 0. Moreover, it has been amply demonstrated that F increases with increasing Re_λ and tends towards the normal value 3, as Re_λ decreases to very small values. The dependence of G upon Re_λ in grid turbulence has been investigated in the range $5 \leqslant \mathrm{Re}_\lambda \leqslant 1000$ [15,16,21–27]. In decaying turbulence that follows a power law, G may be related to S as [28]

$$\frac{G}{\mathrm{Re}_\lambda} \equiv \frac{15}{7\mathrm{Re}_\lambda}\left(\frac{n-1}{n}\right) + \frac{S}{2}. \tag{6}$$

This expression shows that, as $\mathrm{Re}_\lambda \to 0$, $(G/\mathrm{Re}_\lambda)/(-S) \to \infty$, which implies that, as turbulent activity weakens, vorticity dissipation tends to dominate its production [16,21,23,24,26]. The same expression implies that, as Re_λ increases, production and dissipation tend to equalize [15,21,23].

An important postulate, which has been exploited widely for the development of turbulence models, is that, at sufficiently large Re_λ, the dissipation parameter

$$C_\varepsilon = \frac{\varepsilon L}{k^{3/2}}, \tag{7}$$

where ε is the turbulent kinetic energy dissipation rate per unit mass and L is the integral length scale, is constant [1,9,29–34]. The nonconstancy of C_ε in various flows with moderate Re_λ has been documented by several authors [9,33,35–37]. A numerical simulation [38] has suggested that, as $\mathrm{Re}_\lambda \to 0$, $C_\varepsilon \to \infty$, and recent experiments [15] seem to support such a trend, at least down to $\mathrm{Re}_\lambda \approx 5$. Additional work is required to resolve this issue.

In closing this section, it seems worthwhile to reemphasize that Re_λ can be decreased by either decreasing Re_M or by increasing x/M, and so Re_λ may approach zero while the flow structure evolves along different paths. Although the available literature on low Reynolds number grid turbulence includes cases concerned with the final period of decay far from the grid [17,39] and cases with diminishing Re_M at intermediate and long distances from the grid [3,15], it does not explicitly distinguish among the paths followed by the flow structure during its evolution. A conclusive comparison of the flow structure of initially strong turbulence in its final period of decay and the structure of turbulence that was very weak during its generation requires new, craftily designed, experiments and simulations.

III. APPARATUS AND MEASUREMENT PROCEDURES

The experiments were performed in an open-circuit wind tunnel, shown in Fig. 1. This facility has a bypass branch close to the axial blower and far upstream of the test section, through which part of the flow was bled, thus reducing the flow rate through the rest section. The bypass flow rate was controlled by the rotation of a hinged flap via a linear actuator. This wind tunnel is capable of producing pulsatile flows, but, for the present needs, the flap was fixed at a desired position so that the flow in the test section was stationary and the mean speed was in a range of values that included ones that were much lower than those produced stably in the absence of a bypass branch. The flow speed in the test section was controlled by two settings, the blower motor speed

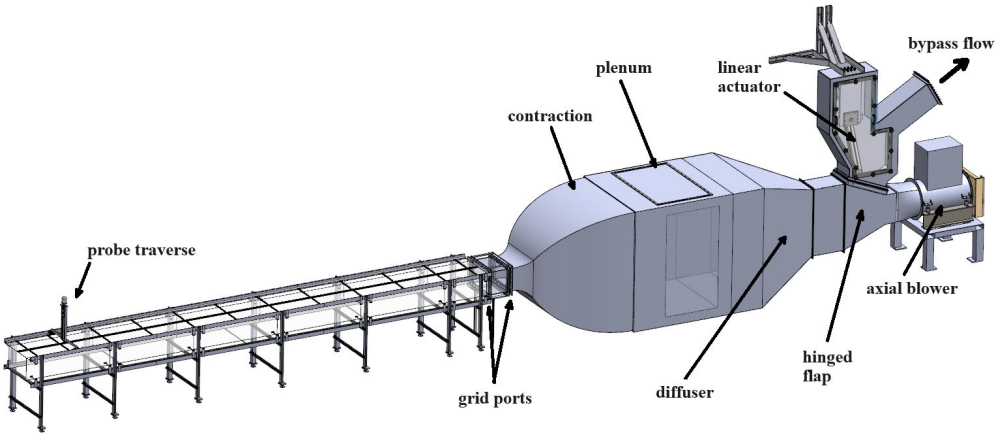

FIG. 1. Sketch of the wind tunnel facility.

and the flap position, both of which could be adjusted precisely. A flow speed map corresponding to different combinations of these two settings was constructed by calibration against velocity measurements at the entrance of the test section with a laser Doppler velocimetry. The uncertainty of these measurements was estimated to be 0.3%.

The test section has a height $h = 305$ mm, a nominal width of $1.5h$, and a length of $22.5h$. Beyond an initial length of $1h$, the test section side walls were adjusted to be slightly diverging, to compensate for the mean pressure field for boundary layer growth.

Among the many grids with various designs and mesh sizes that were available for use in this facility, we selected four, which are listed in Table I, as suitable for the present work, and sufficiently diverse to reveal possible effects of manufacturing process, mesh size, and solidity. Grid M19 was a square-mesh perforated plate, machined from a steel sheet with a thickness of 1.6 mm, whereas grids M13, M3A, and M3B were square-mesh screens, made of woven steel wire. The symbol d in the table denotes the width of solid bars for M19 and the wire diameter for M13, M3A, and M3B. The solidity of the first three grids is comparable to values used widely in the literature, whereas the solidity of M3B is near the upper limit of the range that is considered to produce stable streams [40,41].

All measurements were taken for mean flow velocities ranging from $\overline{U}_1 = 0.4$ to 4 m/s at a streamwise location $x_1/M = 30$. The ranges of obtained Re_M for the four screens are presented in Table I. For comparison, the same table lists the corresponding conditions in four experiments by previous authors. We may note that a quantitative comparison of flows produced by grids with

TABLE I. Summary of experimental conditions for the present four grids and for the grids that produced the lowest Reynolds numbers in four experiments by previous authors.

Grid name	M19	M13	M3A	M3B	BT [39]	BC [17]	TBC [3]	ZNW [15]
Grid type	Perforated	Woven	Woven	Woven	Woven	Woven	Woven	Woven
M [mm]	19.1	12.7	3.2	3.2	1.59	4.23	1.27	5.0
d [mm]	2.55	2.00	0.50	0.76	0.30	0.82	0.25	0.82
σ	0.25	0.29	0.29	0.42	0.34	0.35	0.35	0.39
$\overline{U}_1$ [m/s]	0.4–4.0	0.4–4.0	0.6–4.0	0.6–4.0	6.15	6.1	5.6	2.0
Re_M	520–5000	360–3300	120–820	120–830	650	1720	475	680
Re_d	70–670	53–530	20–130	29–200	120	330	92	146
Symbol	Circle	Cross	Triangle	Square				

different solidity and/or different design (e.g., a perforated plate with bars having a rectangular cross section and a woven screen made of initially cylindrical wires) would be more accurate, if it were based on values of "effective" mesh size and/or bar frontal height, which account for differences in the actual flow velocity approaching each bar and the pattern of the flow separating from the bar. We did not attempt to apply corrections to Re_M and Re_d, as the few relevant results available in the literature are not likely to be accurate at low Reynolds numbers.

Measurements of the streamwise and vertical velocity components were made with a custom-made hot-wire probe. The velocity sensors, arranged in a cross-wire configuration, were made of tungsten and had a diameter of 2.5 μm, a sensing length of 0.85 mm, and a separation distance of 0.5 mm. The length-to-diameter ratio was 340, which is sufficiently large for end conduction effects to be negligible [42]. The hot-wire signals were low-pass filtered with analog filters, having cutoff frequencies of 3.8 kHz, digitized at a rate of 8 kHz and recorded over 60 s for each test. The cross-wire probe was calibrated *in situ* using a velocity-pitch-map calibration method [43] against the test section flow velocity map, which, as mentioned previously, was calibrated against readings of a laser Doppler velocimeter.

The streamwise integral length scale was calculated as $L = \overline{U}_1 T$, where the integral time scale T was determined by integrating the autocorrelation function of the streamwise velocity to its first zero. The velocity derivative variances $\overline{(\partial u_1/\partial t)^2}$ and $\overline{(\partial^2 u_1/\partial t^2)^2}$ were calculated by extrapolating corresponding finite differences to a zero time lag. Using Taylor's frozen flow approximation, the Taylor microscale was calculated as $\lambda = \overline{U}_1[u_1'^2/\overline{(\partial u_1/\partial t)^2}]^{1/2}$ and the turbulence Reynolds number was calculated as $\mathrm{Re}_\lambda = u_1'\lambda/\nu$. The turbulent kinetic energy dissipation rate was then estimated using the isotropic expression $\varepsilon = 15\nu u_1'^2/\lambda^2$, from which we calculated the Kolmogorov microscale as $\eta = (\nu^3/\varepsilon)^{1/4}$ and the dissipation parameter as $C_\varepsilon = (L\varepsilon)/u_1'^3$ [note that the latter definition gives values that are different from those given by Eq. (7)]. It is recognized that the present estimate of ε would likely increasingly deviate from the actual dissipation rate as Re_M decreases and the energy cascade mechanism weakens and eventually disappears. Results obtained using isotropic relationships among the various properties are treated as reference values and also serve for comparison with results in the literature.

The reported measurements are corrected for the effects of wind tunnel background fluctuations and electronic noise. For example, it was considered that the instantaneous measured streamwise velocity fluctuation behind the grid is $u_{1m} = u_1 + u_{1b} + u_{1n}$, where u_1 is the velocity fluctuation generated by the grid, u_{1b} is the background velocity fluctuation (which exists in the wind tunnel irrespectively of the presence of the grid), and u_{1n} is electronic noise (converted to an equivalent velocity fluctuation). Similarly, the instantaneous measured streamwise velocity fluctuation in the absence of any grid was considered to be $u_{1bm} = u_{1b} + u_{1n}$. Under the assumption that u_1, u_{1b} and u_{1n} were statistically uncorrelated to each other, we derived expressions for the relationships between the various statistical properties of u_{1m} and u_1, and applied appropriate corrections, when found to be significant. The statistical properties of u_{1n} were measured with the hot-wires operating in the wind tunnel without any flow and those of u_{1bm} were measured at each given mean speed without any grid inserted. Expressions from which the corrected statistical properties of grid-generated fluctuations were calculated and typical correction levels will be presented in the dissertation of the first author [44]. In general, for the majority of results, corrections were negligible or relatively small. The electronic noise level, expressed as the variance of equivalent velocity fluctuations $u_{1n}'^2$ and measured with the probe in the wind tunnel, but without any flow, was 3.6×10^{-7} m^2/s^2. The largest correction of the measured velocity variance was about 40% and corresponded to the case with grid M3A at a speed $\overline{U}_1 \approx 0.6$ m/s, for which it was found that $u_{1bm}'^2 = 7.2 \times 10^{-6}$ m^2/s^2 and $u_{1m}'^2 = 1.9 \times 10^{-5}$ m^2/s^2. The normalized velocity variance for this case, which in the following will be characterized as "steady," was $u_1'^2/\overline{U}_1^2 = 3 \times 10^{-5}$, which is much smaller than the maximum value 7.5×10^{-4} of this ratio for this grid, obtained at higher speeds. The corrected integral length scale was essentially equal to the measured value within the conventional grid-turbulence range, but the correction factor exceeded 10 as the steady state was approached.

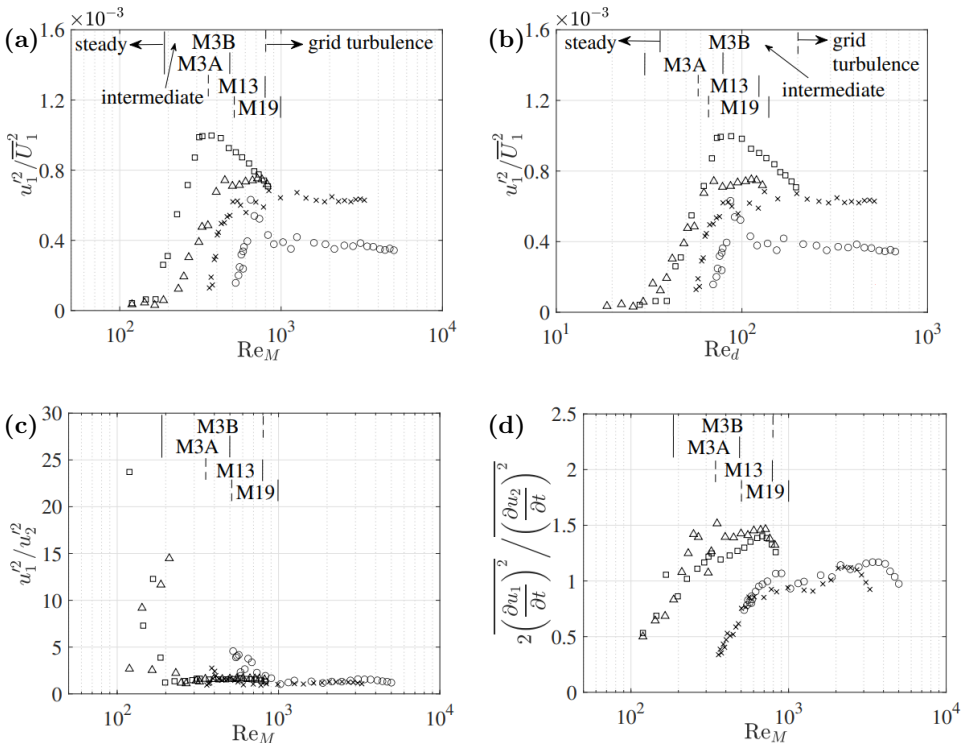

FIG. 2. Strength of velocity fluctuations behind the M19 (○), M13 (×), M3A (△), and M3B (□) grid vs (a) the mesh Reynolds number and (b) the bar Reynolds number; the boundaries between states for each grid are indicated by solid vertical lines, whereas dashed lines indicate that the corresponding boundaries appeared to be outside the available experimental range; indicators of (c) large-scale and (d) fine structure anisotropies.

The most significant corrections, which could have affected the reported results, if they had not been applied, were made for the flatness factor of the velocity derivative at the lowest wind tunnel speeds. When corrected, these flatness factors were in the vicinity of the Gaussian value 3, whereas the uncorrected values could be as low as 1, as a result of the very small flatness of the background fluctuations.

IV. DETERMINATION OF FLOW STATE

To determine the state of the flow behind each grid for each value of Re_M, we compared the value of the relative strength $u_1'^2/\overline{U}_1^2$ of velocity fluctuations at $x_1/M = 30$ with the level corresponding to conventional grid turbulence for the same grid. Measurements of this property are presented in Fig. 2(a). The range of Re_M that were achievable in this facility extended to large enough values for $u_1'^2/\overline{U}_1^2$ in the flows behind M19, M13, and M3A to reach plateaus, within which conventional grid turbulence is deemed to occur. The lack of such a plateau for M3B, may be attributed to an insufficiently large attainable Re_M. The conventional level, as well as the profile of data for each grid, appear to depend on the geometry of the grid. Based on Fig. 2(a), we characterized the threshold of conventional grid turbulence as the lower boundary Re_{Mt} of each plateau. The corresponding values are listed in Table II. A notable observation in this figure is that $u_1'^2/\overline{U}_1^2$ overshoots its conventional value and peaks at an intermediate Re_M, below which it decreases sharply with decreasing Re_M. The location and amplitude of the peak also seem to depend on the grid geometry.

TABLE II. Reynolds numbers characterizing each flow.

Grid name	M19	M13	M3A	M3B
Re_{Mt}	1000	800	500	>800
Re_{Ms}	<520	<360	180	180
Re_{dt}	138	126	78	>200
Re_{ds}	<70	<57	30	35
Re_{λ}	0.6–21	0.7–23	0.4–13	0.7–12

Of central interest in this work is the determination of Re_{Ms}, below which the grid does not generate any turbulence, or rather any velocity fluctuations at all. This was possible for the two smaller grids (M3A and M3B), for which we could achieve very small values of Re_M, including cases ($120 \leqslant \mathrm{Re}_M \lesssim 180$) with essentially negligible fluctuations, for which the flow may be characterized as approximately steady. Therefore, our results for these two grids show that $\mathrm{Re}_{Ms} \approx 180$.

As mentioned previously, the state of the flow in the immediate vicinity of the grid would possibly depend on the bar Reynolds number Re_d. Figure 2(b) shows the dependence of the turbulence strength parameter $u_1'^2/\overline{U}_1^2$ on Re_d for the four grids. For the two smaller grids, for which steady flow was achieved, the threshold Re_{ds} was, respectively, about 30 and 35, thus lower than 47, which is a nominal upper limit for the wakes of circular cylinders to be steady. This observation is also consistent with the finding that, for the two larger grids, the flow remained unsteady even for the lowest achievable Re_d, which was, respectively, 70 and 57; it is noted that, in the range $47 \lesssim \mathrm{Re}_d \lesssim 100$, the wake of a circular cylinder is unsteady and, following a shear layer instability mechanism, develops laminar vortices. In the intermediate ranges $\mathrm{Re}_{Ms} < \mathrm{Re}_M < \mathrm{Re}_{Mt}$ and $\mathrm{Re}_{ds} < \mathrm{Re}_d < \mathrm{Re}_{dt}$, we may postulate that the flow is unsteady and possibly transitional, albeit lacking some characteristics of conventional grid turbulence.

We have produced plots of several other properties using d as a length scale and compared them with corresponding plots using M instead. As we did not find any significant additional information that can be extracted from the former, we will proceed using Re_M as the independent variable.

The dependence of $u_1'^2/u_2'^2$ and $2\overline{(\partial u_1/\partial t)^2}/\overline{(\partial u_2/\partial t)^2}$ upon Re_M is shown, respectively, in Fig. 2(c) and Fig. 2(d). These ratios are, respectively, indicators of the anisotropy of the energy containing eddies (Reynolds stresses) and the fine structure (dissipation rate). Within the upper range of Re_M values that were achievable for each grid, the values of both ratios were nearly constant and somewhat larger than the isotropic value of 1, in conformity with a multitude of previous grid turbulence measurements [45,46]. As Re_M decreased in the intermediate ranges, these two ratios showed opposite trends; the former tended to increase, whereas the latter tended to decrease. Although we do not have sufficient information to explain these trends, we may speculate as follows. The relative weakening of transverse velocity fluctuations may be attributed to a diminishing "flapping" of the bar wakes. The relative strengthening of the transverse velocity derivative variance may indicate that vortices shed from the bars became increasingly nearly parallel to the transverse plane, so large values of $|\partial u_2/\partial t|$ are encountered across the axis of each vortex.

In summary, the dependence of the strength of velocity fluctuations and the anisotropy indicator upon Re_{Mi} is qualitatively consistent for the four grids and allows us to identify or infer three distinct states: a conventional grid turbulence state, an essentially steady flow state, and an intermediate state for each grid. In general, the boundaries of the Re_M ranges for these states depended on the grid geometry, particularly distinguishing woven screens from perforated plates.

An essential feature of turbulence is the mechanism of energy cascade, which entails an isotropy and universality of the fine structure. The approximate universality of power spectra in the high-wave-number range (namely, in the inertial and dissipative subranges) has been demonstrated by many authors. This has been evidenced by the approximate collapse of corresponding spectral

measurements when normalized by Kolmogorov scales in the form [47]

$$E_{11}(\kappa_1)/(\varepsilon\nu^5)^{1/4} = C(\kappa_1\eta)^{-5/3} f_\eta(\kappa_1\eta), \tag{8}$$

where C is a universal constant and $f_\eta(\kappa_1\eta)$ is a universal function. An issue that arises when comparing measurements in different setups is the diversity of the expressions used to estimate ε. Following many previous experiments, we estimated ε from measurements of λ, under the assumption of isotropy. Djenidi and Antonia [48], however, proposed that the dissipation rate for a given turbulent flow should have a value ε^* that fits, in the large wave number range, the universal equation

$$E_{11}(\kappa_1)/(\varepsilon^*\nu^5)^{1/4} = C^*(\kappa_1\eta^*)^{-5/3} f^*_{\eta^*}(\kappa_1\eta^*), \tag{9}$$

where $\eta^* = (\nu^3/\varepsilon^*)^{1/4}$ and C^*, $f^*_{\eta^*}(\kappa_1\eta^*)$ were specified empirically. In conventional grid turbulence, the ratio $\varepsilon^*/\varepsilon$ should be nearly 1, and so one may use the deviation of the value of this ratio from 1 to identify the weakening of turbulent interactions, particularly the deterioration of the energy cascade process, as Re_M diminishes. It is interesting to note that, with a suitable value of ε^*, the dissipative range of normalized spectra may, at least partially, be fitted by Eq. (9), even in the absence of an inertial subrange [4]. In the following, we shall refer to $E_{11}(\kappa_1)/(\varepsilon^*\nu^5)^{1/4}$ as the *adjusted normalized spectrum* to distinguish this property from the Kolmogrorov-normalised spectrum $E_{11}(\kappa_1)/(\varepsilon\nu^5)^{1/4}$.

Figures 3(a), 3(c), 3(e), and 3(g) present the adjusted normalized streamwise velocity spectra behind the four grids for different Re_M. We found that Eq. (9) fit our experimental results fairly well at the high Re_M. As shown in Figs. 3(b), 3(d), 3(f), 3(h), when $\mathrm{Re}_M > \mathrm{Re}_{Mt}$, the ratio $\varepsilon^*/\varepsilon$ was not significantly different from 1, in accordance with conventional grid turbulence literature. Our results also confirm previous observations that the range of the spectra that fit the universal expression diminishes, as the inertial subrange becomes narrower with decreasing Reynolds number. When $\mathrm{Re}_M < \mathrm{Re}_{Mt}$, however, $\varepsilon^*/\varepsilon$ changes behavior. For the two larger grids, this ratio decreases monotonically, up to by one order of magnitude, within the intermediate state, and one may speculate that this trend would likely continue if the measurements were extended to the boundary of the steady state. In the intermediate states of the two smaller grids, $\varepsilon^*/\varepsilon$ first increased somewhat with decreasing Re_M and then started to decrease, first mildly and then, within the steady state, abruptly to extremely small values, which indicate that the dissipation rate was negligible in the steady state.

V. EFFECT OF REYNOLDS NUMBER ON TURBULENCE PROPERTIES

Having identified an intermediate state of grid-generated velocity fluctuations, we now investigate the dependence of some important turbulence properties upon the Reynolds number with focus in this intermediate range. Figure 4 shows the dependence of the streamwise integral scale, the Taylor microscale, their ratio, and the turbulence Reynolds number upon the mesh Reynolds number for the four grids. Although the results for each grid are distinct from those of any other, each of these properties displays a clear qualitative pattern that applies to all cases.

In the conventional grid turbulence range, the integral length scale is somewhat smaller than M and roughly proportional to $\mathrm{Re}_M^{-0.4}$, in agreement with the literature. The same scale, however, generally increases with decreasing Re_M in the intermediate range, reaching values that are up to more than two orders of magnitude larger than M, as the flow approaches the steady state. It is noted that L is computed by integrating the autocorrelation function, corrected statistically for background fluctuations under the assumption that these are uncorrelated with velocity fluctuations generated by the grid. The accuracy of this assumption for very low Re_M cannot be tested with the available information.

The Taylor microscale also follows an inverse power function of Re_M with an exponent in the range -0.4 to -0.5 in the conventional grid turbulence range, but, in contrast with L, it drops with decreasing Re_M in the intermediate range. This indicates a diminishing strength of grid-generated

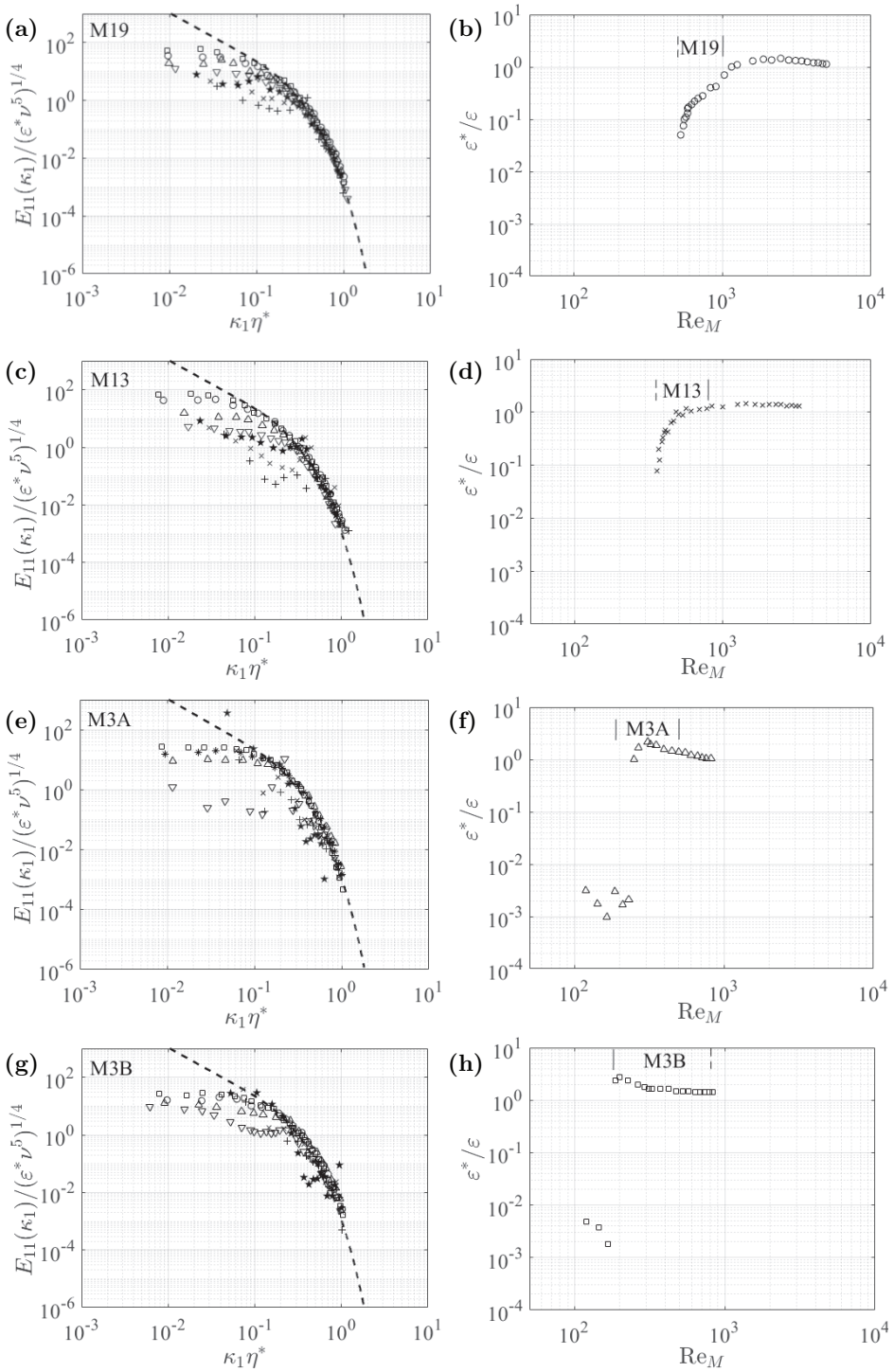

FIG. 3. Adjusted, normalized one-dimensional streamwise velocity spectra for the four grids [(a), (c), (e), (g)] and the corresponding values of the ratio $\varepsilon^*/\varepsilon$ [(b), (d), (f), (h)] for different values of Re_M; $---$: universal spectrum [48]; Re_M values: (a) 520 (+), 540 (×), 620 (★), 900 (▽), 1600 (△), 2470 (◯), 5000 (□); (c) 360 (+), 380 (×), 390 (★), 440 (▽), 700 (△), 2270 (◯), 3300 (□); (e) 120 (+), 160 (×), 210 (★), 270 (▽), 400 (△), 600 (◯), 820 (□); (g) 120 (+), 140 (×), 170 (★), 230 (▽), 290 (△), 420 (◯), 830 (□).

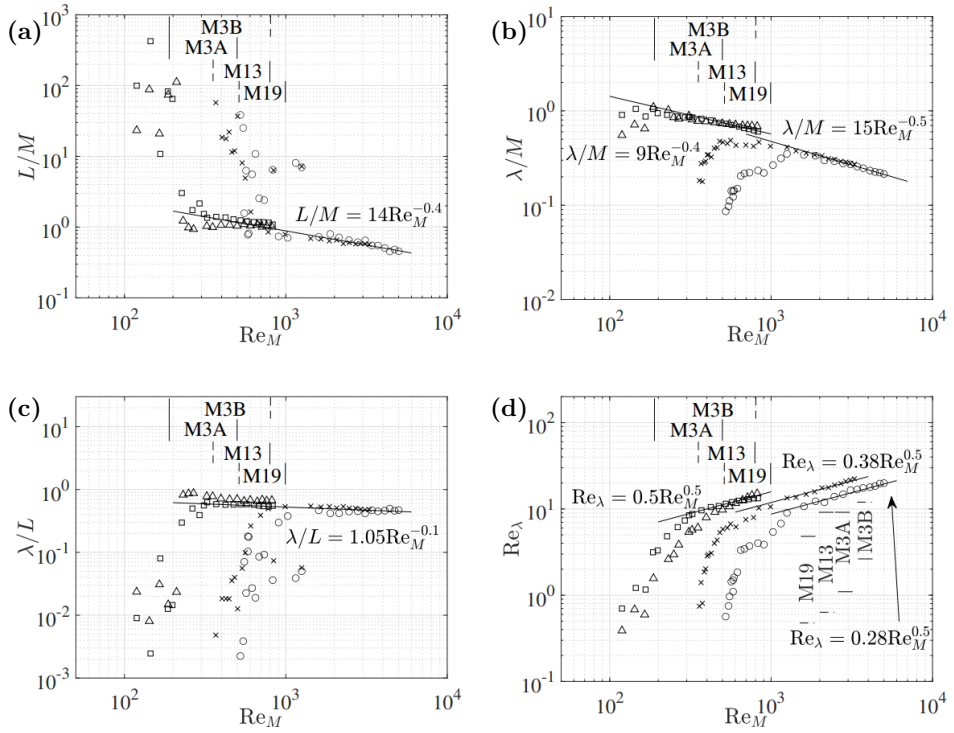

FIG. 4. Plots of (a) the normalized streamwise integral timescale, (b) the normalized Taylor microscale, (c) the ratio of the Taylor microscale and the integral timescale, and (d) the turbulence Reynolds number vs the mesh Reynolds number Re_M; the symbols have been defined in Table I and in the caption of Fig. 2.

fine structure, by comparison to the strength of energy containing motions. The same inference can be based, even more clearly, on Fig. 4(c), which shows that the ratio λ/L decreases rapidly with decreasing Re_M in the intermediate range. For a fixed Re_M (where there is overlap), λ/M and λ/L increase with decreasing mesh size. Overall, these results show that the fine structure of these flows cannot be characterized solely by the value of Re_M.

As shown in Table II, the upper ends of the ranges of Re_λ for all grids overlapped with values in some previous studies, but the lower ends extended to significantly lower values than previously reported. Like L/M and λ/M, the dependence of Re_λ on Re_M was distinct for each grid, but all results followed the same qualitative pattern. In the upper ranges of Re_M, Re_λ could be fitted by a power law of the type $\mathrm{Re}_M^{0.5}$, but, below some value of Re_M in the intermediate turbulence state (roughly equal to Re_{Mt}), Re_λ dropped rapidly as Re_M decreased. An important observation in this figure is that, for all grids, the boundary between the two distinct ranges occurred near $\mathrm{Re}_\lambda \approx 10$, which demonstrates that the flow structure is much better characterized by the value of Re_λ than by the value of Re_M. This is hardly a surprise, because Re_λ is a measure of the strength of the turbulence, whereas Re_M is a measure of the strength of the bulk flow. Consequently, in the following, additional statistical indicators of the state of turbulence will be plotted vs Re_λ.

Our plots of the skewness S and flatness F of the streamwise velocity derivative, shown respectively in Figs. 5(a) and 5(b), are consistent with the results of Tavoularis *et al.* [3], which they complement with a significantly larger database and extend to significantly lower Re_λ. Moreover, the present data allow the fitting of rough power laws to S and F, which may be of use in future theoretical and computational studies.

Figure 5(c) shows that, in agreement with previous literature [15,23,24,26], the ratio $S/(2G/\mathrm{Re}_\lambda)$ is near unit in conventional grid turbulence, and quickly approaches zero as Re_λ decreases. This

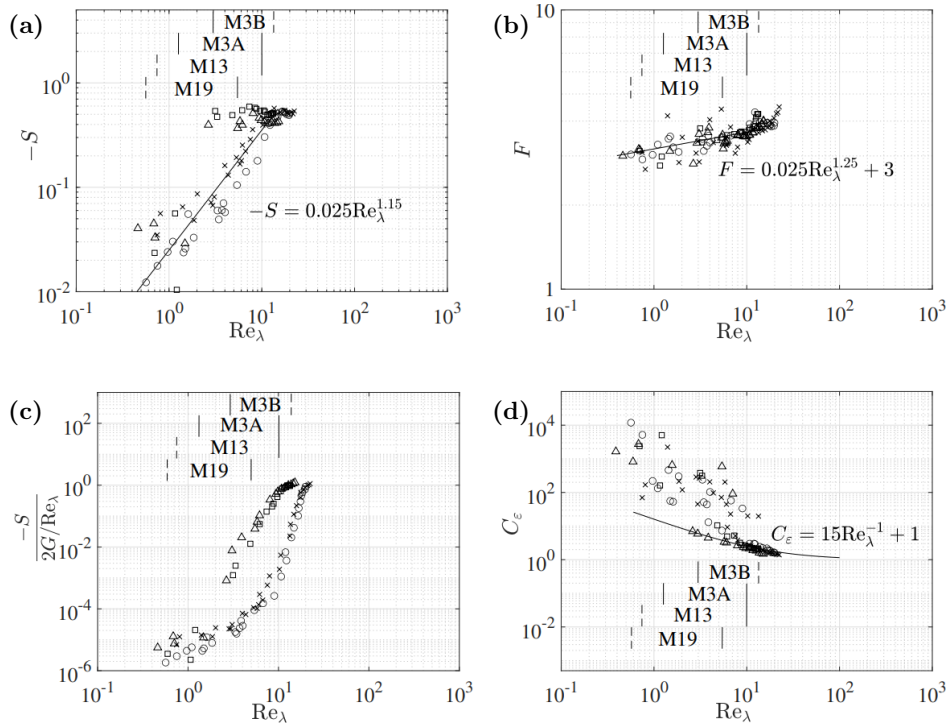

FIG. 5. Plots of (a) the streamwise velocity derivative skewness factor, (b) the streamwise velocity derivative flatness factor, (c) the ratio $(-S)/(2G/\mathrm{Re}_\lambda)$, and (d) C_ε vs Re_λ for the four grids; the symbols have been defined in Table I and in the caption of Fig. 2.

shows that, indeed, as turbulent activity weakens, vorticity dissipation tends to dominate its production.

Finally, Fig. 5(d) presents the dissipation parameter C_ε against Re_λ. In the presently attainable conventional grid turbulence region, which extends only up to $\mathrm{Re}_\lambda \approx 20$, the results may be fitted by the expression $C_\varepsilon = 15\mathrm{Re}_\lambda^{-1} + 1$ to indicate the expected tendency of C_ε to settle at a constant value near unit at larger Re_λ [30]. However, once the flow is in the intermediate region, C_ε increases with decreasing Re_λ significantly faster than this expression indicates, reaching values that are as large as 10 000.

VI. CONCLUDING REMARKS

In the present article, we report investigations of the state and statistical properties of flows behind spatially periodic obstructions ("grids") at Reynolds numbers that are sufficiently small for the velocity fields not to follow conventional grid-turbulence trends. This topic has received little attention in the literature, although devices operating under such conditions are used in laboratories and commercial flow systems. Measurements were taken behind four square-mesh grids with varying designs, mesh sizes, and solidities. Conditions in the present flows overlap with those in grid turbulence literature, which are used as a reference. However, the present study expands significantly the available database for smaller Reynolds numbers and examines cases in which the grid-produced velocity fluctuations are negligible. We have documented and quantified the weakening of turbulent behavior as the Reynolds number diminishes and identified trends and patterns that to the best of our knowledge have not been reported previously. It is hoped that the present findings will motivate future experimental and computational studies of flows past periodic obstructions at small

Reynolds numbers, which may further elucidate their sensitivity to various effects and their general complexity.

ACKNOWLEDGMENT

Funding for this research was provided by the Natural Sciences and Engineering Research Council of Canada, Grant No. RGPIN-2017-03835.

[1] J. C. Vassilicos, Dissipation in turbulent flows, Annu. Rev. Fluid Mech. **47**, 95 (2015).
[2] G. I. Taylor, The spectrum of turbulence, Proc. R. Soc. London A **164**, 476 (1938).
[3] S. Tavoularis, J. C. Bennett, and S. Corrsin, Velocity-derivative skewness in small Reynolds number, nearly isotropic turbulence, J. Fluid Mech. **88**, 63 (1978).
[4] L. Djenidi, S. F. Tardu, R. A. Antonia, and L. Danaila, Breakdown of Kolmogorov's first similarity hypothesis in grid turbulence, J. Turbul. **15**, 596 (2014).
[5] Jayesh and Z. Warhaft, Probability distribution, conditional dissipation, and transport of passive temperature fluctuations in grid-generated turbulence, Phys. Fluids A **4**, 2292 (1992).
[6] D. Hurst and J. C. Vassilicos, Scalings and decay of fractal-generated turbulence, Phys. Fluids **19**, 035103 (2007).
[7] P.-Å. Krogstad and P. A. Davidson, Near-field investigation of turbulence produced by multi-scale grids, Phys. Fluids **24**, 035103 (2012).
[8] J. C. Isaza, R. Salazar, and Z. Warhaft, On grid-generated turbulence in the near-and far field regions, J. Fluid Mech. **753**, 402 (2014).
[9] J. Nedić and S. Tavoularis, Measurements of passive scalar diffusion downstream of regular and fractal grids, J. Fluid Mech. **800**, 358 (2016).
[10] R. E. Seoud and J. C. Vassilicos, Dissipation and decay of fractal-generated turbulence, Phys. Fluids **19**, 105108 (2007).
[11] P.-Å. Krogstad and P. A. Davidson, Freely decaying, homogeneous turbulence generated by multi-scale grids, J. Fluid Mech. **680**, 417 (2011).
[12] Ö. Ertunç, N. Özyilmaz, H. Lienhart, F. Durst, and K. Beronov, Homogeneity of turbulence generated by static-grid structures, J. Fluid Mech. **654**, 473 (2010).
[13] P. C. Valente and J. C. Vassilicos, The decay of turbulence generated by a class of multiscale grids, J. Fluid Mech. **687**, 300 (2011).
[14] P. C. Valente and J. C. Vassilicos, The non-equilibrium region of grid-generated decaying turbulence, J. Fluid Mech. **744**, 5 (2014).
[15] Y. Zheng, K. Nagata, and T. Watanabe, Energy dissipation and enstrophy production/destruction at very low Reynolds numbers in the final stage of the transition period of decay in grid turbulence, Phys. Fluids **33**, 035147 (2021).
[16] G. K. Batchelor and A. A. Townsend, Decay of vorticity in isotropic turbulence, Proc. R. Soc. London A **190**, 534 (1947).
[17] J. C. Bennett and S. Corrsin, Small Reynolds number nearly isotropic turbulence in a straight duct and a contraction, Phys. Fluids **21**, 2129 (1978).
[18] C. W. Van Atta and R. A. Antonia, Reynolds number dependence of skewness and flatness factors of turbulent velocity derivatives, Phys. Fluids **23**, 252 (1980).
[19] R. A. Antonia and A. J. Chambers, On the correlation between turbulent velocity and temperature derivatives in the atmospheric surface layer, Boundary-Layer Meteorol. **18**, 399 (1980).
[20] R. M. Kerr, Higher-order derivative correlations and the alignment of small-scale structures in isotropic numerical turbulence, J. Fluid Mech. **153**, 31 (1985).
[21] S. K. Lee, L. Djenidi, R. A. Antonia, and L. Danaila, On the destruction coefficients for slightly heated decaying grid turbulence, Int. J. Heat Fluid Flow **43**, 129 (2013).

[22] H. S. Kang, S. Chester, and C. Meneveau, Decaying turbulence in an active-grid-generated flow and comparisons with large-eddy simulation, J. Fluid Mech. **480**, 129 (2003).
[23] T. Zhou, R. A. Antonia, L. Danaila, and F. Anselmet, Transport equations for the mean energy and temperature dissipation rates in grid turbulence, Exp. Fluids **28**, 143 (2000).
[24] T. Zhou, R. A. Antonia, and L. Chua, Performance of a probe for measuring turbulent energy and temperature dissipation rates, Exp. Fluids **33**, 334 (2002).
[25] L. Djenidi and R. A. Antonia, Transport equation for the mean turbulent energy dissipation rate in low-grid turbulence, J. Fluid Mech. **747**, 288 (2014).
[26] M. J. Huang and A. Leonard, Power-law decay of homogeneous turbulence at low Reynolds numbers, Phys. Fluids **6**, 3765 (1994).
[27] J. V. Larssen and W. J. Devenport, On the generation of large-scale homogeneous turbulence, Exp. Fluids **50**, 1207 (2011).
[28] W. K. George, The decay of homogeneous isotropic turbulence, Phys. Fluids A **4**, 1492 (1992).
[29] G. K. Batchelor, *The Theory of Homogeneous Turbulence* (Cambridge University Press, Cambridge, 1953).
[30] K. R. Sreenivasan, On the scaling of the turbulence energy dissipation rate, Phys. Fluids **27**, 1048 (1984).
[31] K. R. Sreenivasan, S. M. Deshpande, A. Prabhu, and P. R. Viswanath, The energy dissipation in turbulent shear flows, in *Symposium on Developments in Fluid Dynamics and Aerospace Engineering* (Interline, Bangalore, 1995), pp. 159–190.
[32] J. Nedić and S. Tavoularis, Energy dissipation scaling in uniformly sheared turbulence, Phys. Rev. E **93**, 033115 (2016).
[33] J. Nedić, S. Tavoularis, and I. Marusic, Dissipation scaling in constant-pressure turbulent boundary layers, Phys. Rev. Fluids **2**, 032601(R) (2017).
[34] O. Cadot, Y. Couder, A. Daerr, S. Douady, and A. Tsinober, Energy injection in closed turbulent flows: Stirring through boundary layers versus inertial stirring, Phys. Rev. E **56**, 427 (1997).
[35] J. Nedić and S. Tavoularis, A case study of multi-structure turbulence: Uniformly sheared flow distorted by a grid, Int. J. Heat Fluid Flow **72**, 233 (2018).
[36] C. Livingston and S. Tavoularis, Multi-structure turbulence in a boundary layer with a uniformly sheared free stream, in *Proceedings of the 12th International Symposium on Turbulence and Shear Flow Phenomena (TSFP12) Osaka, Japan, July 19–22, 2022* (2022), pp. 1–6.
[37] S. Tavoularis and J. Nedić, Taylorian diffusion in mildly inhomogeneous turbulence, Int. J. Heat Fluid Flow **67**, 116 (2017).
[38] W. D. McComb, A. Berera, M. Salewski, and S. Yoffe, Taylor's (1935) dissipation surrogate reinterpreted, Phys. Fluids **22**, 061704 (2010).
[39] G. K. Batchelor and A. A. Townsend, Decay of turbulence in the final period, Proc. R. Soc. London A **194**, 527 (1948).
[40] S. Corrsin, Turbulence: Experimental methods, in *Handbuch der Physik—Encyclopedia of Physics, Vol. 8 (2)*, edited by S. Fluegge and C. Truesdell (Springer, Berlin, 1963), pp. 524–590.
[41] S. Tavoularis and J. Nedić, *Measurement in Fluid Mechanics*, 2nd ed. (Cambridge University Press, Cambridge, 2024).
[42] J. D. Li, B. J. McKeon, W. Jiang, J. F. Morrison, and A. J. Smits, The response of hot wires in high Reynolds-number turbulent pipe flow, Meas. Sci. Technol. **15**, 789 (2004).
[43] R. M. Lueptow, K. S. Breuer, and J. H. Haritonidis, Computed aided calibration for X-probes applied to wall-bounded turbulent shear flows, Exp. Fluids **6**, 115 (2004).
[44] D. Duong, Studies of turbulence in low Reynolds number and pulsatile grid turbulence (unpublished).
[45] A. Tsinober, E. Kit, and T. Dracos, Experimental investigation of the field of velocity gradients in turbulent flows, J. Fluid Mech. **242**, 169 (1992).
[46] R. Gomes-Fernandes, B. Ganapathisubramani, and J. C. Vassilicos, Particle image velocimetry study of fractal-generated turbulence, J. Fluid Mech. **711**, 306 (2012).
[47] S. B. Pope, *Turbulent Flows* (Cambridge University Press, Cambridge, 2000).
[48] L. Djenidi and R. A. Antonia, A spectral chart method for estimating the mean turbulent kinetic energy dissipation rate, Exp. Fluids **53**, 1005 (2012).

Chapter 6

The effect of mean flow pulsation on grid turbulence and passive scalar diffusion

6.1 Introduction

Grid-generated turbulence has long served as a primary paradigm of turbulent flows and an essential benchmark for the validation of turbulence theories and models. Although the vast majority of grid turbulence studies have examined stationary flows, a few others have documented some characteristics of non-stationary ones. These include theoretical, computational and experimental studies. In one of the earliest analyses of periodic turbulence, Lohse (2000) examined periodically "kicked" turbulence. He determined that, for a fixed amplitude, the Reynolds number varied with the frequency at smaller frequencies, but had an initial rise and then approached a saturation value at larger frequencies (Lohse, 2000). This study also proposed an experiment to confirm the theoretical results by using two counter-rotating disks; this proposed experiment was realised by Cadot *et al.* (2003). Since then, several studies of periodic turbulence have been performed. These include experimental ones, in which periodic flows were produced by oscillating grids (Cheng & Law, 2001; McCorquodale & Munro, 2017, 2018*a*), grid turbulence in pulsatile flows generated by a wave generator (Raushan *et al.*, 2019, 2021), and pulsatile flows generated by active grids (Azzam & Lavoie, 2019, 2023). In addition, computational studies, in which isotropic turbulence was subject to periodic or pulsatile modulation have been performed (Yang *et al.*, 2019; Bos *et al.*, 2007; Kuczaj *et al.*, 2006, 2008). In another early theoretical study, von der Heydt *et al.* (2003*a*) proposed that the amplitude of the response of the turbulence decreased proportionally to the inverse of the frequency at high modulation frequencies, while for lower modulation frequencies the response of the turbulence followed the modulation with a nearly constant amplitude. Additionally, these authors found that at

some frequencies the amplitude of the response was either significantly diminished or enhanced. Numerical simulations confirmed these observations (von der Heydt *et al.*, 2003*b*). Direct numerical simulations (DNS) of the same problem (Kuczaj *et al.*, 2006) arrived at similar conclusions. In another DNS, the authors examined the effects of the amplitude and the type of forcing and found that the maximal response was more pronounced for larger amplitudes (Kuczaj *et al.*, 2008). Two types of forcing were examined in this work, the first was the sinusoidal forcing used in previous studies and the second was a square-wave forcing, the same as in the periodically "kicked" turbulence by Lohse (2000). It was found that the maximal response of the turbulence occurred at a time scale of the order of the eddy turnover time. This work was followed up by experimental work by Cekli *et al.* (2010), using an active grid to periodically modulate a turbulent wind tunnel flow; they found a resonant enhancement of the turbulent kinetic energy dissipation rate at a modulation frequency f equal to the large-eddy turnover rate T_e. Specifically, at $fT_e \approx 1.5$, the dissipation rate was approximately 1.5 times the dissipation rate at $fT_e = 1$, regardless of the turbulence intensity. Another recent follow-up study (Fang & Bos, 2023) examined the effects on the dissipation rate from large-scale forcing and from turbulence with reversed initial conditions. Their results showed that the predicted perturbation spectrum followed the $k^{-7/3}$ law, confirming their previous theoretical predictions and other DNS results (Horiuti & Tamaki, 2013).

Recent experimental work has examined pulsatile flows generated by a wave generator upstream of a passive grid in a closed-loop water tunnel (Raushan *et al.*, 2019, 2021). The wave generator was operated in three modes (0 Hz (off), 0.75 Hz, and 1.5 Hz) and three different grids were used. Results of the mean velocities, instantaneous velocity time-series, large-scale anisotropies, kinetic energy dissipation rates, length scales and dissipation parameters were documented. These were further compared to cases without a grid present. Curiously, they found that the the largest streamwise variance was generated by the smallest grid in the stationary case, the largest grid in the medium frequency case, and the middle grid in their high frequency case. Generally, larger grids would produce larger velocity variances, but this difference in observations is likely associated with two factors. The first is the difference in solidities of their grids; the smallest grid had the largest solidity, and the largest grid had the smallest solidity. The second is that, in the cases where pulsatile

flow is generated, there appear to be cycle-to-cycle variations in the data. In the latter work, comparisons of the turbulence parameters between the different frequency test cases were made, but comparisons to the stationary case were not possible because measurements without the grid were taken at only one streamwise location.

In this work, we investigate experimentally the characteristics of pulsatile flows and turbulent diffusion downstream of passive grids. At first glance, one would expect that the introduction of sufficiently strong pulsatility to a flow would augment both the turbulent kinetic energy and the turbulent diffusion. Nevertheless, the literature does not provide conclusive evidence for the validity or not of this inference. A previous numerical investigation of pulsatile grid turbulence (Yang *et al.*, 2019) concluded that, when the amplitude of the modulation was sufficiently large and the modulation frequency was sufficiently small, the transfer rate of the kinetic energy through the energy cascade was increased, while the mixing rate was diminished. In particular, an experimental study of a boundary layer undergoing external free-stream oscillations (Brereton *et al.*, 1990) concluded that free-stream pulsatility resulted in minor differences from the corresponding stationary flow, even at frequencies for which bursting phenomena occurred, provided that the modulation frequency was small enough for the turbulence to respond (von der Heydt *et al.*, 2003*a*,*b*; Kuczaj *et al.*, 2006); the literature shows that, for sufficiently large modulation frequencies, the turbulence does not respond.

6.2 Experimental conditions

The experiments were performed in an open-circuit wind tunnel, presented in Fig. 3.3. This facility is equipped with a bypass branch (see Fig. 3.4) downstream of the axial blower and far upstream of the test section, through which part of the flow is bled, reducing the flow rate through the rest section. The bypass flow rate is controlled by the rotation of a hinged flap *via* a linear actuator. The motion of the linear actuator is controlled by setting the maximum acceleration, deceleration and velocity of motion. The flow speed in the test section is controlled by two settings, the blower motor speed and the flap position, both of which can be adjusted precisely. A flow speed map corresponding to different combinations of these two settings was constructed by calibration against velocity measurements at the entrance of the test section with a laser Doppler velocimeter. The uncertainty of these

measurements was estimated to be 0.3%.

The test section has a height $h = 305$ mm, a nominal width of $1.5h$ and a length of $22.5h$. Beyond an initial length of $1h$, the test section side walls were adjusted to be slightly diverging, to compensate the mean pressure field for boundary layer growth.

For a grid to be chosen, it was desirable to have a relatively large mesh size to produce turbulence at a fairly large Re_λ at the chosen low mean speed, but not so large for wall effects to distort the large scale structure of grid turbulence in the range of measurements. Among the many grids with various designs and mesh sizes that were available for use in this facility, two grids were found to be suitable for the present work. Previous work showed that relatively small mesh-size grids ($M < 3.2$mm) would produce flows with quasi-steady, intermediate and fully grid turbulent flows (Duong & Tavoularis, 2024) for mean speeds $\overline{U_1} < 1.2$ m/s. To guarantee fully turbulent grid turbulence, two grids of larger mesh size, the M19 and M51 grids, were chosen, as well as maintaining the lowest speed of the pulsatile flow above 2 m/s. The M19 grid is a square-mesh perforated plate with a mesh size of $M = 19.1$ mm, a thickness of 1.6 mm, a bar width of $d = 2.4$ mm and a solidity of $\sigma = 0.25$. The M51 grid is also a square-mesh perforated plate with a mesh size of $M = 50.8$ mm, thickness of 1.6 mm, bar width of $d = 6.8$ mm and a solidity of $\sigma = 0.25$. An electrically heated ribbon, made of Nichrome alloy and having a thickness of 0.13 mm and a width of 1.59 mm, was inserted at a location that was 304.8 mm ($= 0.50M$) downstream of the grid, to serve as the source of a passive scalar (*i.e.*, temperature rise) for diffusion measurements. The heating power was the same for all reported tests. The M51 grid was chosen for the main tests. For this grid, partial transverse profiles of the velocity statistics and mean temperatures were taken in stationary and pulsatile flows with the heating source in place at nine streamwise locations ($x_1/M = 7.5, 10, 20, 30, 40, 50, 60, 70$ and 80). The range of transverse profiles at each x_1/M was limited to a value that was sufficiently large to capture the width of the heated plume. Within this range, measurements were taken at six transverse ($-x_2/h$) locations, except at $x_1/M = 7.5$, where five transverse locations were measured. These numbers of data points were deemed to describe the temperature profile within the plume with sufficient resolution for the present purposes. Additionally, turbulence statistics in stationary and pulsatile flows without the heating source were measured at eight centerline locations of $x_1/M = 10, 20, 30, 40, 50, 60, 70$ and 80. Similar to

the M51 grid, velocity and turbulence statistics measurements for the M19 grid in stationary and pulsatile flow without the heating source were taken at eight centreline locations ($x_1/M = 10, 20, 30, 40, 50, 60, 70$ and 80) to provide a means of evaluating the effects of pulsation in a flow with weaker turbulence. The upstream amplitude of modulation was set at $a = 0.2$ or 20% of the time-averaged streamwise velocity; the phase-averaged velocity during the cycle would be in the approximate range from 2.3 to 3.5 m/s. This value was deemed to be large enough for pulsation effects, if any, to be measurable, but sufficiently small to allow the flap mechanism to operate at a relatively high frequency. The frequency of pulsation was desired to be as high as possible. Considering the capabilities of the flap driving mechanism, we set this frequency at $f = 0.33$ Hz for all tests. Measurements were taken following a warm-up time of 15 min for flow pulsation and ribbon heating to ensure that the flow had reached equilibrium. The experimental conditions are presented in Table 6.1.

Table 6.1: Summary of experimental conditions

Grid name	M51	M51	M19
Grid type	perforated	perforated	perforated
M [mm]	50.8	50.8	19.1
d [mm]	6.8	6.8	2.4
σ	0.25	0.25	0.25
$\overline{U_{1,c0}}$ [m/s]	2.9	2.9	2.9
$a/\overline{U_{1c0}}$	0.2	0.2	0.2
f [Hz]	0.33	0.33	0.33
Line source	yes	no	no
x_1/M	7.5, 10, 20, 30, 40, 50, 60, 70, 80	10, 20, 30, 40 50, 60, 70, 80	10, 20, 30, 40 50, 60, 70, 80
Transverse profiles	yes	no	no

Measurements of the streamwise and transverse (*i.e.*, vertical) velocity components

were made with a custom-made two-wire probe. The velocity sensors, arranged in a cross-wire configuration, were made of tungsten and had a diameter of 2.5 μm, a sensing length of 0.85 mm and a separation distance of 0.5 mm. The length-to-diameter ratio was 340, which is sufficiently large for end conduction effects to be negligible (Li *et al.*, 2004). The mean temperature close to the two-wire probe was measured with a miniature thermistor. The hot-wire signals were corrected for temperature effects. The reported temperature rise in the heated flow was the difference between the locally measured temperature and the temperature upstream of the heated source, measured with the RTD. The hot-wire signals were low-pass filtered with analog filters, having cutoff frequencies of 3.8 kHz, digitised at a rate of 8 kHz and recorded over $\sim$ 2 periods for each test condition. At least 500 cycles were recorded at each location with a gap of approximately 1 s between consecutive records. This amounted to about 60 min of data taking for each location and 360 min for each six-point profile. An increase of the transverse range or the number of measurement locations within the range would have required an excessively lengthy experimental run, which might have entailed possible changes in the experimental conditions and the probe responses. Previous work in the experimental setup found that approximately 400 cycles were required to converge the phase-averaged velocity, fluctuations, and Taylor and Kolmogorov microscales. The cross-wire probe was calibrated *in situ* using a velocity-pitch-map calibration method (Lueptow *et al.*, 1988) against the test section flow velocity map, which was calibrated against readings of a laser Doppler velocimeter. The thermistor was calibrated against readings of the RTD in a heated calibration jet.

The instantaneous velocity for the pulsatile grid turbulence measurement U_i was decomposed using the triple decomposition method Reynolds & Hussain (1972) as $U_i = \overline{U_i} + u_i = \overline{U_i} + \widetilde{u}_i + u_i^* = \langle U_i \rangle + u_i^*$, where $\overline{U_i}$ is the time-averaged velocity, $\widetilde{u}_i$ is the zero-mean coherent (or periodic component) fluctuations, is the u_i^* zero-mean non-coherent (or turbulent) fluctuations, $\langle U_i \rangle$ is the phase-averaged velocity, and the total fluctuations is $u_i = \widetilde{u}_i + u_i^*$. The streamwise integral time scale T_1 was determined by integrating the temporal autocorrelation coefficient of the streamwise velocity fluctuations to its first zero-crossing. The streamwise integral length scale was then estimated as $L_1 = T_1 \langle U_1 \rangle$. The velocity derivative variances $\langle (\partial u_1^* / \partial t)^2 \rangle$ and $\langle (\partial^2 u_1^* / \partial t^2)^2 \rangle$ were calculated by extrapolating

corresponding finite differences to a zero time lag. Using Taylor's frozen flow approximation, the Taylor microscale was calculated as $\lambda = \langle U_1 \rangle (\langle u_1^{*2} \rangle / \langle (\partial u_1^* / \partial t)^2 \rangle)^{1/2}$ and the turbulence Reynolds number was calculated as $\mathrm{Re}_\lambda = \langle u_1^* \rangle \lambda / \nu$. The turbulent kinetic energy dissipation rate was then estimated using the isotropic expression $\varepsilon = 15\nu \langle u_1^{*2} \rangle / \lambda^2$, from which we calculated the Kolmogorov microscale as $\eta = \left(\nu^3/\varepsilon\right)^{1/4}$ and the dissipation parameter as $C_\varepsilon = (L_1 \varepsilon)/\langle u_1^{*2} \rangle^{3/2}$. The skewness of the velocity derivative is $S \equiv \frac{\langle (\partial u_1^* / \partial x_1)^3 \rangle}{\langle (\partial u_1^* / \partial x_1)^2 \rangle^{3/2}}$. To compare to the stationary mean-speed equivalent measurements, the phase-averaged properties are time-averaged over the cycle T_{cycle}.

Stationary mean-speed equivalent grid turbulence measurements were also taken as reference comparisons. The instantaneous velocity for the stationary grid turbulence measurement $U_{i,st}$ was decomposed using Reynolds decomposition as $U_{i,st} = \overline{U_{i,st}} + u_{i,st}$, where $\overline{U_{i,st}}$ is the time-averaged stationary velocity, $u_{i,st}$ is the stationary turbulent fluctuations. The streamwise integral time scale $T_{1,st}$ was determined by integrating the temporal autocorrelation coefficient of the streamwise velocity fluctuations to its first zero-crossing. The streamwise integral length scale was then estimated as $L_{1,st} = T_{1,st} \overline{U_{1,st}}$. The velocity derivative variances $\overline{(\partial u_1 / \partial t)^2}_{st}$ and $\overline{(\partial^2 u_1 / \partial t^2)^2}_{st}$ were calculated by extrapolating corresponding finite differences to a zero time lag. Using Taylor's frozen flow approximation, the Taylor microscale was calculated as $\lambda_{st} = \overline{U_{1,st}} (\overline{u_{1,st}^2} / \overline{(\partial u_1 / \partial t)^2}_{st})^{1/2}$ and the turbulence Reynolds number was calculated as $\mathrm{Re}_{\lambda,st} = u'_{1,st} \lambda_{st} / \nu$. The turbulent kinetic energy dissipation rate was then estimated using the isotropic expression $\varepsilon_{st} = 15\nu u_{1,st}^{'2} / \lambda_{st}^2$, from which we calculated the Kolmogorov microscale as $\eta_{st} = \left(\nu^3/\varepsilon_{st}\right)^{1/4}$ and the dissipation parameter as $C_{\varepsilon,st} = (L_{1,st} \varepsilon_{st})/(u_{1,st}^{'2})^{3/2}$. The skewness of the velocity derivative is $S_{st} \equiv \frac{\overline{(\partial u_1 / \partial x_1)^3}_{st}}{\overline{(\partial u_1 / \partial x_1)^2}_{st}^{3/2}}$.

The reported measurements are corrected for the effects of wind tunnel background fluctuations and electronic noise. For example, it was considered that the instantaneous measured streamwise velocity fluctuation behind the grid for the non-stationary flow is $\langle u_{1m}(t) \rangle = \langle u_1(t) \rangle + \langle u_{1b}(t) \rangle + \langle u_{1n}(t) \rangle$, where $\langle u_1(t) \rangle$ is the velocity fluctuation generated by the grid, $\langle u_{1b}(t) \rangle$ is the background velocity fluctuation (which exists in the wind tunnel irrespectively of the presence of the grid) and $\langle u_{1n}(t) \rangle$ is electronic noise (converted to an equivalent velocity fluctuation). Similarly, the instantaneous measured streamwise velocity fluctuation in the absence of any grid was considered to be $\langle u_{1bm} \rangle = \langle u_{1b} \rangle + \langle u_{1n} \rangle$. Under the assumption that $\langle u_1 \rangle, \langle u_{1b} \rangle$ and $\langle u_{1n} \rangle$ were statistically uncorrelated to each other, we

derived expressions for the relationships between the various statistical properties of $\langle u_{1m} \rangle$ and $\langle u_1 \rangle$, and applied appropriate corrections, when found to be significant. The statistical properties of $\langle u_{1n} \rangle$ were measured with the hot-wires operating in the wind tunnel without any flow and those of $\langle u_{1bm} \rangle$ were measured at each given mean speed without any grid inserted. Expressions from which the corrected statistical properties of grid-generated fluctuations were calculated and typical correction levels are presented in Appendix A.

6.3 Transverse profiles of time-averaged velocity statistics of the heated flow

In this section, we present time-averaged velocity statistics in both stationary and pulsatile grid turbulence in the heated flow. These measurements were taken behind the M51 grid in the heated flow in an earlier part of the research, when we expected we could correct the results for the background fluctuations (see Section 3.3.4). However, it was concluded that it was not possible to perform background fluctuation corrections for the heated flow measurements because, without the grid, the properties of the heated plume would be very different from those with the grid present. Additionally, background fluctuation corrections would not be possible in the boundary layer because, without the grid, the boundary layer thickness and turbulence properties would be very different from those with the grid. Moreover, we also found that measuring the instantaneous temperature with cold wire in these low-speed flows was inaccurate. The only correction that was applied to these velocity measurements was one for local mean temperature changes, measured with the thermistor. Thus, the presented velocity statistics in this section for the heated flow behind the M51 grid are not corrected for the background velocity fluctuations. Error estimates from the unheated flow measurements of the background fluctuation corrections were found to be small ($\sim$ 1%) for the streamwise fluctuations, but increased further downstream (up to 40% at $x_1/M = 80$). The background corrections were found to also be small ($\sim$ 1%) for the anisotropy and turbulent kinetic energy, increasing further downstream (up to 25% at $x_1/M = 80$). For this reason, the results in this section are mainly presented to show the transverse profiles of these properties and should be treated as qualitative. Measurements of additional turbulence properties, such as autocorrelation coefficients and velocity derivative statistics, will not be reported for the heated flow, because it was estimated that background

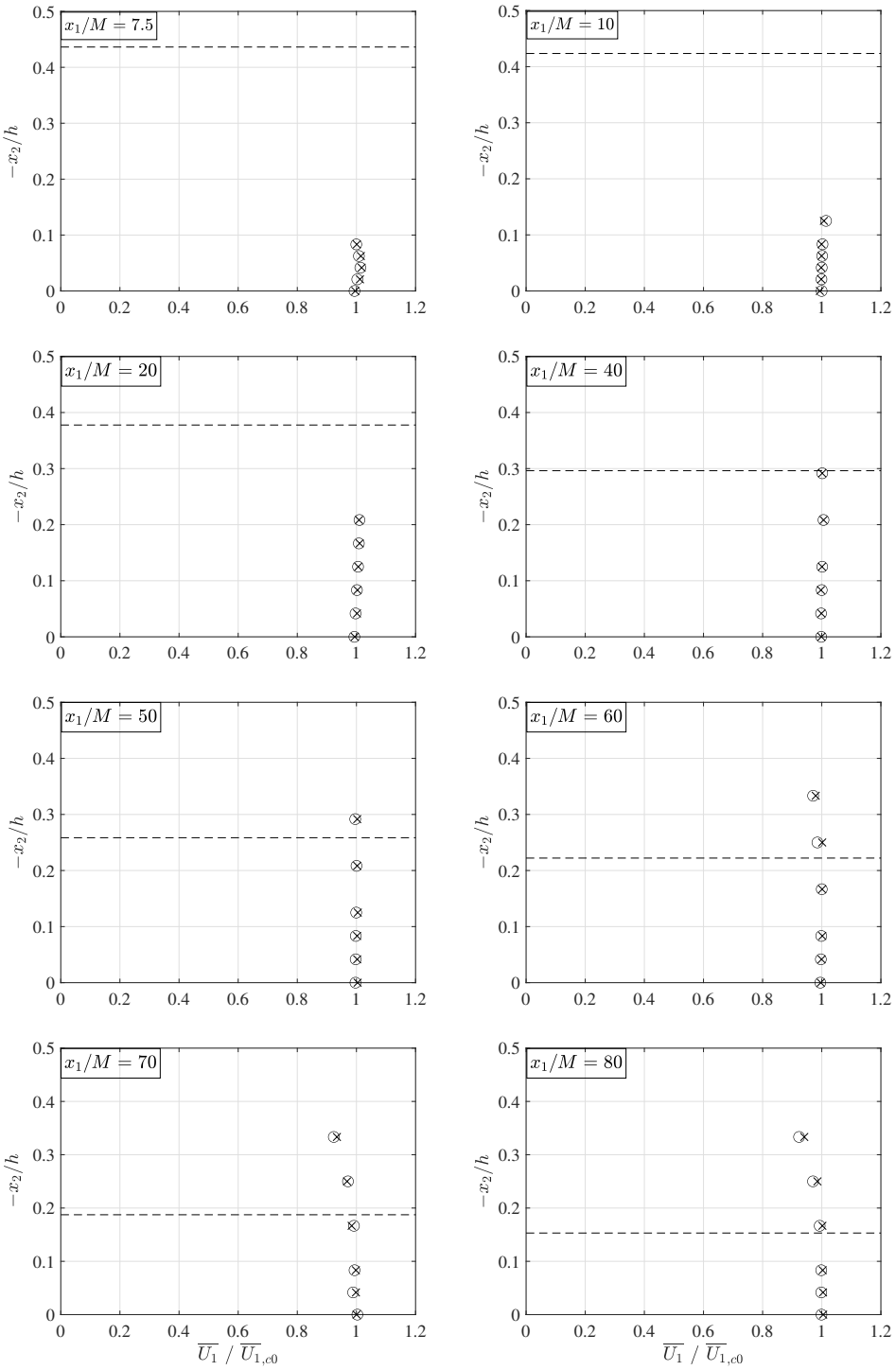

Figure 6.1: Transverse profiles of the normalised time-averaged velocity behind the M51 grid in stationary flow (×) and in pulsatile flow (○); dashed lines mark the estimated edge of the grid turbulence core.

corrections would be very large for some of these properties, especially far downstream of the grid in the pulsatile flow (*e.g.*, $\sim 15 - 150\%$ for L_1 and $\sim 1 - 75\%$ for S and F). The background fluctuation corrections were found to be relatively small for properties of the first derivative of the streamwise velocity (*e.g.* $\sim 0.3 - 11\%$ for λ).

Transverse profiles of the time-averaged velocity, normalised by the reference centreline velocity $\overline{U_{1,c0}} = 2.9$ m/s, are presented in Figure 6.1. At the first streamwise location ($x_1/M = 7.5$), small effects of the grid elements and the ribbon wakes can still be seen in the profile, where a very small momentum deficit is shown at the centreline location. By the next streamwise location at $x_1/M = 10$, the wakes of the grid elements and the ribbon were undetectable. Starting at that location, the transverse profile segments were essentially uniform and remained uniform up to $x_1/M = 50$. At $x_1/M = 60$ the boundary layers along the test section walls began to influence the reported mean profiles and such influence became increasingly stronger downstream. To estimate the boundary layer thickness, we plotted expressions of the type $[(1/2 + x_2/h)]/\delta_e^{1/7}$ in Figure 6.2 and selected the value of δ_e for each x_1/M that appears to produce the best fit to the normalised velocity profile. Because of the small number of measurement points and the narrow range of measurements, the uncertainty of these estimates is relatively large. The results, shown in Figure 6.2, do not show any systematic effect of the flow pulsation. In the same figure, we have also plotted an empirical estimate of the normalised thickness δ/h of a boundary layer that starts as laminar at the end of the contraction ($x_1/h = -1$) and undergoes bypass transition at the grid (Pritchard & Mitchell, 2016). As δ/h is within the measurement uncertainty of δ_e/h, we shall use the former to estimate the boundaries of the core region of the present grid turbulence, which is essentially free of boundary layer effects.

In the following, we will present time-averaged profiles of turbulence statistics. Transverse profiles of the streamwise velocity variance, normalised by the reference centreline velocity $\overline{U_{1,c0}} = 2.9$ m/s, are presented in Figure 6.3. The boundary of the grid-turbulence core is also marked in this figure. First, let us evaluate the effect of pulsation in the core region. At $x_1/M = 7.5$, the level of this property in the stationary flow is noticeably greater than that in the pulsatile flow, but the two levels become approximately equal at $x_1/M = 10$ and, for $x_1/M \geq 20$, the fluctuations in the pulsatile flow are generally larger than those in the stationary flow. The present results also permit us to make some tentative observations

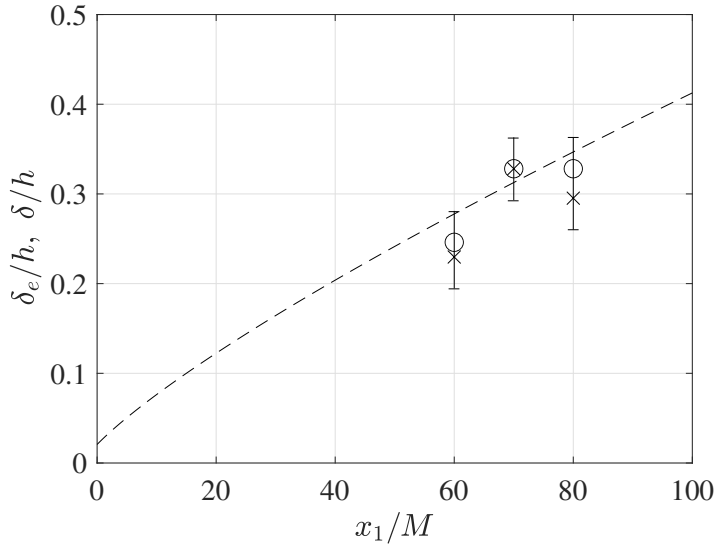

Figure 6.2: Normalised boundary layer thickness δ_e/h) behind the M51 grid in stationary flow ($\times$) and in pulsatile flow ($\circ$), together with an empirical estimate δ/h (dashed line).

for the effect of pulsation in the boundary layer region, in which we have some limited data for $50 \leq x_1/M \leq 80$. The available results also show that the pulsation increases the streamwise turbulence level in the boundary layer.

Transverse profiles of the anisotropy indicator u_1'/u_2' are presented in Figure 6.4. The levels of this indicator are larger than 1, consistently with many previous studies in grid turbulence. In general, we may assess that pulsation results in a small increase of anisotropy, both in the core region and in the boundary layer.

Transverse profiles of the shear stress correlation coefficient are presented in Figure 6.5. The values and profiles are generally consistent with other grid turbulence and boundary layer studies. Only mild differences in the shear stress correlation coefficient can be detected between the results in pulsatile and stationary flows.

Assuming that grid turbulence is axisymmetric in the x_2 and x_3 directions, the turbulent kinetic energy in the core region can be estimated as $k \approx 0.5(\overline{u_1^2}+2\overline{u_2^2})$. The same expression is used in the boundary layer, where it is expected that $\overline{u_2^2} < \overline{u_3^2}$, with the understanding that the shown values may underestimate k by up to about 10%. Transverse profiles of the turbulent kinetic energy normalised by the centreline velocity $\overline{U_{1,c0}}$ at different streamwise locations are presented in Figure 6.6. Like the streamwise fluctuations, the turbulent kinetic

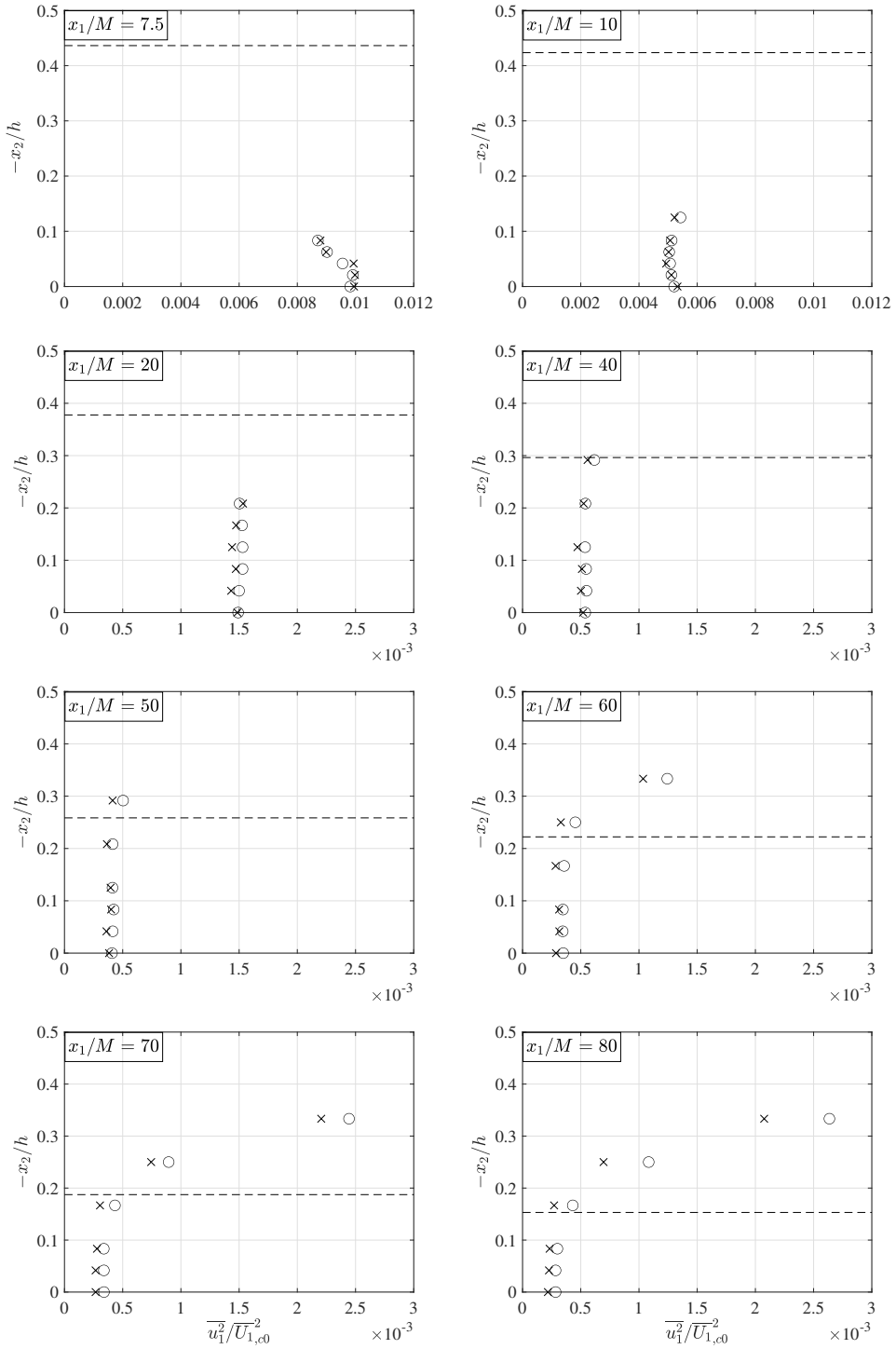

Figure 6.3: Transverse profiles of the normalised time-averaged streamwise velocity fluctuations behind the M51 grid in stationary flow (×) and in pulsatile flow (∘); dashed lines mark the estimated edge of the grid turbulence core.

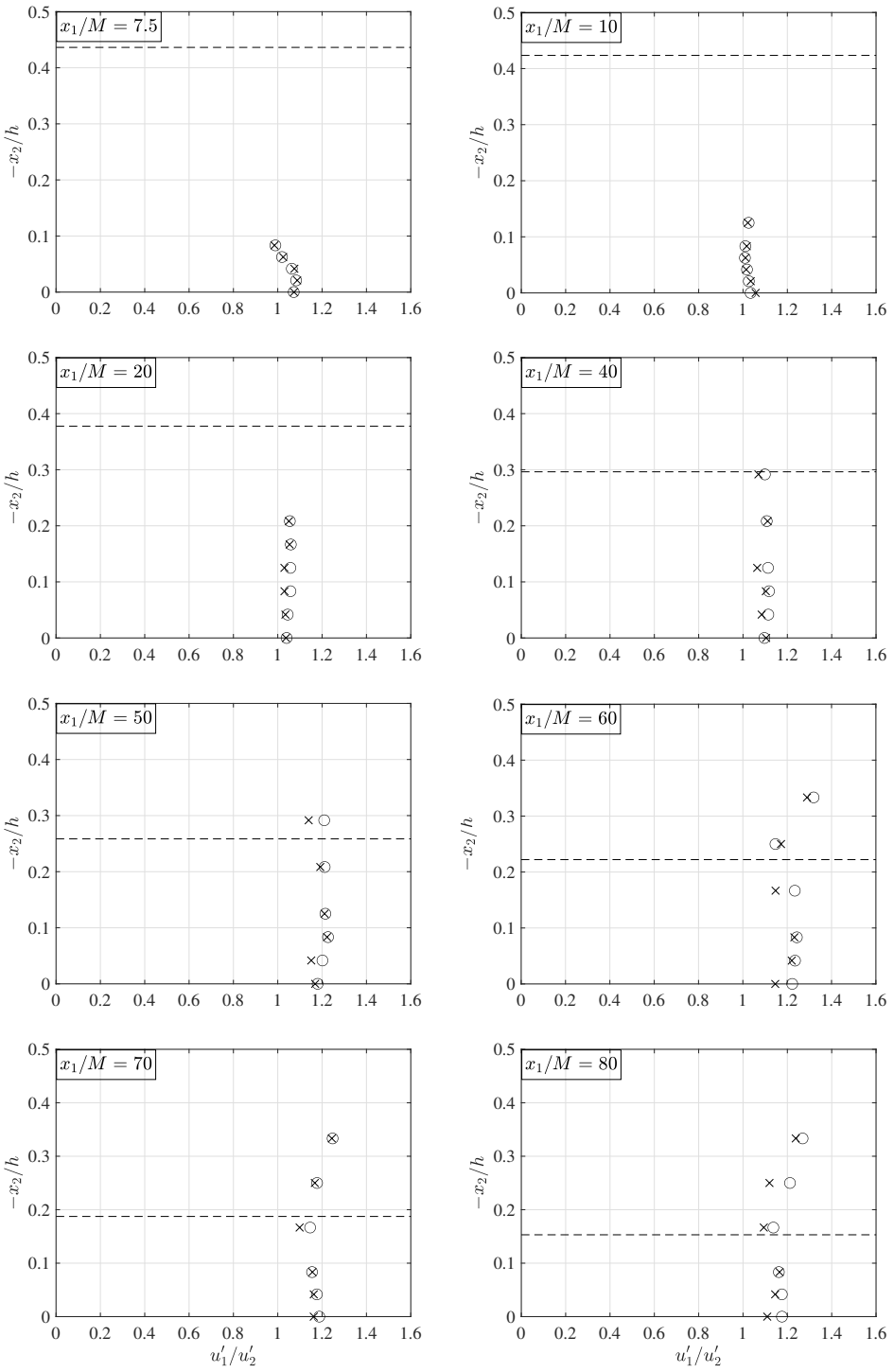

Figure 6.4: Transverse profiles of the time-averaged anisotropy indicator behind the M51 grid in stationary flow (×) and in pulsatile flow (∘); dashed lines mark the estimated edge of the grid turbulence core.

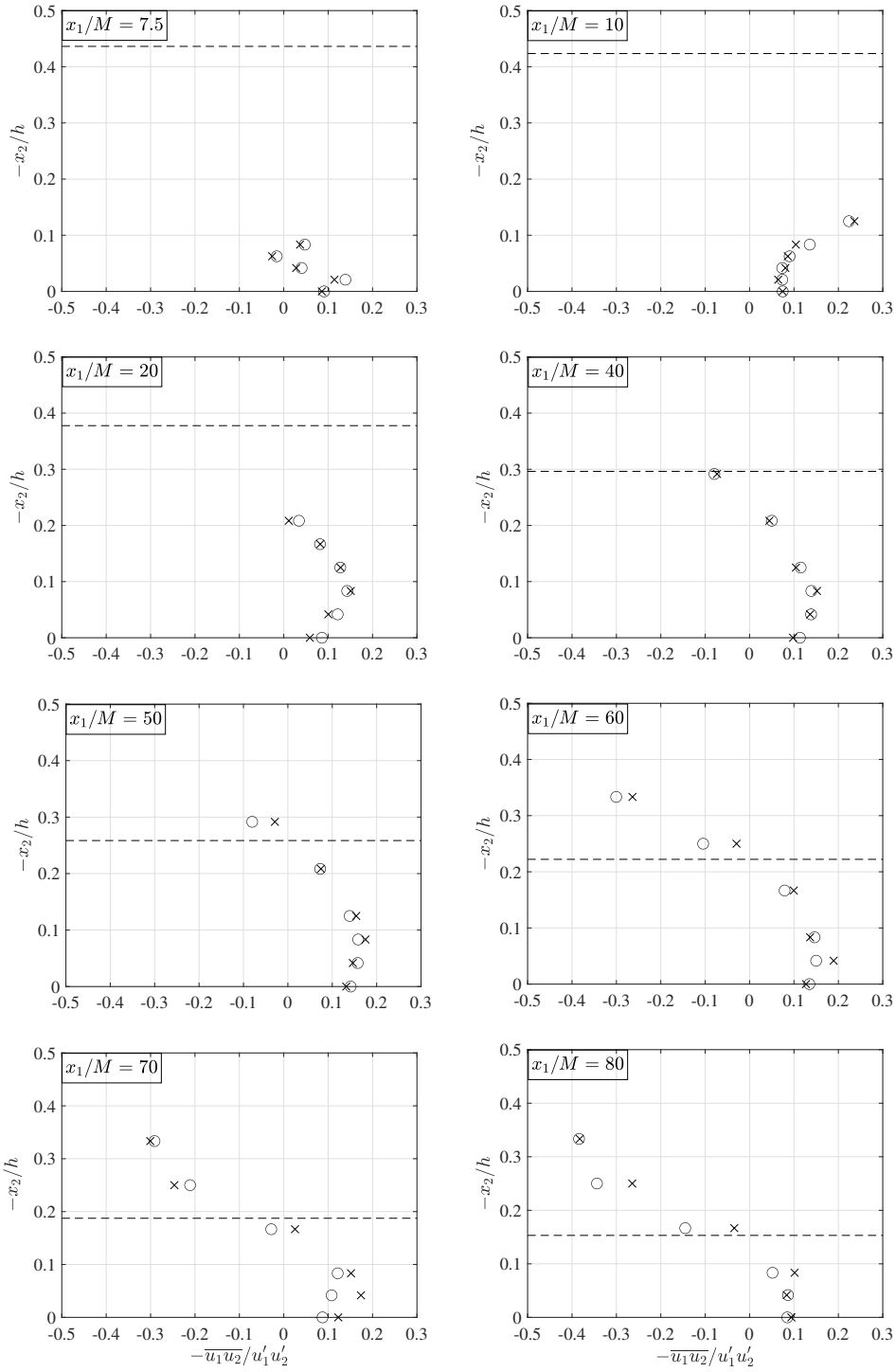

Figure 6.5: Transverse profiles of the time-averaged shear stress correlation coefficient behind the M51 grid in stationary flow (×) and in pulsatile flow (∘); dashed lines mark the estimated edge of the grid turbulence core.

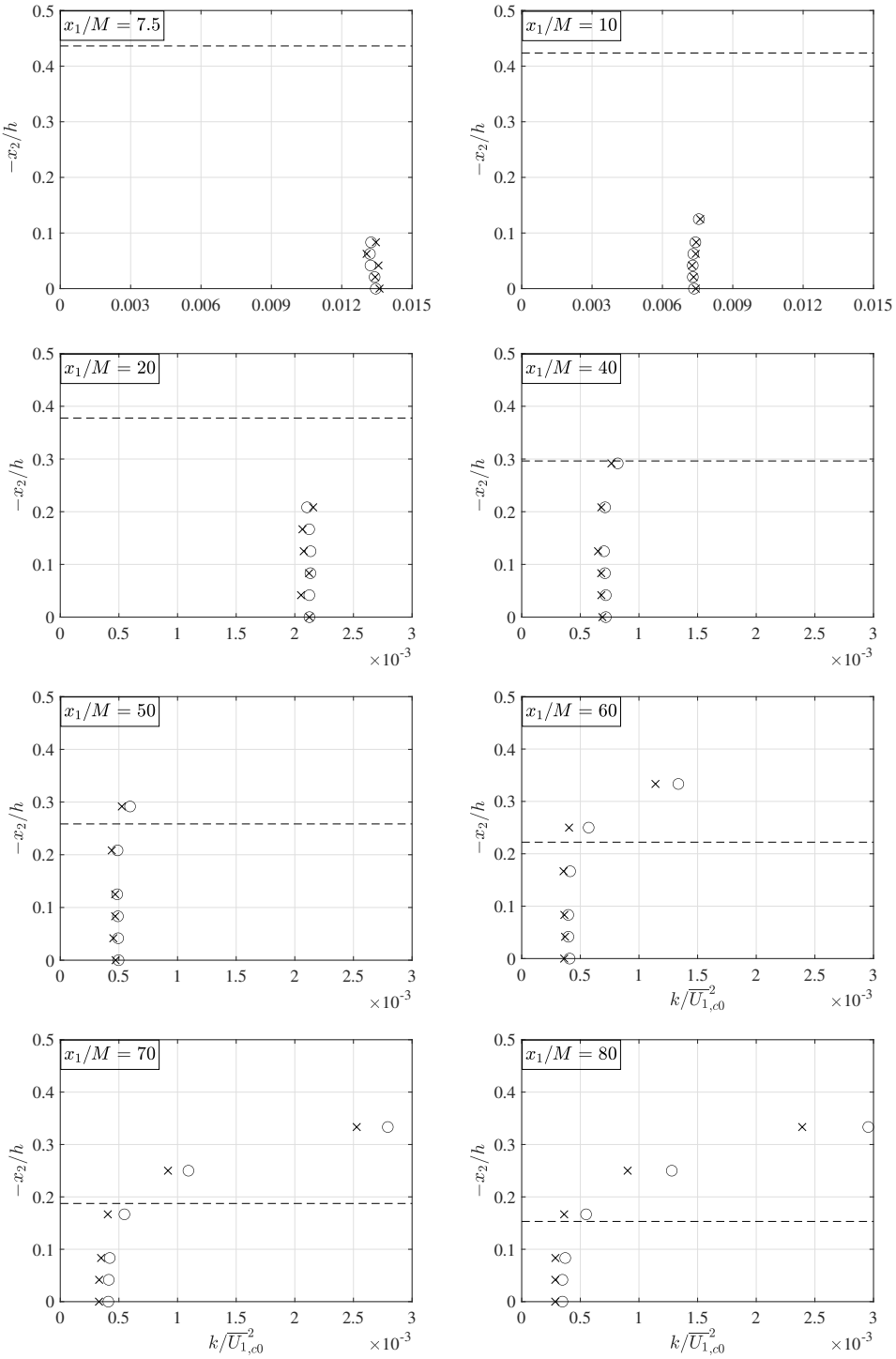

Figure 6.6: Transverse profiles of the time-averaged turbulent kinetic energy behind the M51 grid in stationary flow (×) and in pulsatile flow (∘); dashed lines mark the estimated edge of the grid turbulence core.

energy in the pulsatile flow is noticeably greater than that in the stationary flow, except close to the grid (x_1/M = 10 and 20).

Overall, the transverse profiles of turbulence statistics indicate that flow pulsation generally enhances the turbulence activity both in the grid turbulence core and in the boundary layer.

6.4 Streamwise evolution of the time-averaged turbulence properties

As explained in the previous section, the presented transverse profiles of time-averaged velocity statistics behind the M51 grid and the heated source were not corrected for background velocity fluctuations or temperature fluctuations, although they were corrected for mean temperature changes, measured with the thermistor. In contrast, measurements behind the same grid, but without the heating ribbon, which were only taken along the centreline, were corrected for velocity fluctuations in the test section core without the grid. To quantify the effect of the heated ribbon, we compared the two sets of centreline values. To isolate this effect, we applied the same correction for background fluctuations to the centreline measurements behind the heated ribbon. The corrected centreline values of the streamwise velocity variances for both the heated-ribbon and the no-ribbon cases are presented in Figure 6.7. For both the stationary and the pulsatile cases, the variance of the streamwise fluctuations was $\sim$ 15% smaller in the heated flow at x_1/M = 10. Further downstream, the effect of heated ribbon diminished from $\sim$ 10% at x_1/M = 40 to $\sim$ 5% at x_1/M = 80. In the following, we shall present only velocity measurements in the flow without the ribbon.

The previously presented transverse profiles of time-average velocity statistics for the M51 grid have demonstrated that a substantially wide grid turbulence core existed within the range of at least $x_1/M \leq 80$ ($x_1/h \leq 13.3$). As the boundary layer thickness does not appear to be very sensitive to the "free stream" grid-turbulence, we expect that the flow behind the M19 grid would also have a comparable core region. Therefore, we will present unheated flow turbulence measurements along the test section streamline as representative of the velocity fields in the cores of the flows behind the two grids. Measurements are presented at the same normalised streamwise distances from the two grids, namely, at x_1/M = 10, 20, 30, 40, 50, 60, 70 and 80.

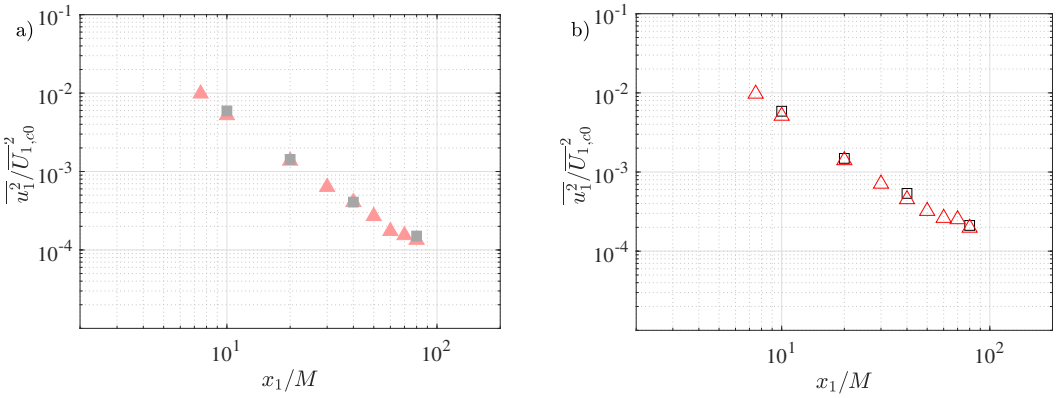

Figure 6.7: Streamwise evolution of the normalised centreline time-averaged variance of the streamwise velocity fluctuations in the unheated (■, □) and heated (▲, △) flow behind the M51 grid; a) stationary flow and b) pulsatile flow.

The decay of the normal Reynolds stresses and the turbulent kinetic energy in stationary grid turbulence away from the grid has commonly been fitted by power laws, for example, as

$$\frac{k}{\overline{U_1}^2} = a\left(\frac{x_1 - x_{10}}{M}\right)^{-n} \tag{6.1}$$

where a, n and x_{10} depend on the grid design. Typical values of n are in the range $1.1 \leq n \leq 1.4$ (Comte-Bellot & Corrsin, 1966; Nedić & Tavoularis, 2016*b*) and a typical value of the effective origin for square-mesh grids is $x_{10}/M = 3.5$ (Comte-Bellot & Corrsin, 1966). Measurements in this study were available for four values of x_1/M, but the values at $x_1/M = 10$ were disregarded as being too close to the grid to be included in the power-law region. It was further considered that determination of both an effective origin and a decay exponent by fitting a power law to three points would be subject to very large uncertainty. Therefore, we approximated the effective origin as $x_{10}/M = 3.5$ and determined the exponent n by least-squares fitting. As shown in Figures 6.8 and 6.9, the fitted exponents to the streamwise normal stress and the turbulent kinetic energy for both grids and for both stationary and pulsatile flows were not too far from those in the literature for stationary grid turbulence. In all cases, the decay exponent in a pulsatile flow was measurably slightly smaller in magnitude than that in the corresponding stationary flow.

The anisotropy indicator values behind the M51 and M19 grids are plotted in Figure 6.10. The two grids produce similar effects on this parameter, with values in the pulsatile

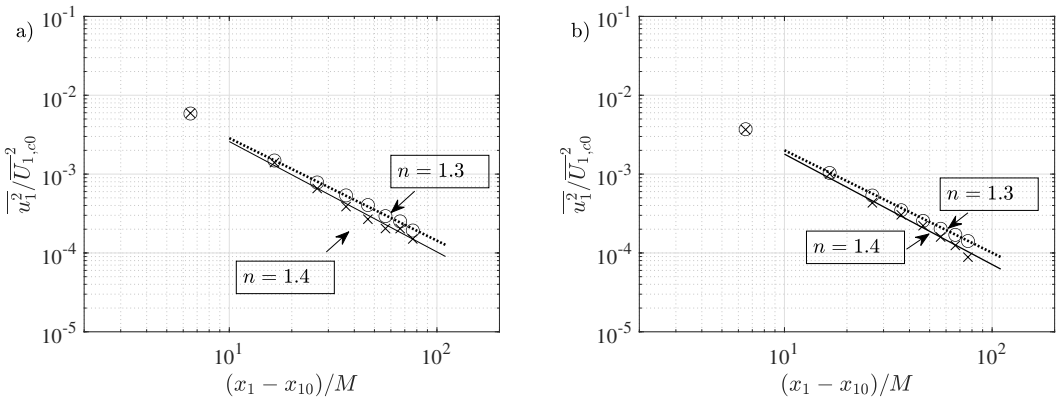

Figure 6.8: Streamwise evolution of the normalised centreline time-averaged variance of the streamwise velocity fluctuations behind a) M51 grid b) M19 grid in stationary flow (×) and pulsatile flow (○).

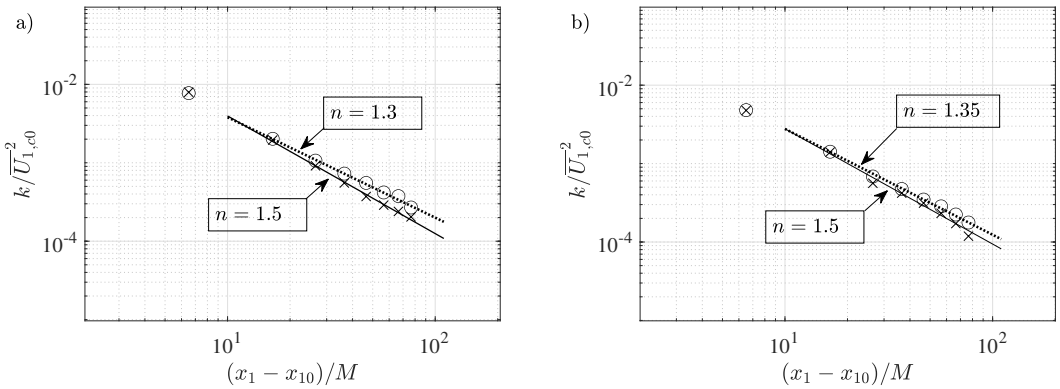

Figure 6.9: Streamwise evolution of the normalised centreline time-averaged turbulent kinetic energy behind a) M51 grid b) M19 grid in stationary flow (×) and pulsatile flow (○).

flow being very slightly larger than the stationary values. Overall, the values are consistent with previous work.

The centreline evolution of the time-averaged integral length scale, normalised by the grid mesh size, is presented in Figure 6.11. Behind both grids, the pulsatile flow is shown to have a smaller integral length scale than that in the stationary flow. The normalised length scale was also found to approximately fit a power-law with an exponent of 0.33 behind both grids in pulsatile flow, and exponents of 0.48 and 0.37 respectively behind the larger and smaller grids in stationary flow. This exponent in the pulsatile flow is smaller than literature

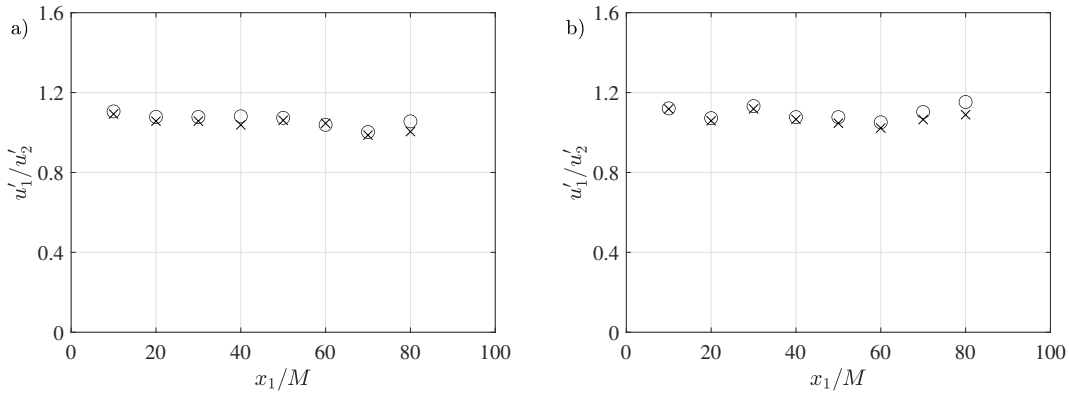

Figure 6.10: Streamwise evolution of the centreline anisotropy behind a) M51 grid b) M19 grid in stationary flow (×) and pulsatile flow (○).

values, which were in the range 0.4 – 0.5, but this difference may be attributed to the zero-crossing method used to determine L_1. A previous study showed that this method can produce exponents from 0.2 to 0.5 (Trush *et al.*, 2020). The Taylor microscale, presented in Figure 6.12, was shown to be greater in the pulsatile than the stationary flow at all locations, except at $x/M = 10$ for the smaller grid, for both grids.

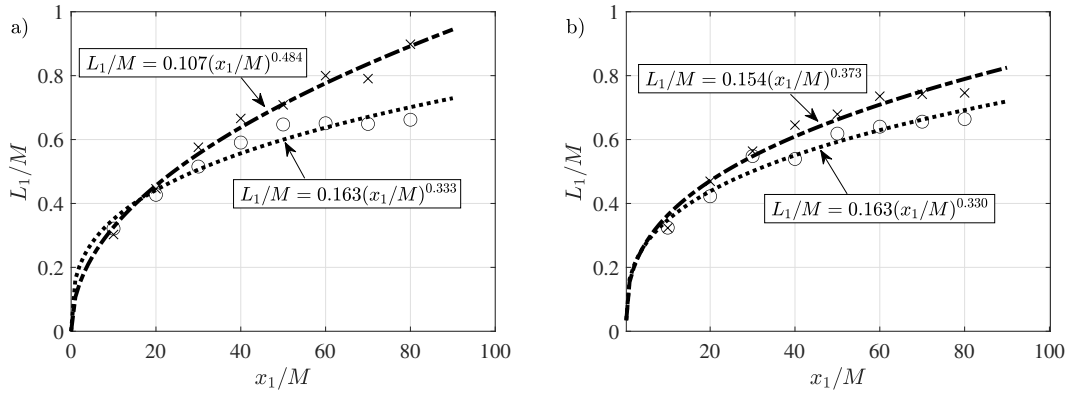

Figure 6.11: Streamwise evolution of the normalised centreline time-averaged integral length scale behind a) M51 grid b) M19 grid in stationary flow (×) and pulsatile flow (○).

As Figure 6.13 shows, the time-averaged turbulence Reynolds number near the grids ($x_1/M = 10$) was not significantly different in the pulsatile and stationary flows. However, as x_1/M increased, Re_λ became larger in the pulsatile flow and the difference generally increased further downstream.

The turbulent kinetic energy dissipation rate was generally larger for the pulsatile flow

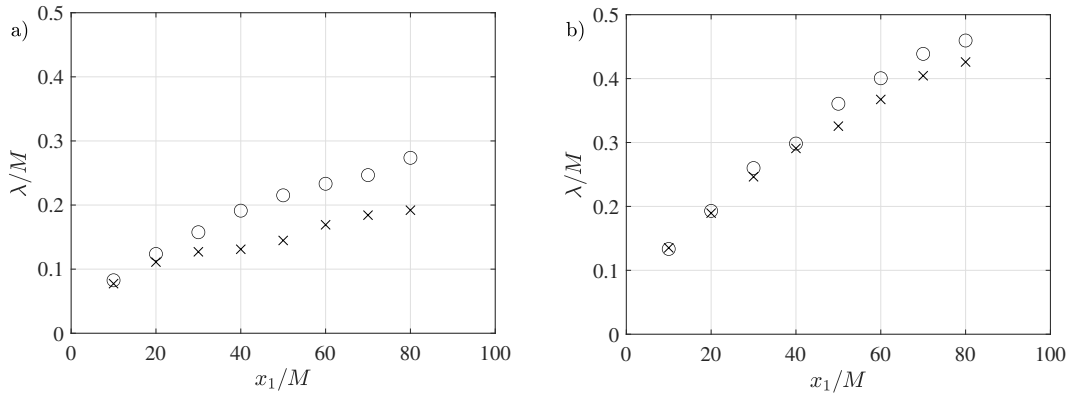

Figure 6.12: Streamwise evolution of the normalised centreline time-averaged Taylor microscale behind a) M51 grid b) M19 grid in stationary flow (×) and pulsatile flow (○).

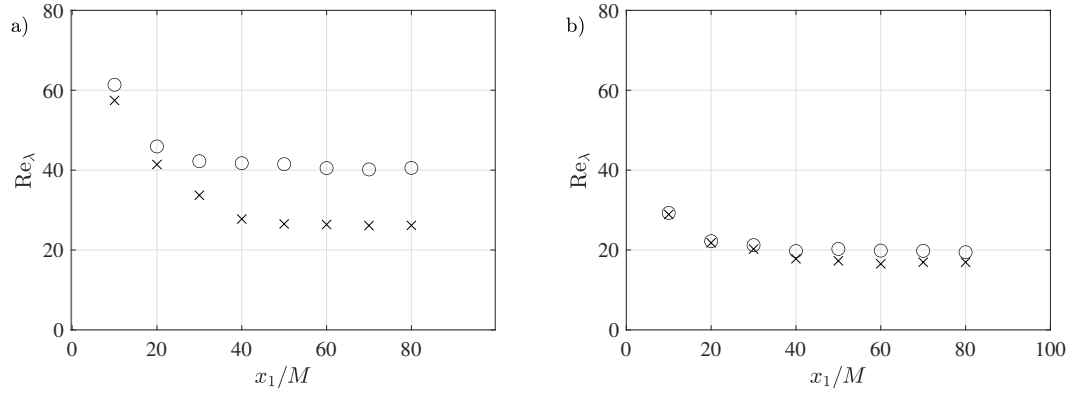

Figure 6.13: Streamwise evolution of the normalised centreline turbulence Reynolds number behind a) the M51 grid and b) the M19 grid in stationary flow (×) and pulsatile flow (○).

than the stationary one (Figure 6.14), with the difference being smaller for the smaller grid. Near either grid, the dissipation parameter was slightly larger in the pulsatile than the stationary flow (Figure 6.15, but, far from either grid, the pulsatile value became significantly smaller than the stationary one, except for the last two values of the larger grid. Even so, the latter two values are not very far from unit and are consistent with previous work (Nedić & Tavoularis, 2016*b*).

Figure 6.16 shows the dependence of the dissipation parameter on the turbulence Reynolds number for the M51 grid for both stationary and pulsatile flow from $10 \leq x_1/M \leq 40$. Previously, Nedić & Tavoularis (2016*b*) showed the presence of a region ($5 \leq x_1/M \leq 25$)

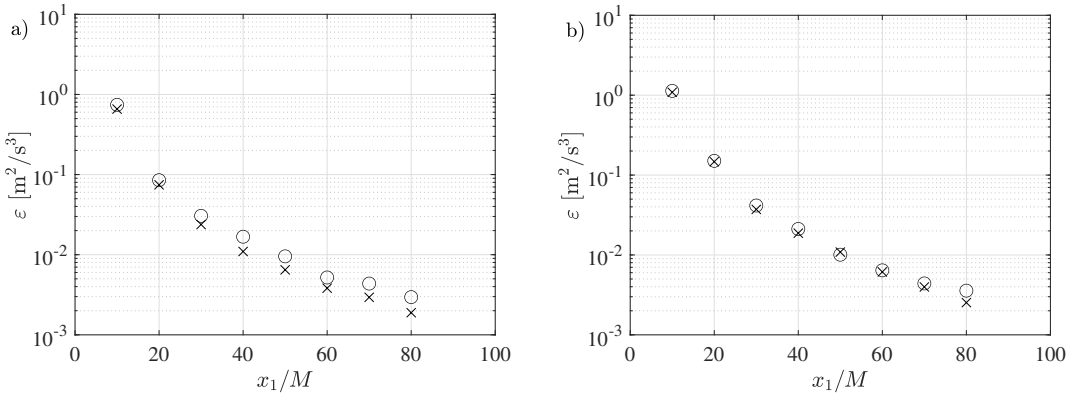

Figure 6.14: Streamwise evolution of the normalised centreline time-averaged turbulent kinetic energy dissipation rate behind a) M51 grid b) M19 grid in stationary flow (×) and pulsatile flow (○).

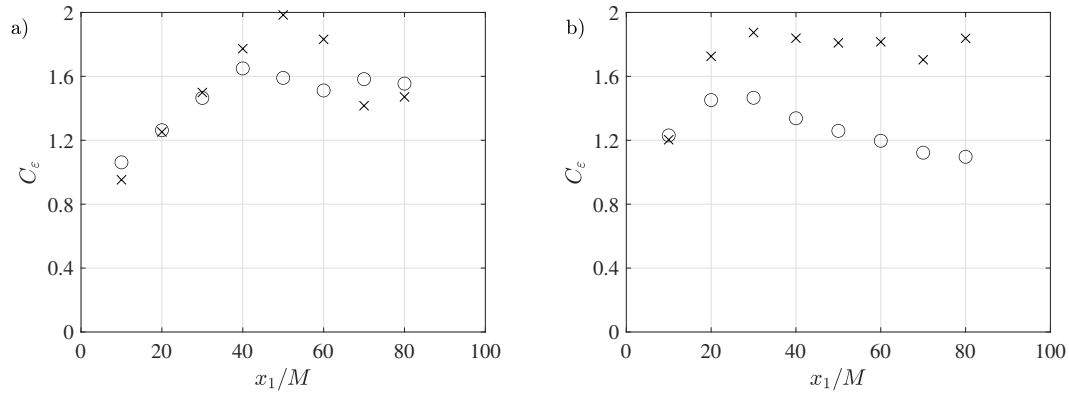

Figure 6.15: Streamwise evolution of the centreline time-averaged dissipation parameter behind a) M51 grid b) M19 grid in stationary flow (×) and pulsatile flow (○).

where $C_\varepsilon \propto \mathrm{Re}_\lambda^{-1}$ for an M80 grid of the same solidity as our M51 grid. In both stationary and pulsatile flows, the expression $C_\varepsilon = A\mathrm{Re}_\lambda^{-1}$ appears to fit well. Results for the M19 grid were not plotted because there was little or no such region for the M19 grid within the experimental x_1/M range (see also Nedić & Tavoularis (2016*a*)).

To quantify the effect of the flow pulsation on the turbulence properties, ratios of time averages along the centreline in pulsatile and stationary flows are plotted in Fig. 6.17. Close to the grid, all ratios were nearly unit, but they deviated from unit downstream. In particular, the ratios of the variance of the streamwise fluctuations and the turbulent kinetic energy exceeded unit significantly by the last measurement station, in the most extreme

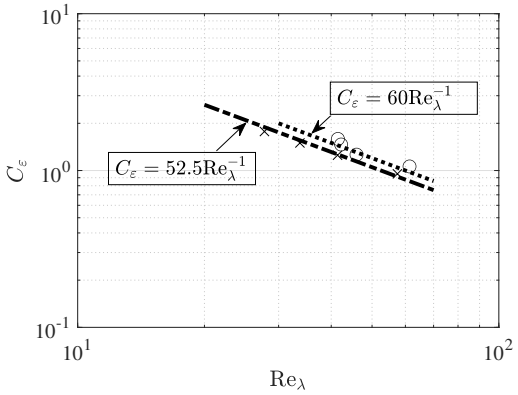

Figure 6.16: Dependence of the dissipation parameter on the turbulence Reynolds number for the M51 grid in stationary flow (×) and pulsatile flow (○).

cases by 60%. This increasing trend may indicate that the energy in the large scale motions added by the flow pulsations are being transferred to the smaller scales as the flow evolves downstream. The anisotropy in the pulsatile flow was slightly larger (by 5%), and the Taylor microscales were also larger in the pulsatile flow (by ∼ 10–50% for λ). Interestingly, the integral length scale was shown to be smaller in the pulsatile flow, by up to 25% smaller for the larger grid. These changes also resulted in an increase in the turbulence Reynolds number (by 15–55%). The turbulent kinetic energy dissipation rate in pulsatile flow was found to be larger by a similar amount (by ∼ 50–60%), which resulted in a decrease of the dissipation parameter (by 20–40%).

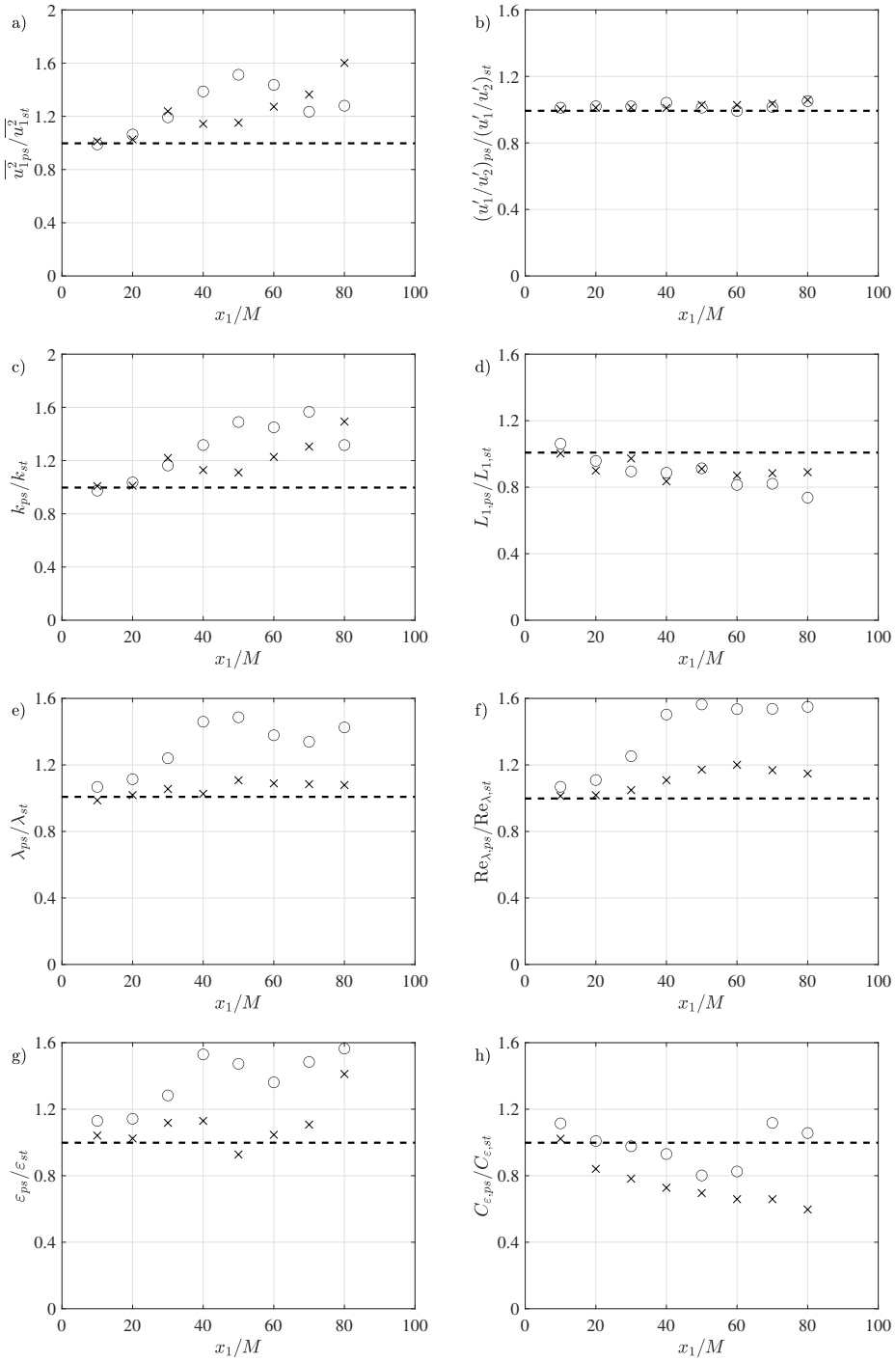

Figure 6.17: a) Centreline evolution of ratios of time-averaged turbulence properties behind the M51 grid (○) and the M19 grid (×) in pulsatile (*ps*) to stationary (*st*) flows: a) streamwise velocity variance; b) anisotropy indicator; c) turbulent kinetic energy; d) integral length scale; e) Taylor microscale; f) turbulence Reynolds number; g) turbulent kinetic energy dissipation rate; and h) dissipation parameter.

6.5 Phase-averaged properties

In this section, phase-averaged turbulence properties of the pulsatile flow are plotted against the cycle time ("phase") $\tau_p = t/T_{cyc}$ to illustrate how property values at each phase contribute to the time average. Representative results are presented in Figure 6.18 for the M51 grid at streamwise location $x_1/M = 40$.

The phase-averaged velocity, shown for reference at the bottom plots (Figure 6.18d,h), had a roughly sinusoidal shape, but with visible asymmetries, which are the result of asymmetries in the action of the oscillating flap. The phase-averaged velocity amplitude decreased somewhat (by $4-5\%$) downstream for the M51 grid, but not for the M19 grid (Figure 6.19). Moreover, the available measurements do not show a significant phase change of the phase-averaged velocity waveform along the test section.

A notable observation that can be made in the plots of various properties is that both the turbulent kinetic energy and its dissipation rate waveforms have also quasi-sinusoidal shapes, but with a phase shift from the mean velocity waveform; this phase shift is such that the minima of the two former properties occur approximately during the time of maximum mean acceleration, whereas their maxima occur during maximum deceleration (namely, at the times of the inflection points in the mean velocity waveform). This is in agreement with extensive previous observations that acceleration suppresses turbulence, while deceleration enhances it. The integral length scale appears to follow, in rough terms and within large scatter, the mean velocity waveform. In contrast, the Taylor microscale varies in the opposite direction, namely, it is larger during low-speed phases and smaller during high-speed ones; this is consistent with the waveforms of k and ε. The relative amplitudes of various properties vary significantly: whereas k and ϵ change strongly during the cycle, L_1 and λ change relatively little. As a result, Re_λ and C_ε, which are compound properties, have intermediate waveforms. A final observation is that, although k and ε dropped below the stationary values during part of the cycle, L_1, λ, Re_λ and C_ε had larger than stationary values throughout the entire cycle or at least during most of it.

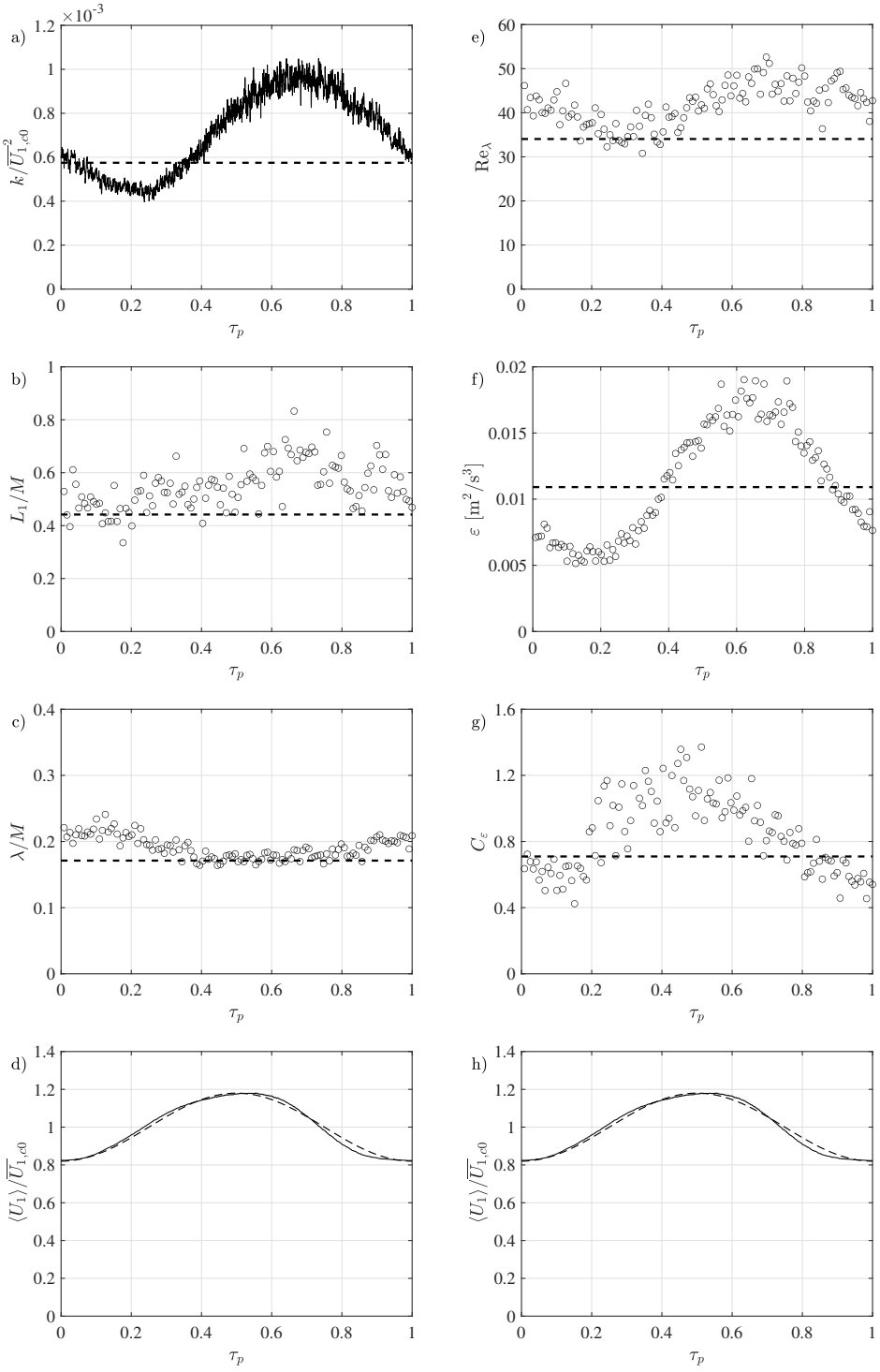

Figure 6.18: Phase-averaged turbulence properties behind the M51 grid in pulsatile flow at $x_1/M = 40$: a) turbulent kinetic energy; b) integral length scale; c) Taylor microscale; e) turbulence Reynolds number; f) turbulent energy dissipation rate; g) dissipation parameter; horizontal dashed lines show the stationary flow values at the same location; d,h) phase-averaged velocity and sine wave with the same amplitude and phase (dashed line).

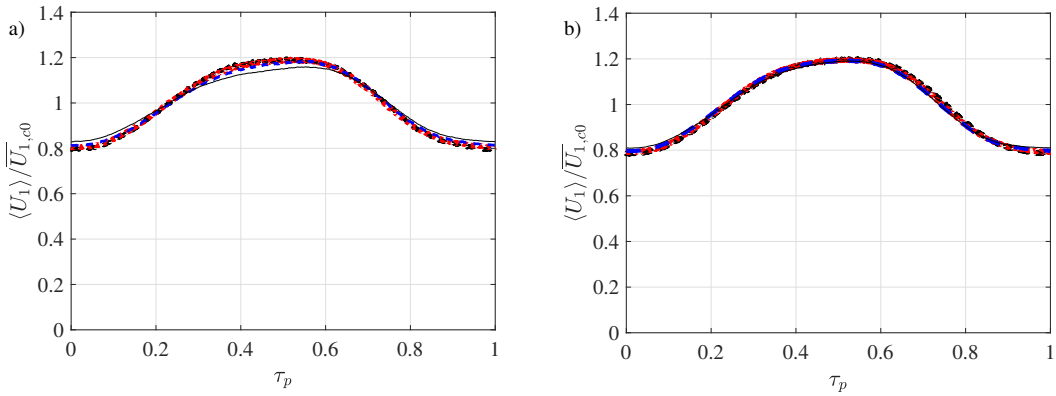

Figure 6.19: Phased averaged velocity of the a) M51 grid and b) M19 grid at different streamwise measurement stations. $x_1/M = 10$ (Black-dashed line), 20 (red-dotted line), 40 (blue-dashed line), and 80 (black-solid line).

6.6 Streamwise evolution of the scalar plume

Transverse profiles of the time-averaged temperature rise ΔT at eight streamwise stations in both stationary and pulsatile grid turbulence are shown in Figure 6.20. All values have been normalised by a constant reference temperature rise $\Delta T_{ref} = 2.1$ K, which is equal to the peak mean temperature rise at $x_1/M = 7.5$. Within the limited resolution of these plots, the temperature values in the pulsatile flow do not appear to be significantly different from those in the stationary flow. It is interesting to notice that this observation applies to both the grid-turbulence core and the boundary layer. To detect quantitatively any possible effect of pulsatility, we performed further analysis by least-squares fitting a Gaussian function to each temperature profile, under the expectation that the plume would have a Gaussian shape (Taylor, 1938; Nedić & Tavoularis, 2016*b*; Duong & Tavoularis, 2022). As Figure 6.21a shows, most data are described fairly well by the fitted Gaussian functions, although, in some profiles, such as at $x/M = 50$ (▷ and ▷), the tail of the Gaussian did not fit very well to the value at the greatest measured distance from the centreline.

The streamwise evolution of the ratio of the normalised centreline temperature rises in the pulsatile and stationary flows is presented in Figure 6.21b. Overall, this ratio remained relatively close to unit, albeit showing significant scatter, but no systematic trend in the boundary-layer-affected region.

The plume half-width σ, which is a measure of the plume spread, was estimated from the fitted Gaussian and is plotted in Figure 6.22a. The plume spread in the pulsatile flow is shown to be slightly larger than the one in the stationary flow for $x_1/M \leq 50$. In this region, the entire plume is contained within the grid-turbulence core. In contrast, for $x_1/M \geq 60$, the plume spread is smaller in the pulsatile flow. In this region, the tail of the plume is within the boundary layer. This observation may be tentatively attributed to an effect of pulsatility on the boundary layer structure, but this topic is outside the scope of the present study. The dashed line in Figure 6.22a separates the regions within which the plume is unaffected and affected by the wall. A power law with an exponent of 0.45 was fitted to the results in the range $7.5 \leq x_1/M \leq 50$, in agreement with previous work on grid turbulence, which found exponents between 0.34 and 0.5 (Taylor, 1938; Anand & Pope, 1985; Stapountzis *et al.*, 1986). The proportionality coefficient in the pulsatile flow was found to be approximately 7% larger than that in the stationary flow.

To quantify the effect of pulsatility on the plume spread, we plotted in Figure (6.22b the ratio of the plume half widths in the pulsatile and stationary flows. The plume spread in the pulsatile flow grows larger than plume spread in the stationary flow to about 7-8% larger after $x/M = 20$, consistent with the ratio of the proportionality coefficients of the fitted power laws in Figure 6.22a. After $x/M = 50$, where the boundary layer begins to interact with the plume, the spread of the pulsatile flow compared to the spread of the stationary flow diminishes by around 10%.

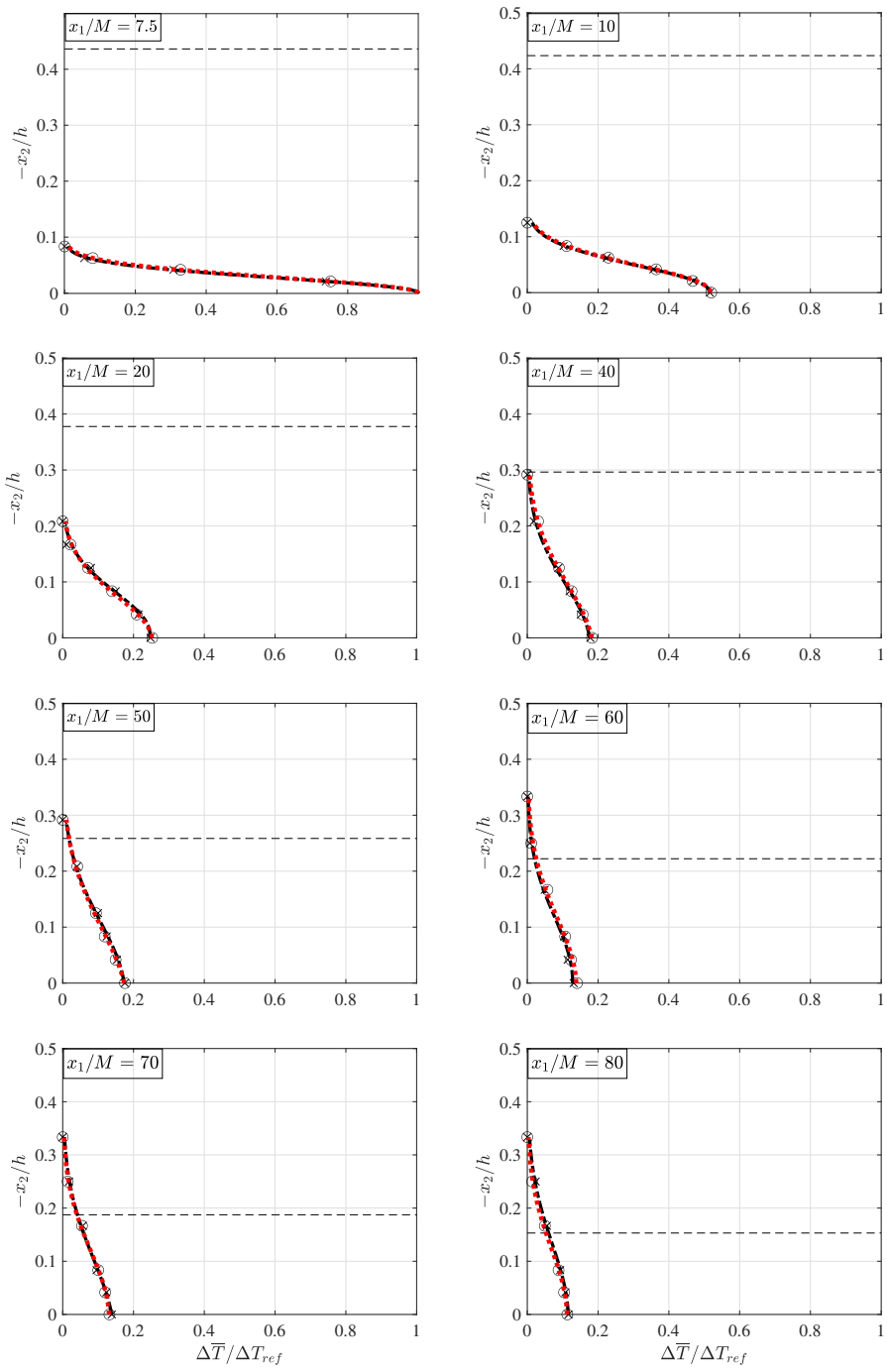

Figure 6.20: Transverse profiles of the normalised time-averaged temperature rise behind the M51 grid in stationary flow (×) and in pulsatile flow (∘); Gaussian functions fitted to the data are shown by black dash-dotted lines for stationary flow and red dotted lines for pulsatile flow; horizontal dashed lines mark the estimated edge of the grid turbulence core; the reference temperature rise was ΔT_{ref} = 2.1 K.

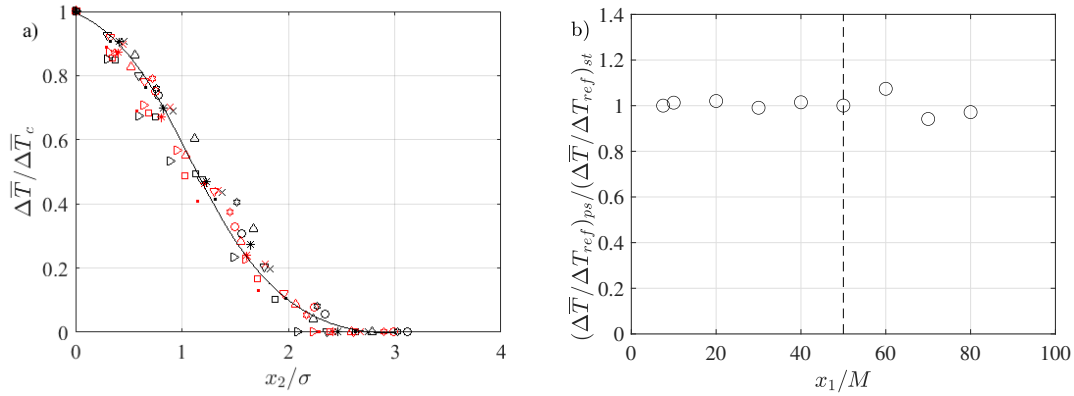

Figure 6.21: a) Transverse profiles of the temperature rise normalised by its local centreline value in stationary flow (red symbols) and in pulsatile flow (black symbols); $x_1/M = 7.5$ ($\circ$), 10 ($\square$), 20 ($\triangle$), 30 ($*$), 40 ($\times$), 50 ($\triangleright$), 60 ($\hexagram$), 70 ($\cdot$) and 80 ($\triangledown$); the solid line is a Gaussian function; b) centreline evolution of the ratio of the normalised centreline temperature rises in pulsatile and stationary flows; the reference temperature rise was $\Delta T_{ref} = 2.1$ K.

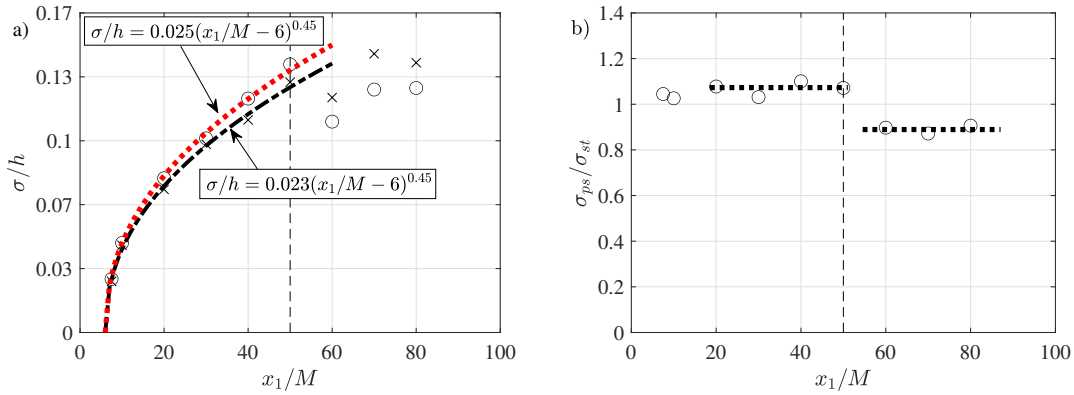

Figure 6.22: a) Plume half width at different streamwise locations in stationary flow ($\times$) and in pulsatile flow ($\circ$); the vertical dashed line marks the furthest downstream location at which the plume spread is essentially unaffected by the boundary layer, and b) centreline evolution of the ratio of the plume half widths in pulsatile and stationary flows; in both plots, vertical dashed lines mark the furthest downstream location at which the plume spread is essentially unaffected by the boundary layer, and in (b), dotted lines show average levels of the half width ratio in the core and in the boundary layer.

Chapter 7

Conclusions and recommendations

7.1 Conclusions

This thesis describes the results of experimental studies on three topics on grid-generated turbulence, which have not been examined in past literature. The first study examined the enhancement of turbulent mixing by porous obstructions. The second study examined the flow field downstream of grids at very low Reynolds numbers, which included turbulent, intermediate and non-turbulent cases. The third study examined the effects of flow pulsation on grid turbulence and turbulent diffusion.

The main conclusions of this work, which expand the current knowledge of grid turbulence, are as follows:

- An array of thin cylinders closely downstream of a passive scalar source positioned near a grid enhances greatly scalar mixing.

- As the Reynolds number decreases to values that are smaller than those examined in the past, grid turbulence undergoes a transformation to an intermediate state, in which the statistical properties of the velocity field increasingly deviate from those in conventional grid turbulence. Further decrease of the Reynolds number results in essentially steady flow behind the grid.

- Flow pulsation increases the turbulent kinetic energy and the spread of a scalar plume in grid turbulence.

The objectives of all three studies have been met and the main findings have practical engineering applications, including the enhancement of turbulent mixing and flow management in wind tunnels. Besides the qualitative contributions to the field, the thesis contains detailed documentation of turbulence and scalar properties under previously unexplored

conditions, which may assist in the development and validation of turbulence theories and computational models.

7.2 Recommendations for future studies

The present work can be extended to additional research on grid turbulence, broadening the scope and providing additional documentation related to the present objectives. Examples of such possible extensions are the following:

- Examination of the effects of flow pulsation on grid turbulence and diffusion under conditions for which the flow is fully turbulent during part of the cycle and in the intermediate or steady state during another part.
- Examination of the grid turbulence decay exponent as the Reynolds number decreases to extremely small values.
- Examination of the effects of obstruction porosity on scalar dispersion and turbulence and attempt to separate the effects of plume deflection by the obstruction elements and additional turbulence produced by the obstruction.
- Examination of the combined effects of flow pulsation and porous obstructions on turbulent mixing.

A secondary finding of the present work was that flow pulsation seems to obstruct diffusion of a scalar from the turbulent free stream to the boundary layer. This issue has significant practical importance, but was not examined thoroughly as it is outside of the present scope. The non-stationary flow facility provides the opportunity for studying the effects of flow pulsation on boundary layers, shear layers, wakes and other shear flows. It also allows the generation of flows with mild favourable and adverse pressure gradients. Each of such investigations would be suitable for a graduate thesis and would require careful planning and substantial effort and time.

References

Adrian, RJ, Christensen, KT & Liu, ZC 2000 Analysis and interpretation of instantaneous turbulent velocity fields. *Exper. Fluids* **29** (3), 275–290.

Anand, MS & Pope, SB 1985 Diffusion behind a line source in grid turbulence. Bradbury, LJS, Durst, F, Launder, BE, Schmidt, FW & Whitelaw JH. In *Turbulent Shear Flows 4*, pp. 46–61. Springer.

Antonia, RA & Chambers, AJ 1980 On the correlation between turbulent velocity and temperature derivatives in the atmospheric surface layer. *Bound. Lay. Meteorol.* **18** (4), 399–410.

Ashok, A, Bailey, SCC, Hultmark, M & Smits, AJ 2012 Hot-wire spatial resolution effects in measurements of grid-generated turbulence. *Exper. Fluids* **53**, 1713–1722.

Azzam, A & Lavoie, P 2019 Experimental investigation of unsteady turbulence using an active grid. In *Proc. TSFP11, Southampton, United Kingdom, July 30–August 2, 2019*.

Azzam, A & Lavoie, P 2023 Unsteady flow generation in a wind tunnel using an active grid. *Exper. Fluids* **64** (2), 29.

Batchelor, GK 1949 Diffusion in a field of homogeneous turbulence. I. Eulerian analysis. *Aust. J. Chem.* **2** (4), 437–450.

Batchelor, GK 1953 *The Theory of Homogeneous Turbulence*. Cambridge University Press.

Batchelor, GK & Townsend, AA 1947 Decay of vorticity in isotropic turbulence. *Proc. R. Soc. Lon. Ser-A* **190** (1023), 534–550.

Bennett, JC & Corrsin, S 1978 Small Reynolds number nearly isotropic turbulence in a straight duct and a contraction. *Phys. Fluids* **21** (12), 2129–2140.

Bos, WJT, Clark, TT & Rubinstein, R 2007 Small scale response and modeling of periodically forced turbulence. *Phys. Fluids* **19** (5), 055107.

Bos, WJT & Rubinstein, R 2017 Mixing in modulated turbulence. Analytical results. *Comput. Fluids* **151**, 102–107.

Brereton, GJ & Reynolds, WC 1987 Experimental Study of the Fluid Mechanics of Unsteady Turbulent Boundary Layers. *Tech. Rep.*. Stanford University, California, Thermosciences Div.

Brereton, GJ, Reynolds, WC & Jayaraman, R 1990 Response of a turbulent boundary layer to sinusoidal free-stream unsteadiness. *J. Fluid Mech.* **221**, 131–159.

Brumley, BH & Jirka, GH 1987 Near-surface turbulence in a grid-stirred tank. *J. Fluid Mech.* **183**, 235–263.

Bruun, HH 1995 *Hot-wire Anemometry Principles and Signal Analysis*. Oxford University Press, Oxford.

Cadot, O, Couder, Y, Daerr, A, Douady, S & Tsinober, A 1997 Energy injection in closed turbulent flows: Stirring through boundary layers versus inertial stirring. *Phys. Rev. E* **56** (1), 427.

Cadot, O, Titon, JH & Bonn, D 2003 Experimental observation of resonances in modulated turbulence. *J. Fluid Mech.* **485**, 161–170.

Cafiero, G, Obligado, M & Vassilicos, JC 2020 Length scales in turbulent free shear flows. *J. Turbul.* **21** (4), 243–257.

Cafiero, G & Vassilicos, JC 2019 Non-equilibrium turbulence scalings and self-similarity in turbulent planar jets. *P. R. Soc. A* **475** (2225), 20190038.

Cekli, HE, Tipton, C & van de Water, W 2010 Resonant enhancement of turbulent energy dissipation. *Phys. Rev. Lett.* **105** (4), 044503.

Cheng, NS & Law, AWK 2001 Measurements of turbulence generated by oscillating grid. *J. Hydraul. Eng.* **127** (3), 201–208.

Chiapponi, L, Longo, S & Tonelli, M 2012 Experimental study on oscillating grid turbulence and free surface fluctuation. *Exp. Fluids* **53** (5), 1515–1531.

Comte-Bellot, G & Corrsin, S 1966 The use of a contraction to improve the isotropy of grid-generated turbulence. *J. Fluid Mech* **25** (4), 657–682.

Comte-Bellot, G & Corrsin, S 1971 Simple eulerian time correlation of full-and narrow-band velocity signals in grid-generated,'isotropic'turbulence. *J. Fluid Mech* **48** (2), 273–337.

Cousteix, J, Houdeville, R & Javelle, JT 1981 Response of a turbulent boundary layer to a pulsation of the external flow with and without adverse pressure gradient. Michel, R, Cousteix, R & Houdeville, R. In *Unsteady Turbulent Shear Flows*, pp. 120–144. Springer.

Dairay, T, Obligado, M & Vassilicos, JC 2015 Non-equilibrium scaling laws in axisymmetric turbulent wakes. *J. Fluid Mech.* **781**, 166–195.

Dickinson, SC & Long, RR 1978 Laboratory study of the growth of a turbulent layer of fluid. *Phys. Fluids* **21** (10), 1698–1701.

Dickinson, SC & Long, RR 1983 Oscillating-grid turbulence including effects of rotation. *J. Fluid Mech.* **126**, 315–333.

Djenidi, L. & Antonia, R. A. 2012 A spectral chart method for estimating the mean turbulent kinetic energy dissipation rate. *Exp. Fluids* **53** (4), 1005–1013.

Djenidi, L. & Antonia, R. A. 2014 Transport equation for the mean turbulent energy dissipation rate in low-grid turbulence. *J. Fluid Mech.* **747**, 288–315.

Djenidi, L, Tardu, SF, Antonia, RA & Danaila, L 2014 Breakdown of Kolmogorov's first similarity hypothesis in grid turbulence. *J. Turbul.* **15** (9), 596–610.

Don, A 2016 Structure of Turbulent Flow in a Rod Bundle. Master's thesis, Université d'Ottawa/University of Ottawa.

Duong, D 2017 Accelerating and Decelerating Flows in a Rod Bundle. Master's thesis, Université d'Ottawa/University of Ottawa.

Duong, D & Tavoularis, S 2022 Enhancement of turbulent mixing by a porous obstruction. *Phys. Rev. Fluids* **7** (12), 124502.

Duong, D & Tavoularis, S 2024 Grid-generated velocity fields at very small reynolds numbers. *Phys. Rev. Fluids* **9** (2), 024607.

Ertunç, Ö., Özyilmaz, N., Lienhart, H., Durst, F. & Beronov, K. 2010 Homogeneity of turbulence generated by static-grid structures. *J. Fluid. Mech.* **654**, 473–500.

Fang, L & Bos, WJT 2023 An EDQNM study of the dissipation rate in isotropic non-equilibrium turbulence. *J. Turb.* pp. 1–18.

Fernando, HJS & De Silva, IPD 1993 Note on secondary flows in oscillating-grid, mixing-box experiments. *Phys. Fluids. A-Fluid* **5** (7), 1849–1851.

Fernando, HJS & Long, RR 1983 The growth of a grid-generated turbulent mixed layer in a two-fluid system. *J. Fluid Mech.* **133**, 377–395.

Fernando, HJS & Long, RR 1985 On the nature of the entrainment interface of a two-layer fluid subjected to zero-mean-shear turbulence. *J. Fluid Mech.* **151**, 21–53.

Finnicum, DS & Hanratty, TJ 1988 Effect of imposed sinusoidal oscillations on turbulent flow in a pipe. *PCH* **10**, 585.

Freymuth, P 1977 Frequency response and electronic testing for constant-temperature hot-wire anemometers. *J Phys. E Sci. Instrum.* **10** (7), 705.

George, W. K. 1992 The decay of homogeneous isotropic turbulence. *Phys. Fluids A* **4** (7), 1492–1509.

Germaine, E, Mydlarski, L, Cortelezzi, L *et al.* 2014 Evolution of the scalar dissipation rate downstream of a concentrated line source in turbulent channel flow. *J. Fluid Mech.* **749**, 227–274.

Gerrard, JH 1971 An experimental investigation of pulsating turbulent water flow in a tube. *J. Fluid Mech.* **46** (1), 43–64.

Gilbrech, DA & Combs, GD 1963 Critical Reynolds numbers for incompressible pulsating flow in tubes. *Devel. Theor.* **1**, 292–304.

Goltsman, AE, Saushin, II & Mikheev, NI 2018 Flow turbulence characteristics in channels under conditions of combined effect of pressure gradient and superimposed flow pulsations. In *Journal of Physics: Conference Series, Novosibirsk, Russian Federation, August 27–30, 2018*. IOP Publishing.

Goto, S & Vassilicos, JC 2015 Energy dissipation and flux laws for unsteady turbulence. *Phys. Lett. A* **379** (16-17), 1144–1148.

Goto, S & Vassilicos, JC 2016 Unsteady turbulence cascades. *Phys. Rev. E* **94** (5), 053108.

Greenblatt, D & Moss, EA 1999 Pipe-flow relaminarization by temporal acceleration. *Phys. Fluids.* **11** (11), 3478–3481.

Greenblatt, D & Moss, EA 2004 Rapid temporal acceleration of a turbulent pipe flow. *J. Fluid Mech.* **514**, 65–75.

He, S & Ariyaratne, C 2011 Wall shear stress in the early stage of unsteady turbulent pipe flow. *J. Hydraul. Eng.* **137** (5), 606–610.

He, S & Jackson, JD 2000 A study of turbulence under conditions of transient flow in a pipe. *J. Fluid Mech.* **408**, 1–38.

He, S & Jackson, JD 2009 An experimental study of pulsating turbulent flow in a pipe. *Eur. J. Mech. B-Fluid* **28** (2), 309–320.

Hearst, RJ & Lavoie, P 2016 Effects of multi-scale and regular grid geometries on decaying turbulence. *J. Fluid Mech.* **803**, 528–555.

Hearst, R Jason & Lavoie, Philippe 2015 The effect of active grid initial conditions on high reynolds number turbulence. *Experiments in Fluids* **56**, 1–20.

Herlina, H 2005 Gas Transfer at the Air-Water Interface in a Turbulent Flow Environment. PhD thesis, Universitätsverlag Karlsruhe, Karlsruhe.

von der Heydt, A, Grossmann, S & Lohse, D 2003*a* Response maxima in modulated turbulence. *Phys. Rev. E* **67** (4), 046308.

von der Heydt, A, Grossmann, S & Lohse, D 2003*b* Response maxima in modulated turbulence. II. Numerical simulations. *Phys. Rev. E* **68** (6), 066302.

Hopfinger, EJ & Toly, JA 1976 Spatially decaying turbulence and its relation to mixing across density interfaces. *J. Fluid Mech.* **78** (1), 155–175.

Horiuti, K & Tamaki, T 2013 Nonequilibrium energy spectrum in the subgrid-scale one-equation model in large-eddy simulation. *Phys. Fluids* **25** (12).

Huang, M. J. & Leonard, A. 1994 Power-law decay of homogeneous turbulence at low reynolds numbers. *Phys. Fluids* **6** (11), 3765–3775.

Hurst, D & Vassilicos, JC 2007 Scalings and decay of fractal-generated turbulence. *Phys. Fluids* **19** (3), 035103.

Hussain, AKMF & Reynolds, WC 1970 The mechanics of an organized wave in turbulent shear flow. *J. Fluid Mech.* **41** (2), 241–258.

Hussain, AKMF & Reynolds, WC 1972 The mechanics of an organized wave in turbulent shear flow. Part 2. Experimental results. *J. Fluid Mech.* **54** (2), 241–261.

Isaza, J. C., Salazar, R. & Warhaft, Z. 2014 On grid-generated turbulence in the near-and far field regions. *J. Fluid Mech.* **753**, 402–426.

Jayaraman, R, Parikh, P & Reynolds, WC 1982 An Experimental Study of the Dynamics of an Unsteady Turbulent Boundary Layer. *Tech. Rep.*. Stanford University, California, Thermosciences Div.

Jayesh & Warhaft, Z. 1992 Probability distribution, conditional dissipation, and transport of passive temperature fluctuations in grid-generated turbulence. *Phys. Fluids A* **4** (10), 2292–2307.

Jerome, FE, Guitton, DE & Patel, RP 1971 Experimental study of the thermal wake interference between closely spaced wires of a X-type hot-wire probe. *Aeronaut. Quart.* **22** (2), 119–126.

Jirka, GH, Herlina, H & Niepelt, A 2010 Gas transfer at the air–water interface: experiments with different turbulence forcing mechanisms. *Exp. Fluids* **49** (1), 319–327.

Kang, H. S., Chester, S. & Meneveau, C. 2003 Decaying turbulence in an active-grid-generated flow and comparisons with large-eddy simulation. *J. Fluid Mech.* **480**, 129–160.

Karlsson, SKF 1959 An unsteady turbulent boundary layer. *J. Fluid Mech.* **5** (4), 622–636.

Karnik, U & Tavoularis, S 1987 Generation and manipulation of uniform shear with the use of screens. *Exper. Fluids* **5** (4), 247–254.

Karnik, U & Tavoularis, S 1989 Measurements of heat diffusion from a continuous line source in a uniformly sheared turbulent flow. *J. Fluid Mech.* **202**, 233–261.

Kerr, RM 1985 Higher-order derivative correlations and the alignment of small-scale structures in isotropic numerical turbulence. *J. Fluid Mech.* **153**, 31–58.

Kistler, AL & Vrebalovich, T 1966 Grid turbulence at large Reynolds numbers. *J. Fluid Mech.* **26** (1), 37–47.

Kolmogorov, AN 1941*a* Dissipation of energy in locally isotropic turbulence. In *Dokl. Akad. Nauk SSSR*, , vol. 32, p. 16.

Kolmogorov, AN 1941*b* On degeneration (decay) of isotropic turbulence in an incompressible viscous liquid. In *Dokl. Akad. Nauk SSSR*, , vol. 31, pp. 538–540.

Kolmogorov, AN 1941*c* The local structure of turbulence in incompressible viscous fluid for very large Reynolds numbers. *Dokl. Akad. Nauk SSSR* **30**, 301.

Krogstad, P-Å & Davidson, P. A. 2011 Freely decaying, homogeneous turbulence generated by multi-scale grids. *J. Fluid Mech.* **680**, 417–434.

Krogstad, P-Å & Davidson, P. A. 2012 Near-field investigation of turbulence produced by multi-scale grids. *Phys. Fluids* **24** (3), 035103.

Kuczaj, AK, Geurts, BJ & Lohse, D 2006 Response maxima in time-modulated turbulence: Direct numerical simulations. *Europhys. Lett.* **73** (6), 851.

Kuczaj, AK, Geurts, BJ, Lohse, D & van de Water, W 2008 Turbulence modification by periodically modulated scale-dependent forcing. *Comput. Fluids* **37** (7), 816–824.

Lacassagne, T, Lyon, A, Simoëns, S, El Hajem, M & Champagne, JY 2020 Flow around an oscillating grid in water and shear-thinning polymer solution at low Reynolds number. *Exp. Fluids* **61** (1), 1–24.

Lacassagne, T, Simoëns, S, El Hajem, M, Lyon, A & Champagne, JY 2019 Oscillating grid turbulence in shear-thinning polymer solutions. *Phys. Fluids* **31** (8), 083102.

Larssen, J. V. & Devenport, W. J. 2011 On the generation of large-scale homogeneous turbulence. *Exp. Fluids* **50** (5), 1207–1223.

Lee, S. K., Djenidi, L., Antonia, R. A. & Danaila, L. 2013 On the destruction coefficients for slightly heated decaying grid turbulence. *Int. J. Heat Fluid Fl.* **43**, 129–136.

Lepore, J & Mydlarski, L 2011 Lateral dispersion from a concentrated line source in turbulent channel flow. *J. Fluid Mech.* **678**, 417.

Li, JD, McKeon, BJ, Jiang, W, Morrison, JF & Smits, AJ 2004 The response of hot wires in high Reynolds-number turbulent pipe flow. *Meas. Sci. Technol.* **15** (5), 789.

Liberzon, A, Holzner, M, Lüthi, B, Guala, M & Kinzelbach, W 2009 On turbulent entrainment and dissipation in dilute polymer solutions. *Phys. Fluids* **21** (3), 035107.

Lodahl, CR, Sumer, BM & Fredsøe, J 1998 Turbulent combined oscillatory flow and current in a pipe. *J. Fluid Mech.* **373**, 313–348.

Lohse, D 2000 Periodically kicked turbulence. *Phys. Rev. E* **62** (4), 4946.

Long, RR 1978 Theory of turbulence in a homogeneous fluid induced by an oscillating grid. *Phys. Fluids* **21** (10), 1887–1888.

Longo, S, Chiapponi, L & Liang, D 2013 Analytical study of the water surface fluctuations induced by grid-stirred turbulence. *Appl. Math. Model* **37** (12-13), 7206–7222.

Lueptow, RM, Breuer, KS & Haritonidis, JH 1988 Computed aided calibration for X-probes applied to wall-bounded turbulent shear flows. *Exp. Fluids* **6**, 115–118.

Manna, M & Vacca, A 2005 Resistance reduction in pulsating turbulent pipe flows. *J. Eng. Gas. Turb. Power* **127** (2), 410–417.

Manna, M, Vacca, A & Verzicco, R 2012 Pulsating pipe flow with large-amplitude oscillations in the very high frequency regime. Part 1. Time-averaged analysis. *J. Fluid Mech.* **700**, 246–282.

Mansour, NN & Wray, AA 1994 Decay of isotropic turbulence at low Reynolds number. *Physics of Fluids* **6** (2), 808–814.

Mao, ZX & Hanratty, TJ 1986 Studies of the wall shear stress in a turbulent pulsating pipe flow. *J. Fluid Mech.* **170**, 545–564.

Mao, ZX & Hanratty, TJ 1992 Measurement of wall shear rate in large amplitude unsteady reversing flows. *Exp. Fluids* **12** (4-5), 342–350.

Maruyama, T, Kuribayashi, T & Mizushina, T 1976 The structure of the turbulence in transient pipe flows. *J. Chem. Eng. Jpn* **9** (6), 431–439.

Mazellier, N & Vassilicos, JC 2010 Turbulence without Richardson–Kolmogorov cascade. *Phys. Fluids* **22** (7), 075101.

McCorquodale, MW & Munro, RJ 2017 Experimental study of oscillating-grid turbulence interacting with a solid boundary. *J. Fluid Mech.* **813**, 768–798.

McCorquodale, MW & Munro, RJ 2018*a* A method for reducing mean flow in oscillating-grid turbulence. *Exp. Fluids* **59** (12), 1–16.

McCorquodale, MW & Munro, RJ 2018*b* Analysis of intercomponent energy transfer in the interaction of oscillating-grid turbulence with an impermeable boundary. *Phys. Fluids* **30** (1), 015105.

McKenna, SP & McGillis, WR 2004 The role of free-surface turbulence and surfactants in air–water gas transfer. *Int. J. Heat Mass Tran.* **47** (3), 539–553.

Menendez, AN 1983 Study of Unsteady Turbulent Boundary Layers. PhD thesis, University of Iowa, Iowa City.

Morikawa, K, Urano, S, Sanada, T & Saito, T 2008 Turbulence modulation induced by bubble swarm in oscillating-grid turbulence. *J. Pow. Ener. Sys.* **2** (1), 330–339.

Mydlarski, L. 2017 A turbulent quarter century of active grids: from Makita (1991) to the present. *Fluid Dyn. Res.* **49** (6), 061401.

Nagami, Y & Saito, T 2013 Measurement of modulation induced by interaction between bubble motion and liquid-phase motion in the decaying turbulence formed by an oscillating-grid. *Particuology* **11** (2), 158–169.

Nedić, J & Tavoularis, S 2016*a* Energy dissipation scaling in uniformly sheared turbulence. *Phys. Rev. E* **93** (3), 033115.

Nedić, J & Tavoularis, S 2016*b* Measurements of passive scalar diffusion downstream of regular and fractal grids. *J. Fluid Mech.* **800**, 358–386.

Nedić, J, Tavoularis, S & Marusic, I 2017 Dissipation scaling in constant-pressure turbulent boundary layers. *Phys. Rev. Fluids* **2** (3), 032601.

Nedić, J, Vassilicos, JC & Ganapathisubramani, B 2013 Axisymmetric turbulent wakes with new nonequilibrium similarity scalings. *Phys. Rev. Lett.* **111** (14), 144503.

Obligado, M, Dairay, T & Vassilicos, JC 2016 Nonequilibrium scalings of turbulent wakes. *Phys. Rev. Fluids* **1** (4), 044409.

Patel, MH & Young, AD 1977 On turbulent boundary layers in oscillatory flow. *P. Roy. Soc. Lond. A Mat.* **353** (1672), 121–144.

Pope, S. B. 2000 *Turbulent Flows*. Cambridge University Press.

Pritchard, P. J. & Mitchell, J. W. 2016 *Fox and McDonald's Introduction to Fluid Mechanics*. John Wiley & Sons.

Rahman, S & Webster, DR 2005 The effect of bed roughness on scalar fluctuations in turbulent boundary layers. *Exp. Fluids* **38** (3), 372–384.

Ramaprian, BR & Tu, SW 1980 An experimental study of oscillatory pipe flow at transitional Reynolds numbers. *J. Fluid Mech.* **100** (3), 513–544.

Ramaprian, BR & Tu, SW 1983 Fully developed periodic turbulent pipe flow. Part 2. The detailed structure of the flow. *J. Fluid Mech.* **137**, 59–81.

Ranade, P, Duvvuri, S, McKeon, B, Gordeyev, S, Christensen, K & Jumper, EJ 2019 Turbulence amplitude amplification in an externally forced, subsonic turbulent boundary layer. *AIAA J.* **57** (9), 3838–3850.

Rastello, M, Michallet, H & Marié, JL 2020 Sediment erosion in zero-mean-shear turbulence. *Phys. Fluids* **32** (3), 036601.

Raushan, PK, Singh, SK & Debnath, K 2019 Grid-generated turbulence in pulsating flow under the rigid boundary influence. *Eur. J. Mech. B Fluid* **78**, 291–305.

Raushan, PK, Singh, SK & Debnath, K 2021 Turbulence characteristics of oscillating flow through passive grid. *Ocean Eng.* **224**, 108727.

Reynolds, Osborne 1883 Xxix. an experimental investigation of the circumstances which determine whether the motion of water shall be direct or sinuous, and of the law of resistance in parallel channels. *Philos. T. R. Soc. Lond.* (174), 935–982.

Reynolds, WC & Hussain, AKMF 1972 The mechanics of an organized wave in turbulent shear flow. Part 3. Theoretical models and comparisons with experiments. *J. Fluid Mech.* **54** (2), 263–288.

Rind, E & Tavoularis, S 2012 Design, Instrumentation and Performance of a Largescale Rod-Bundle Air Flow Facility. *Tech. Rep.*. Technical Report UO-MCG-BF-2012-01, University of Ottawa, Ontario, Canada.

Ronneberger, D & Ahrens, CD 1977 Wall shear stress caused by small amplitude perturbations of turbulent boundary-layer flow: an experimental investigation. *J. Fluid Mech.* **83** (3), 433–464.

Saddoughi, SG & Veeravalli, SV 1994 Local isotropy in turbulent boundary layers at high reynolds number. *J. Fluid Mech.* **268**, 333–372.

Sakai, Y, Nakamura, I, Miyata, M & Tsunoda, H 1986 Diffusion of matter from a continuous point source in uniform mean shear flows: 2nd report, characteristics of concentration fluctuation intensity. *Bull. JSME* **29** (250), 1149–1155.

San, L, Long, T & Liu, C 2017 Algal bioproductivity in turbulent water: An experimental study. *Water* **9** (5), 304.

Sarpkaya, T 1966 Experimental determination of the critical Reynolds number for pulsating Poiseuille flow. *ASME Digital Collection* .

Seoud, RE & Vassilicos, JC 2007 Dissipation and decay of fractal-generated turbulence. *Phys. Fluids* **19** (10), 105108.

Shemer, L & Kit, E 1984 An experimental investigation of the quasisteady turbulent pulsating flow in a pipe. *Phys. Fluids* **27** (1), 72–76.

Shemer, L, Wygnanski, I & Kit, E 1985 Pulsating flow in a pipe. *J. Fluid Mech.* **153**, 313–337.

Shuy, EB 1996 Wall shear stress in accelerating and decelerating turbulent pipe flows. *J. Hydraul. Res.* **34** (2), 173–183.

Sreenivasan, KR 1984 On the scaling of the turbulence energy dissipation rate. *Phys. Fluids* **27** (5), 1048–1051.

Sreenivasan, KR, Deshpande, SM, Prabhu, A & Viswanath, PR 1995 The energy dissipation in turbulent shear flows. In *Symposium on Developments in Fluid Dynamics and Aerospace Engineering*, pp. 159–190. Interline Bangalore, India.

Stapountzis, H, Sawford, BL, Hunt, JCR & Britter, RE 1986 Structure of the temperature field downwind of a line source in grid turbulence. *J. Fluid Mech.* **165**, 401–424.

Stettler, JC & Hussain, AKMF 1986 On transition of the pulsatile pipe flow. *J. Fluid Mech.* **170**, 169–197.

Tardu, SF, Binder, G & Blackwelder, R 1987 Response of turbulence to large amplitude oscillations in channel flow. Comte-Bellot, G & Mathieu, J. In *Advances in turbulence*, pp. 546–555. Springer.

Tardu, SF & da Costa, P 2005 Experiments and modeling of an unsteady turbulent channel flow. *AIAA J.* **43** (1), 140–148.

Tavoularis, S, Bennett, JC & Corrsin, S 1978 Velocity-derivative skewness in small Reynolds number, nearly isotropic turbulence. *J. Fluid Mech.* **88** (1), 63–69.

Tavoularis, S & Corrsin, S 1981*a* Experiments in nearly homogeneous turbulent shear flow with a uniform mean temperature gradient. Part 2. the fine structure. *J. Fluid Mech.* **104**, 349–367.

Tavoularis, S & Corrsin, S 1981*b* Experiments in nearly homogenous turbulent shear flow with a uniform mean temperature gradient. Part 1. *J. Fluid Mech.* **104**, 311–347.

Tavoularis, S & Nedić, J 2017 Taylorian diffusion in mildly inhomogeneous turbulence. *Int. J. Heat Fluid Fl.* **67**, 116–121.

Tavoularis, S & Nedić, J 2024 *Measurement in Fluid Mechanics*. Cambridge University Press.

Taylor, GI 1938 The spectrum of turbulence. *P. Roy. Soc. Lond. A Mat.* **164** (919), 476–490.

Thompson, SM & Turner, JS 1975 Mixing across an interface due to turbulence generated by an oscillating grid. *J. Fluid Mech.* **67** (2), 349–368.

Trush, A, Pospíšil, S & Kozmar, H 2020 Comparison of turbulence integral length scale determination methods. *WIT Trans. Eng. Sci.* **128**, 113–123.

Tu, SW & Ramaprian, BR 1983 Fully developed periodic turbulent pipe flow. Part 1. Main experimental results and comparison with predictions. *J. Fluid Mech.* **137**, 31–58.

Tuzi, R & Blondeaux, P 2008 Intermittent turbulence in a pulsating pipe flow. *J. Fluid Mech.* **599**, 51–79.

Uberoi, MS & Corrsin, S 1952 Diffusion of heat from a line source in isotropic turbulence. *Tech. Rep.* 1142. National Advisory Committee for Aeronautics.

Uberoi, MS & Freymuth, P 1969 Spectra of turbulence in wakes behind circular cylinders. *Phys. Fluids* **12** (7), 1359–1363.

Valente, PC & Vassilicos, JC 2011 The decay of turbulence generated by a class of multi-scale grids. *J. Fluid Mech.* **687**, 300–340.

Valente, PC & Vassilicos, JC 2012 Universal dissipation scaling for nonequilibrium turbulence. *Phys. Rev. Lett.* **108** (21), 214503.

Valente, P. C. & Vassilicos, J. C. 2014 The non-equilibrium region of grid-generated decaying turbulence. *J. Fluid Mech.* **744**, 5–37.

Van Atta, CW & Antonia, RA 1980 Reynolds number dependence of skewness and flatness factors of turbulent velocity derivatives. *Phys. Fluids* **23** (2), 252–257.

Vardy, AE & Brown, JMB 2003 Transient turbulent friction in smooth pipe flows. *J. Sound Vib.* **259** (5), 1011–1036.

Vassilicos, JC 2015 Dissipation in turbulent flows. *Annu. Rev. Fluid Mech.* **47**, 95–114.

Verso, L, van Reeuwijk, M & Liberzon, A 2017 Steady state model and experiment for an oscillating grid turbulent two-layer stratified flow. *Phys. Rev. Fluids* **2** (10), 104605.

Wang, Y, Cai, WH, Wei, TZ, Wang, L & Li, FC 2015 Experimental study on two-oscillating grid turbulence with polymer additives. In *Fluids Engineering Division Summer Meeting*, , vol. 57212, p. V001T15A008. American Society of Mechanical Engineers.

Wang, Y, Cai, WH, Wei, TZ, Zhang, HN, Wang, L & Li, FC 2016 Proper orthogonal decomposition analysis for two-oscillating grid turbulence with viscoelastic fluids. *Adv. Mec. Eng.* **8** (11), 1687814016679773.

Warhaft, Z 1984 The interference of thermal fields from line sources in grid turbulence. *J. Fluid Mech.* **144**, 363–387.

Webster, DR, Rahman, S & Dasi, LP 2003 Laser-induced fluorescence measurements of a turbulent plume. *J. Eng. Mech.* **129** (10), 1130–1137.

White, Frank M, Ng, CO & Saimek, S 2011 *Fluid mechanics*. McGraw-Hill, cop.

Wyngaard, JC 1969 Spatial resolution of the vorticity meter and other hot-wire arrays. *Journal of Physics E: Scientific Instruments* **2** (11), 983.

Xuequan, E & Hopfinger, EJ 1986 On mixing across an interface in stably stratified fluid. *J. Fluid Mech.* **166**, 227–244.

Yang, Y, Chahine, R, Rubinstein, R & Bos, WJT 2019 Passive scalar mixing in modulated turbulence. *Fluid Dyn. Res.* **51** (4), 045501.

Yao, N, Wang, Y, Liu, J, Sun, X, Hao, Z, Liu, Y, Chen, S & Wang, G 2021 Bubble rise characteristics in oscillating grid turbulence. *Miner Eng.* **164**, 106832.

Yellin, EL 1966 Laminar-turbulent transition process in pulsatile flow. *Circ. Res.* **19** (4), 791–804.

Zheng, Y, Nagata, K & Watanabe, T 2021 Energy dissipation and enstrophy production/destruction at very low Reynolds numbers in the final stage of the transition period of decay in grid turbulence. *Phys. Fluids* **33** (3), 035147.

Zhou, T., Antonia, R. A. & Chua, L. 2002 Performance of a probe for measuring turbulent energy and temperature dissipation rates. *Exp. Fluids* **33** (2), 334–345.

Zhou, T., Antonia, R. A., Danaila, L. & Anselmet, F. 2000 Transport equations for the mean energy and temperature dissipation rates in grid turbulence. *Exp. Fluids* **28** (2), 143–151.

Appendix A

Corrections for measured statistical properties

This part of the appendix contains the correction methods to the measured and calculated properties in both the steady flow and pulsatile flow conditions, which are presented in Tables A.1 and A.4. The same subscript notation is used for other corrected variables. Typical levels of noise contamination for background and corrected values for directly measured properties are presented in Tables A.2 and A.5. It is noted that at the very low speeds, the flow is steady, and thus the signal measured related to the fluctuations is expected to be mostly noise, and at higher speeds where the flow is turbulent, the contamination level decreases drastically. Typical levels of noise contamination for background and corrected values for calculated properties are presented in Tables A.3 and A.6. Overall, the corrections for the low speed were are larger and becoming negligible at higher speeds. Although the corrections were large at the low speeds, the values of the properties were also very small.

Table A.1: Summary of correction methods for measured and calculated stationary grid turbulence properties.

Property
$u_1'^2 = u_{1m}'^2 - u_{1bm}'^2$
$u_2'^2 = u_{2m}'^2 - u_{2bm}'^2$
$\overline{(\partial u_1/\partial t)^2} = \overline{(\partial u_1/\partial t)_m^2} - \overline{(\partial u_1/\partial t)_{bm}^2}$
$\overline{(\partial u_1/\partial x_1)^3} = \overline{(\partial u_1/\partial x_1)_m^3}$
$\overline{(\partial u_1/\partial t_1)^4} = \overline{(\partial u_1/\partial t_1)_m^4} - \overline{(\partial u_1/\partial t_1)_{bm}^4}$
$\overline{(\partial^2 u_1/\partial t^2)^2} = \overline{(\partial^2 u_1/\partial t^2)_m^2} - \overline{(\partial^2 u_1/\partial t^2)_{bm}^2}$
$R_m(t,\tau) = \frac{u_{1m}(t)u_{1m}(t+\tau)}{u_{1m}^2(t)}$
$R(t,\tau) = \frac{u_{1m}(t)u_{1m}(t+\tau) - u_{1bm}(t)u_{1bm}(t+\tau)}{u_{1m}^2(t) - u_{1bm}^2(t)}$
$L_{1m} = \overline{U}_1 \int_t^{t+\tau_0} R_m(t,\tau)d\tau$
$L_1 = \overline{U}_1 \int_t^{t+\tau_0} R(t,\tau)d\tau$
$\lambda_m = \overline{U}_1 \left[u_{1m}'^2/\overline{(\partial u_1/\partial t)_m^2}\right]^{1/2}$
$\lambda = \overline{U}_1 \left[u_1'^2/\overline{(\partial u_1/\partial t)^2}\right]^{1/2}$
$\mathrm{Re}_{\lambda m} = u_{1m}'\lambda_m/\nu$
$\mathrm{Re}_\lambda = u_1'\lambda/\nu$
$\varepsilon_m = 15\nu u_{1m}'^2/\lambda_m^2$
$\varepsilon = 15\nu u_1'^2/\lambda^2$
$\eta_m = \left(\nu^3/\varepsilon_m\right)^{1/4}$
$\eta = \left(\nu^3/\varepsilon\right)^{1/4}$
$S_m = \frac{\overline{(\partial u_1/\partial x_1)_m^3}}{\left[\overline{(\partial u_1/\partial x_1)_m^2}\right]^{3/2}}$
$S = \frac{\overline{(\partial u_1/\partial x_1)^3}}{\left[\overline{(\partial u_1/\partial x_1)^2}\right]^{3/2}}$
$F_m = \frac{\overline{(\partial u_1/\partial x_1)_m^4}}{\left[\overline{(\partial u_1/\partial x_1)_m^2}\right]^2}$
$F = \frac{\overline{(\partial u_1/\partial x_1)^4}}{\left[\overline{(\partial u_1/\partial x_1)^2}\right]^2}$
$G_m = u_{1m}'^2 \frac{\overline{(\partial^2 u_1/\partial x_1^2)_m^2}}{\left[\overline{(\partial u_1/\partial x_1)_m^2}\right]^2}$
$G = u_1'^2 \frac{\overline{(\partial^2 u_1/\partial x_1^2)^2}}{\left[\overline{(\partial u_1/\partial x_1)^2}\right]^2}$
$C_{\varepsilon m} = (L_1\varepsilon_m)/u_{1m}'^3$
$C_\varepsilon = (L_1\varepsilon)/u_1'^3$

Table A.2: Summary of noise contamination and measured values for different variables for different flow conditions in stationary grid turbulence at $x_1/M = 30$.

Grid	$\overline{U_1}$ [m/s]	$u_1'^2$ [m^2/s^2] ($u_{1m}'^2$ [m^2/s^2])	$u_2'^2$ [m^2/s^2] ($u_{2m}'^2$ [m^2/s^2])	$\overline{(\partial u_1/\partial t)^2}$ [m^2/s^4] ($\overline{(\partial u_1/\partial t)^2}_m$ [m^2/s^4])	$\overline{(\partial u_1/\partial t_1)^4}$ [m^4/s^8] ($\overline{(\partial u_1/\partial t_1)^4}_m$ [m^4/s^8])	$\overline{(\partial^2 u_1/\partial t^2)^2}$ [m^2/s^6] ($\overline{(\partial^2 u_1/\partial t^2)^2}_m$ [m^2/s^6])
–	0	3.6×10^{-7}	3.4×10^{-7}	0.8	0.5	1.5×10^{8}
–	0.4	5.2×10^{-6}	6.0×10^{-7}	0.4	1.1	0.9×10^{8}
		(5.6×10^{-6})	(9.4×10^{-7})	(1.2)	(1.6)	(2.4×10^{8})
	0.6	7.2×10^{-6}	6.1×10^{-7}	0.5	1.9	1.3×10^{8}
		(7.5×10^{-6})	(9.5×10^{-7})	(1.3)	(2.4)	(2.8×10^{8})
	1.3	6.6×10^{-5}	1.4×10^{-5}	10	209	7.3×10^{8}
		(6.6×10^{-5})	(1.4×10^{-5})	(11)	(210)	(8.8×10^{8})
	4.0	1.1×10^{-4}	3.7×10^{-5}	31	1050	5.7×10^{9}
		(1.1×10^{-4})	(3.7×10^{-5})	(32)	(1050)	(5.9×10^{9})
M19	0.4	2.8×10^{-5}	6.1×10^{-6}	1.8	10	2.9×10^{8}
		(3.3×10^{-5})	(7.1×10^{-6})	(3.1)	(12)	(5.3×10^{8})
	1.3	6.4×10^{-4}	4.8×10^{-4}	25	2400	1.7×10^{9}
		(7.0×10^{-4})	(4.9×10^{-4})	(36)	(2600)	(2.6×10^{9})
	4.0	5.6×10^{-3}	4.6×10^{-3}	5400	1.1×10^{8}	2.3×10^{10}
		(5.7×10^{-3})	(4.7×10^{-3})	(5400)	(1.1×10^{8})	(2.9×10^{10})
M13	0.4	2.4×10^{-5}	2.5×10^{-5}	0.8	2.2	0.4×10^{8}
		(3.0×10^{-5})	(2.6×10^{-5})	(2.1)	(3.8)	(2.7×10^{8})
	1.3	9.3×10^{-4}	9.0×10^{-4}	45	7100	5.6×10^{8}
		(1.0×10^{-3})	(9.1×10^{-4})	(56)	(7300)	(1.4×10^{9})
	4.0	9.8×10^{-3}	9.1×10^{-3}	12900	7.5×10^{8}	8.4×10^{10}
		(1.0×10^{-2})	(9.2×10^{-3})	(12900)	(7.5×10^{8})	(9.0×10^{10})
M3A	0.6	1.1×10^{-5}	4.2×10^{-6}	1.2	4.6	1.4×10^{8}
		(1.9×10^{-5})	(5.2×10^{-6})	(2.4)	(6.9)	(4.2×10^{8})
	1.3	4.8×10^{-4}	4.6×10^{-4}	120	57300	1.7×10^{9}
		(5.3×10^{-4})	(4.7×10^{-4})	(130)	(57500)	(2.5×10^{9})
	4.0	1.1×10^{-2}	7.4×10^{-3}	37000	5.4×10^{9}	3.2×10^{11}
		(1.1×10^{-2})	(7.4×10^{-3})	(37000)	(5.4×10^{9})	(3.2×10^{11})
M3B	0.6	1.4×10^{-5}	5.9×10^{-7}	0.6	1.0	8.8×10^{7}
		(2.1×10^{-5})	(1.5×10^{-6})	(1.8)	(3.3)	(3.6×10^{8})
	1.3	1.7×10^{-3}	1.2×10^{-3}	460	783000	1.5×10^{9}
		(1.7×10^{-3})	(1.2×10^{-3})	(470)	(783000)	(2.3×10^{9})
	4.0	1.1×10^{-2}	8.5×10^{-3}	49300	1.0×10^{10}	7.5×10^{11}
		(1.1×10^{-2})	(8.5×10^{-3})	(49300)	(1.0×10^{10})	(7.6×10^{11})

Table A.3: Summary of measured and corrected values for different turbulence variables for different flow conditions in stationary grid turbulence at $x_1/M = 30$.

Grid	$\overline{U_1}$ [m/s]	λ [m] (λ_m [m])	Re_λ ($\mathrm{Re}_{\lambda,m}$)	η [m] (η_m [m])	S (S_m)	F (F_m)	G (G_m)	C_ε $C_{\varepsilon,m}$
–	0	–	–	–	0.0054	0.79	81	–
–	0.4	1.0×10^{-3}	0.16	1.3×10^{-3}	0.01	6.8	2900	3200
		(1.0×10^{-3})	(0.16)	(1.3×10^{-3})	(0.01)	(1.0)	(930)	(3200)
	0.6	1.6×10^{-3}	0.5	1.2×10^{-3}	0.02	7.6	1150	1000
		(1.6×10^{-3})	(0.5)	(1.2×10^{-3})	(0.02)	(1.3)	(1150)	(1000)
	1.3	3.1×10^{-3}	1.65	1.2×10^{-3}	0.02	2.1	500	280
		(3.1×10^{-3})	(1.65)	(1.2×10^{-3})	(0.02)	(1.8)	(500)	(280)
	4.0	7.5×10^{-3}	5.1	1.7×10^{-3}	0.004	1.1	640	66
		(7.5×10^{-3})	(5.1)	(1.7×10^{-3})	(0.004)	(1.0)	(640)	(66)
M19	0.4	1.6×10^{-3}	0.57	1.1×10^{-3}	0.012	3.0	2450	160
		(1.4×10^{-3})	(0.52)	(9.7×10^{-4})	(0.011)	(1.3)	(1900)	(120)
	1.3	6.5×10^{-3}	10.7	1.0×10^{-3}	0.30	3.9	1800	3.0
		(5.7×10^{-3})	(9.9)	(9.2×10^{-4})	(0.28)	(2.6)	(1500)	(2.6)
	4.0	4.1×10^{-3}	19.9	4.6×10^{-4}	0.51	3.9	4.4	1.6
		(4.1×10^{-3})	(20.2)	(5.0×10^{-4})	(0.51)	(3.9)	(5.6)	(1.6)
M13	0.4	2.3×10^{-3}	0.75	1.4×10^{-3}	0.04	3.1	1350	55
		(1.6×10^{-3})	(0.59)	(1.2×10^{-3})	(0.01)	(0.9)	(1900)	(40)
	1.3	5.4×10^{-3}	10.6	8.4×10^{-4}	0.46	3.4	250	2.6
		(5.0×10^{-3})	(10.2)	(7.6×10^{-4})	(0.33)	(2.3)	(450)	(2.3)
	4.0	3.5×10^{-3}	22.4	3.7×10^{-4}	0.54	4.5	5.0	1.4
		(3.5×10^{-3})	(22.6)	(3.3×10^{-4})	(0.54)	(4.5)	(5.4)	(1.4)
M3A	0.6	1.8×10^{-3}	0.39	1.4×10^{-3}	0.04	3.0	1100	1000
		(1.6×10^{-3})	(0.46)	(1.2×10^{-3})	(0.02)	(1.2)	(1400)	(470)
	1.3	2.6×10^{-3}	3.8	6.8×10^{-4}	0.78	3.8	61	4.5
		(2.6×10^{-3})	(3.9)	(6.7×10^{-4})	(0.76)	(3.6)	(74)	(4.3)
	4.0	2.2×10^{-3}	15.1	2.9×10^{-4}	0.43	4.0	2.6	1.5
		(2.2×10^{-3})	(15.2)	(2.8×10^{-4})	(0.43)	(4.0)	(2.7)	(1.5)
M3B	0.6	2.9×10^{-3}	0.70	1.7×10^{-3}	0.024	3.1	4000	320
		(2.0×10^{-3})	(0.59)	(1.3×10^{-3})	(0.004)	(1.0)	(2300)	(170)
	1.3	2.7×10^{-3}	7.3	5.1×10^{-4}	0.60	3.6	12.4	4.4
		(2.7×10^{-3})	(7.4)	(5.1×10^{-4})	(0.59)	(3.6)	(15.6)	(4.4)
	4.0	1.9×10^{-3}	13.3	2.7×10^{-4}	0.51	4.2	3.5	2.0
		(1.9×10^{-3})	(13.4)	(2.7×10^{-4})	(0.51)	(4.2)	(3.6)	(2.0)

Table A.4: Summary of correction methods for measured and calculated pulsatile grid turbulence properties.

Property
$\langle u_1^2 \rangle = \langle u_{1m}^2 \rangle - \langle u_{1bm}^2 \rangle$
$\langle u_2^2 \rangle = \langle u_{2m}^2 \rangle - \langle u_{2bm}^2 \rangle$
$\langle (\partial u_1/\partial t)^2 \rangle = \langle (\partial u_1/\partial t)_m^2 \rangle - \langle (\partial u_1/\partial t)_{bm}^2 \rangle$
$\langle (\partial u_1/\partial x_1)^3 \langle = \langle (\partial u_1/\partial x_1)_m^3 \rangle$
$R_m(t,\tau) = \frac{\langle u_{1m}(t) u_{1m}(t+\tau) \rangle}{\langle u_{1m}^2(t) \rangle}$
$R(t,\tau) = \frac{\langle u_{1m}(t) u_{1m}(t+\tau) - u_{1bm}(t) u_{1bm}(t+\tau) \rangle}{\langle u_{1m}^2(t) - u_{1bm}^2(t) \rangle}$
$L_{1m} = \langle U_1 \rangle \int_t^{t+\tau_0} R_m(t,\tau) d\tau$
$L_1 = \langle U_1 \rangle \int_t^{t+\tau_0} R(t,\tau) d\tau$
$\lambda_m = \langle U_1 \rangle \left[\langle u_{1m}^2 \rangle / \langle (\partial u_1/\partial t)_m^2 \rangle \right]^{1/2}$
$\lambda = \langle U_1 \rangle \left[\langle u_1^2 \rangle / \langle (\partial u_1/\partial t)^2 \rangle \right]^{1/2}$
$\mathrm{Re}_{\lambda m} = \langle u_{1m}^2 \rangle^{1/2} \lambda_m / \nu$
$\mathrm{Re}_{\lambda} = \langle u_1^2 \rangle^{1/2} \lambda / \nu$
$\varepsilon_m = 15 \nu \langle u_{1m}^2 \rangle / \lambda_m^2$
$\varepsilon = 15 \nu \langle u_1^2 \rangle / \lambda^2$
$\eta_m = \left(\nu^3 / \varepsilon_m \right)^{1/4}$
$\eta = \left(\nu^3 / \varepsilon \right)^{1/4}$
$S_m = \frac{\langle (\partial u_1/\partial x_1)_m^3 \rangle}{\left[\langle (\partial u_1/\partial x_1)_m^2 \rangle \right]^{3/2}}$
$S = \frac{\langle (\partial u_1/\partial x_1)^3 \rangle}{\left[\langle (\partial u_1/\partial x_1)^2 \rangle \right]^{3/2}}$
$C_{\varepsilon m} = (L_1 \varepsilon_m) / \langle u_{1m}^2 \rangle^{3/2}$
$C_{\varepsilon} = (L_1 \varepsilon) / \langle u_1^2 \rangle^{3/2}$

Table A.5: Summary of noise contamination and measured values for different variables for different flow conditions in pulsatile grid turbulence at $x_1/M = 20$.

Grid	$\langle U_1 \rangle$ [m/s]	$\langle u_1^2 \rangle$ [m^2/s^2] ($\langle u_{1m}^2 \rangle$ [m^2/s^2])	$\langle u_2^2 \rangle$ [m^2/s^2] ($\langle u_{2m}^2 \rangle$ [m^2/s^2])	$\langle (\partial u_1/\partial t)^2 \rangle$ [m^2/s^4] ($\langle (\partial u_1/\partial t)_m^2 \rangle$ [m^2/s^4])
–	0	3.6×10^{-7}	3.4×10^{-7}	0.8
–	2.3	2.4×10^{-4}	6.3×10^{-6}	14.4
		(2.4×10^{-4})	(6.7×10^{-6})	(15.2)
	2.9	6.6×10^{-4}	9.5×10^{-6}	18.5
		(6.6×10^{-4})	(9.9×10^{-6})	(19.3)
	3.5	2.4×10^{-4}	1.6×10^{-5}	22.2
		(2.4×10^{-4})	(1.6×10^{-5})	(23.1)
M19	2.3	4.8×10^{-3}	2.7×10^{-3}	1629
		(5.7×10^{-3})	(2.7×10^{-3})	(1645)
	2.9	8.8×10^{-3}	4.9×10^{-3}	7006
		(9.5×10^{-3})	(4.9×10^{-3})	(7025)
	3.5	1.5×10^{-2}	7.7×10^{-3}	15230
		(1.5×10^{-2})	(7.8×10^{-3})	(15260)
M51	2.3	0.7×10^{-2}	0.6×10^{-2}	886
		(0.8×10^{-2})	(0.6×10^{-2})	(903)
	2.9	1.3×10^{-2}	1.1×10^{-2}	3273
		(1.3×10^{-2})	(1.1×10^{-2})	(3292)
	3.5	2.1×10^{-2}	1.8×10^{-2}	6986
		(2.1×10^{-2})	(1.8×10^{-2})	(7008)

Table A.6: Summary of measured and corrected values for different turbulence variables for different flow conditions in pulsatile turbulence.

Grid	$\langle U_1 \rangle$ [m/s]	λ [m] (λ_m [m])	Re_λ ($\mathrm{Re}_{\lambda,m}$)	η [m] (η_m [m])	S (S_m)	C_ε $C_{\varepsilon,m}$
–	0	–	–	–	0.0054	–
–	2.3	1.8×10^{-2}	36.4	1.5×10^{-3}	0.02	26
		(1.8×10^{-2})	(36.4)	(1.5×10^{-3})	(0.02)	(26)
	2.9	1.4×10^{-2}	19.2	1.6×10^{-3}	0.01	31
		(1.4×10^{-2})	(19.2)	(1.6×10^{-3})	(0.01)	(31)
	3.5	1.4×10^{-2}	15.6	1.7×10^{-3}	0.007	64
		(1.4×10^{-2})	(15.6)	(1.7×10^{-3})	(0.007)	(64)
M19	2.3	4.2×10^{-3}	19.5	4.6×10^{-4}	0.51	1.3
		(4.5×10^{-3})	(22.8)	(4.6×10^{-4})	(0.51)	(23.1)
	2.9	3.7×10^{-3}	22.4	4.0×10^{-4}	0.48	1.6
		(3.8×10^{-3})	(22.5)	(4.0×10^{-4})	(0.48)	(6.3)
	3.5	3.3×10^{-3}	25.5	3.4×10^{-4}	0.4	1.6
		(3.3×10^{-3})	(25.6)	(3.4×10^{-4})	(0.4)	(1.6)
M51	2.3	6.8×10^{-3}	42.7	5.3×10^{-4}	0.53	1.1
		(7.1×10^{-3})	(46.6)	(5.3×10^{-4})	(0.55)	(5.8)
	2.9	6.6×10^{-3}	45.1	5.0×10^{-4}	0.43	1.1
		(6.7×10^{-3})	(46.5)	(5.0×10^{-4})	(0.44)	(1.8)
	3.5	5.8×10^{-3}	53.1	4.1×10^{-4}	0.42	1.0
		(5.8×10^{-3})	(53.8)	(4.1×10^{-4})	(0.42)	(1.1)

Appendix B

Specifications of non-stationary wind tunnel parts

This part of the appendix contains documentation for some of the components of the non-stationary wind tunnel components.

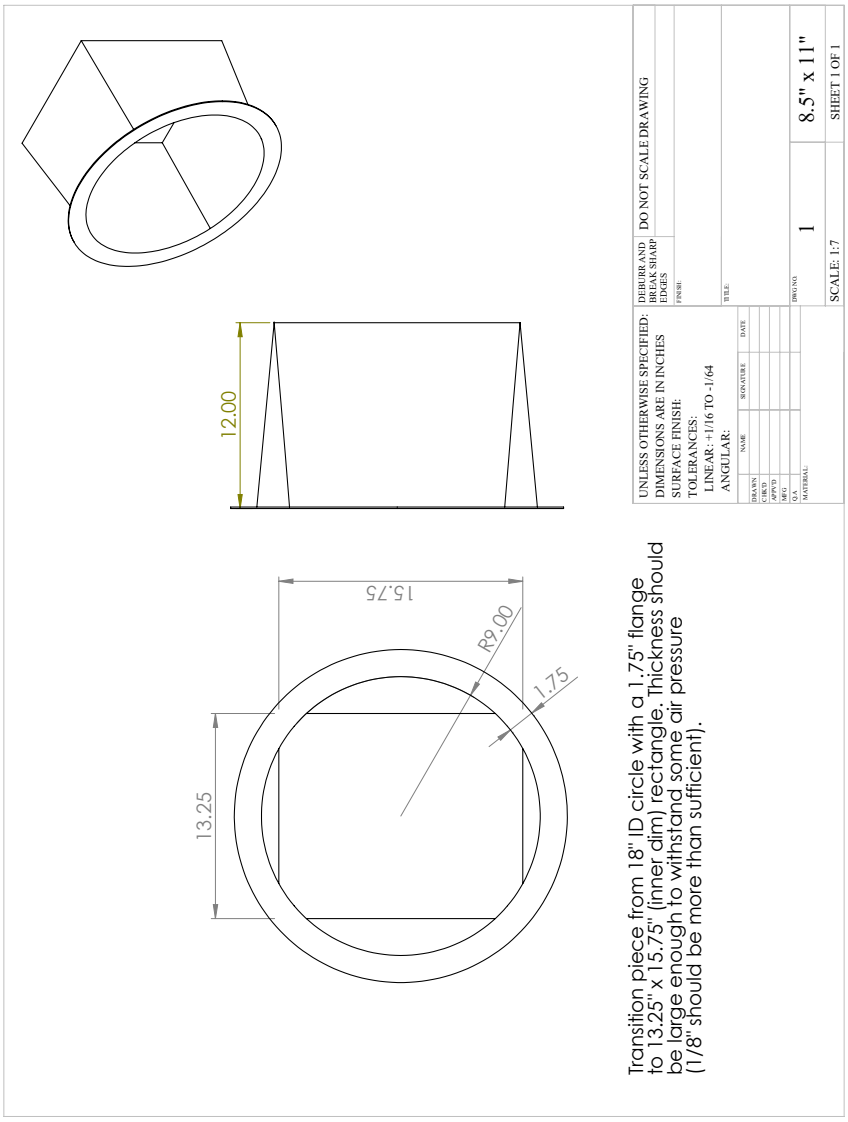

Figure B.1: Specifications of the circular-to-rectangular transition piece.

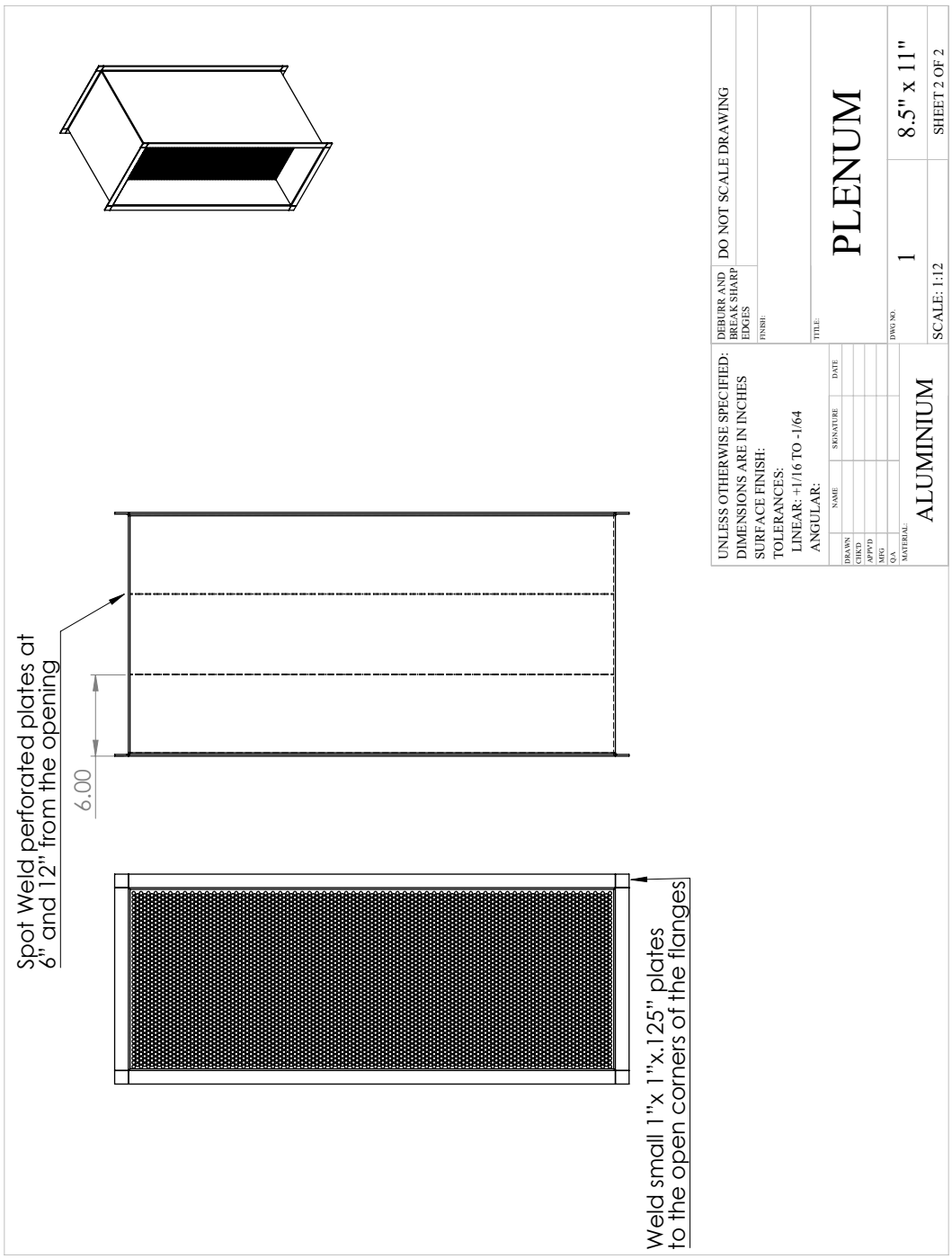

Figure B.2: Specifications of the channel with perforated plates for flow conditioning.

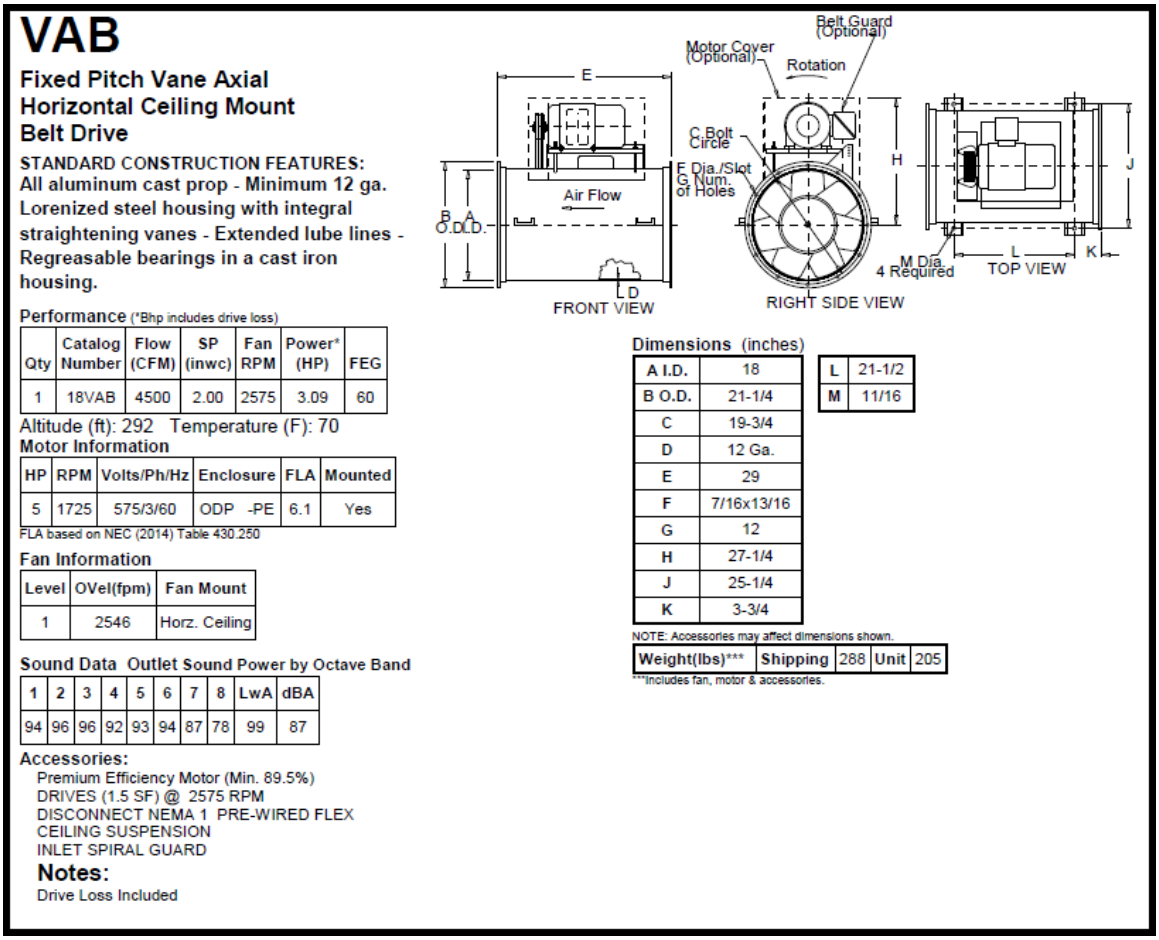

VAB

Fixed Pitch Vane Axial
Horizontal Ceiling Mount
Belt Drive

STANDARD CONSTRUCTION FEATURES:
All aluminum cast prop - Minimum 12 ga. Lorenized steel housing with integral straightening vanes - Extended lube lines - Regreasable bearings in a cast iron housing.

Performance (*Bhp includes drive loss)

Qty	Catalog Number	Flow (CFM)	SP (inwc)	Fan RPM	Power* (HP)	FEG
1	18VAB	4500	2.00	2575	3.09	60

Altitude (ft): 292 Temperature (F): 70

Motor Information

HP	RPM	Volts/Ph/Hz	Enclosure	FLA	Mounted
5	1725	575/3/60	ODP -PE	6.1	Yes

FLA based on NEC (2014) Table 430.250

Fan Information

Level	OVel(fpm)	Fan Mount
1	2546	Horz. Ceiling

Sound Data Outlet Sound Power by Octave Band

1	2	3	4	5	6	7	8	LwA	dBA
94	96	96	92	93	94	87	78	99	87

Accessories:
Premium Efficiency Motor (Min. 89.5%)
DRIVES (1.5 SF) @ 2575 RPM
DISCONNECT NEMA 1 PRE-WIRED FLEX
CEILING SUSPENSION
INLET SPIRAL GUARD

Notes:
Drive Loss Included

Dimensions (inches)

A I.D.	18
B O.D.	21-1/4
C	19-3/4
D	12 Ga.
E	29
F	7/16x13/16
G	12
H	27-1/4
J	25-1/4
K	3-3/4

L	21-1/2
M	11/16

NOTE: Accessories may affect dimensions shown.

Weight(lbs)***	Shipping	288	Unit	205

***Includes fan, motor & accessories.

Figure B.3: Specifications of the Loren Cook VAB18 axial fan.